MEASUREMENT OF FORWARD-BACKWARD ASYMMETRY AND SEARCH FOR NEW PHYSICS IN THE DIELECTRON CHANNEL WITH THE ATLAS DETECTOR

A Dissertation Presented to the Graduate Faculty of the

Dedman College

Southern Methodist University

in

Partial Fulfillment of the Requirements

for the degree of

Doctor of Philosophy

with a

Major in Experimental Particle Physics

by

Rozmin Daya K

(B.A., Southern Methodist University, 2006)

December 17, 2011

ACKNOWLEDGMENTS

First and foremost I thank Renat Ishmukhametov–my valued colleague, best friend and now husband. I've always been able to turn to you if with any question about physics analysis, statistics, or programming, and life in general. Even if you don't have the answer, you're always willing to patiently discuss things through with me. Without your support and help, being a physicist would be a lot more difficult and a whole lot less fun.

I am also grateful to my advisor (more so than he probably thinks), Ryszard Stroynowski, for his patience, insight, and especially for his passion for physics. The latter attribute has often manifested itself in the form of lively conversations (and mostly good-natured arguments), which have been an unforgettable part of my experience as a graduate student. I'm glad to have had an advisor who is so extraordinarily supportive and who is interested in my work. Even though I'm graduating and leaving SMU, I can honestly say that I look forward to working with Ryszard again in the future.

Thanks also to SMU ATLAS professors Stephen Sekula, Jingbo Ye and Bob Kehoe, who acted as mentors for me while writing my thesis and conducting the final pieces of analysis. They often made time in their very busy schedules to offer advice stemming from their rich and extensive experiences in this field. They have been there to talk about everything from actual analysis, defending and writing a thesis, politics of the field and job searches.

SMU theory professors Roberto Vega, Randall Scalise and Kent Hornbostel did their best to teach me physics. While I'm never going to be a theorist, I think that they were to some extent successful in their mission. Without their instruction I could not have written this thesis, and I probably wouldn't be able to do my job.

I want to acknowledge my fellow current and former ATLAS authors, without whom this work would not be possible. The ATLAS experiment is a huge collaboration, and the fact is that none of us do anything alone. Among this group of exceptional individuals, I want especially to thank: Mohamed Aharrouche, Marco Delmastro, Kamile Dindar-Yagci, Andrea di Simone, Marcello Fanti, Martin Goebel, Haleh Hadavand, Daniel Hayden, Sarah Heim, Yuriy Ilchenko, David Joffe, Marumi Kado, Azeddine Kasmi, Sebastian Koenig, Thomas Koffas, Dominick Olivito, Aidan Randle-Conde, Ryan Rios, Kristof Schmeiden, Kerstin Tackmann, Haichen Wang and Martin Woudstra for their assistance, support and friendship.

I want also to acknowledge the Lightner-Sams foundation, for their support of a more material, but certainly no less essential, nature. Two grants from the foundation enabled me to conduct my graduate studies while based at CERN, the very epicenter of Particle Physics. The value of this can not be overstated.

I also am grateful to my parents; firstly, for putting up with me, and secondly, for everything else.

Daya K, Rozmin B.A., Southern Methodist University, 2006

Measurement of forward-backward asymmetry and search for new physics in the dielectron channel with the ATLAS detector

Advisor: Professor Ryszard Stroynowski

Doctor of Philosophy degree conferred December 17, 2011
Dissertation completed September 28, 2011

High p_T, isolated electrons are key components of some of the most interesting signatures that may be observed in collision data from the Large Hadron Collider (LHC). One such example is the decay of a high mass, neutral particle with narrow natural width to an e^+e^- pair. This thesis outlines the author's contributions to the direct, model independent search for such a particle as a bump in the dielectron invariant mass spectrum using 167 pb^{-1} of data collected by the ATLAS detector in 2011. Limits on such a resonance in the context of an extra heavy gauge boson (Z') have been set. Additionally, the electron forward-backward charge asymmetry, which is also sensitive to the presence of a Z' particle, is measured as a function of invariant mass with 1.073 fb^{-1} proton-proton collision data recorded by the ATLAS experiment. The observed distribution is compared to the Standard Model expectation using simulated data in order to search for evidence of a Z'. In both cases, no evidence for a Z' is observed. Different amounts of data for the two analyses correspond to the fact that the indirect search was performed several months after the direct one.

TABLE OF CONTENTS

LIST OF FIGURES

LIST OF TABLES

This dissertation is dedicated to my family

Chapter 1

THE HIGH ENERGY FRONTIER

Always listen to experts. They'll tell you what can't be done and why. Then do it.
The definition of impossible changes over time.

Robert A. Heinlein (1907-1988)
American science fiction writer and engineer

1.1. A new kind of adventure

The frontiers that mankind sets out to tame have themselves evolved over time, growing grander and more complex, more difficult to attain. A primate ancestor, millions of years ago, decides to come down from the trees and see what the ground below has to offer[1]. A small band of sailors, thousands of years ago, ventures out across a forbidding ocean that no one has before crossed, and which is thought to end only by falling off the Earth's edge. Three men, decades ago, allow themselves to be hurtled through and beyond the atmosphere in what is essentially a cramped metal box, out into empty space, to set foot on the moon's virgin surface.

It is not necessary, however, for exploration to involve risk of severe bodily harm. Today's physicists set out to map a new land of a different nature, aiming to probe distances on an impossibly small scale by using collisions of energy higher than we have ever produced before. It would not be an exaggeration to say that this is now an entirely new age; it is the age of truly high energy physics.

[1] Lions, as it turns out.

1.2. The Standard Model

In order to frame the questions of this exciting era, it is necessary to understand the current state of affairs, to have a description of our best model of what the universe is made of and how it works. This model is known as the Standard Model of physics.

In the Standard Model, almost all matter can be sub-divided further into the most fundamental building blocks: particles known as quarks and leptons. There are six of each of these types of particles, shown in Figure 1.1.

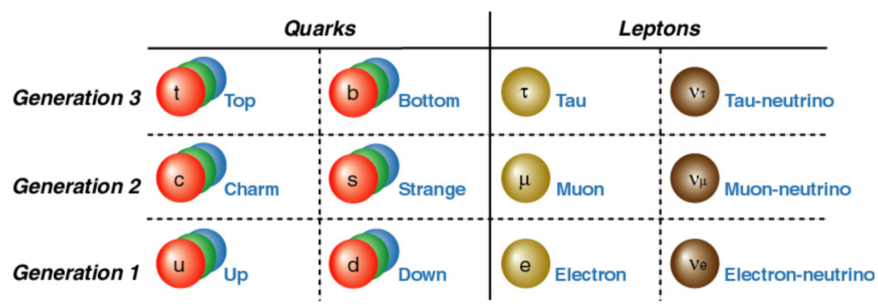

Figure 1.1. The 'generations' of quarks and leptons. The first generation of quarks and non-neutrino leptonsis the lightest and the third the heaviest. The neutrinos are nearly massless with undetermined mass. [48]

Additionally, there exist indivisible, and in some cases massive, particles that mediate three of the known four forces: the photon, which mediates the electromagnetic force, the gluon, which mediates the strong force that holds matter together, and the W and Z bosons, which mediate the weak force that governs β decay. These are the gauge bosons. Particles that can be produced or decay via a given force must 'couple' to the force's carrier with a certain strength. The strength, or value, of this coupling is particle dependent.

The final indivisible component of the Standard Model is the proposed Higgs boson. The Higgs boson is thought to interact with all other particles in such a way that they become massive. Because of this, all massive particles–including the Higgs itelf–must couple to the Higgs. The only Standard Model particles to which the Higgs does not couple are gluons and photons, as shown in Figure 1.2.

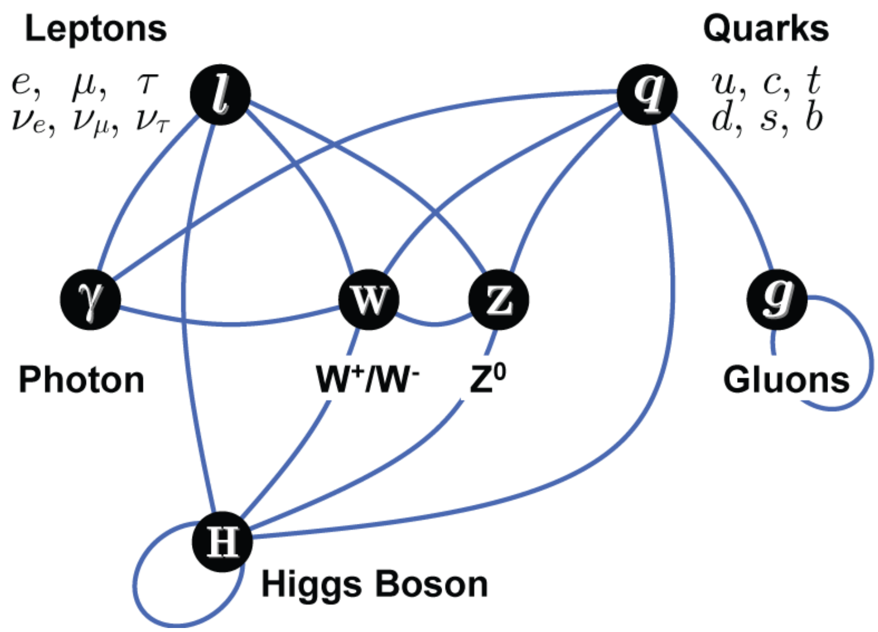

Figure 1.2. The particles of the Standard Model. The blue lines indicate couplings between particles (strength of the coupling is not indicated by the illustration). [95]

The discovery of the Higgs boson and the precise measurement of its fundamental characteristics is a major goal of physicists today. Despite extensive searches conducted at lower energy, the Higgs boson remains undiscovered. This is one of the motivating factors for pushing the borders of the energy frontier farther and farther.

1.3. Beyond Standard Model physics

One reason for exploring physics at very high energy is to answer questions on which the Standard Model is silent. This includes problems such as:

- **What is dark matter?** The speed of rotation of galaxies has been measured precisely and found to differ from the value it must be given the amount of mass observed [92]. To explain this, an additional source of matter is introduced. This is called dark matter, as it is not observed directly. Again, since it is not observable directly, dark matter is thought to interact only via the weak force. The only particle that behaves this way in the Standard Model is the neutrino. However, recent limits on the neutrino mass [77] suggest that the mass of all neutrinos in the universe is not enough to explain the existence of dark matter. Ideally, a theory of Beyond Standard Model physics should contain a potential dark matter candidate.

- **Arbitrary number of generations?** As was described previously, the Standard Model contains three generations of quarks and leptons. This does not derive from the theoretical model, but is rather an experimental observation, and is thus arbitrary. A more compelling model would be one that predicts the number of particles observed.

- **Explanation of gravity?** It is a well-known problem of modern physics that Einstein's theory of General Relativity does not reconcile with quantum mechanics. Any Beyond Standard Model theory that encompasses the observed Standard Model must also contain a viable explanation for gravity at the quantum level.

- **Why don't forces unify?** At the beginning of the universe, before the Big Bang, it seems reasonable to hypothesize that all the observed forces were consolidated into one. As we probe ever higher energies and ever smaller distance scales, we come closer and closer to replicating those pre-Big Bang conditions.

Therefore, at these higher energy scales the forces should again unify. The measure of this unification is usually accomplished by plotting the coupling constants of the weak, electromagnetic and strong forces as a function of energy, shown for the Standard Model case in Figure 1.3. As can be seen, the coupling constants do not meet at a point in the Standard Model.

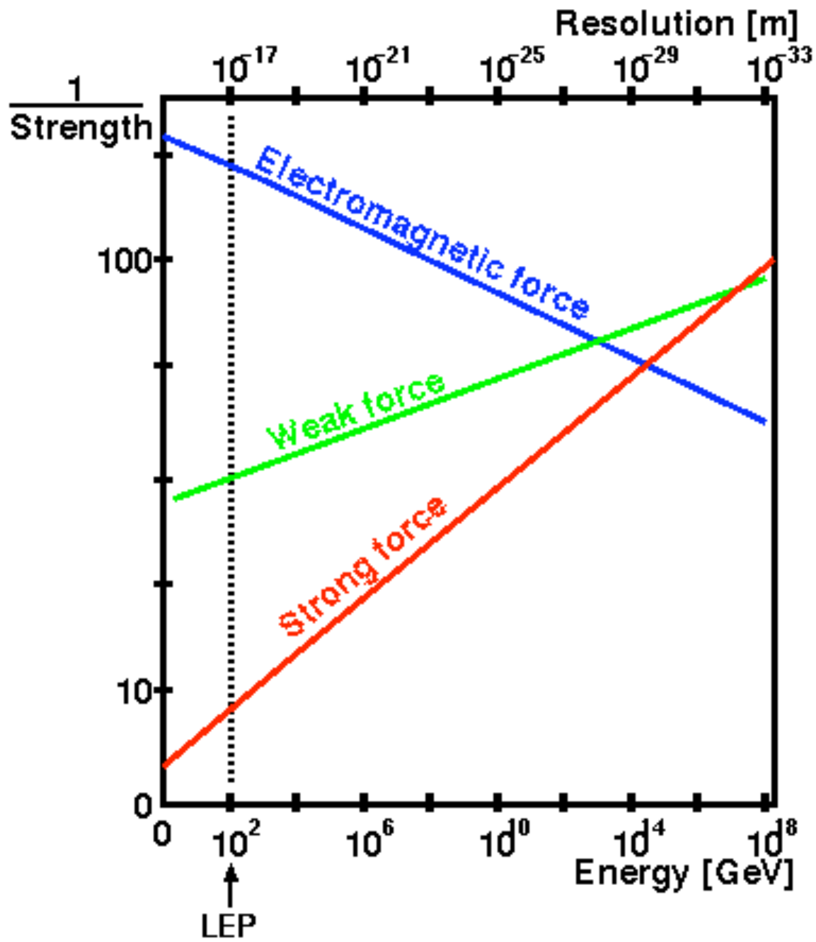

Figure 1.3. The weak, electromagnetic and strong force coupling 'constants' of the Standard Model, as a function of energy. The values measured from the CERN LEP experiments are indicated by the dashed line [34].

A set of Beyond Standard Model theories that aims to address the issue of force unification is known as Grand Unification Theories (GUTs). In GUTs, the forces of Figure 1.3 would be unified at high mass; unification means equal strength of reactions and equal couplings for all forces. Some of these theories also provide answers to the other questions mentioned.

1.4. Grand Unification models with extra neutral gauge bosons (Z')

The topic of this thesis involves searches for one or more additional neutral gauge bosons. Such particles are predicted in a class of GUT theories known as E_6 models, with E_6 being the gauge group whose spontaneous symmetry breaking allows directly for the existence of these bosons.

1.4.1. GUT models based on the E_6 gauge group

The Standard Model can be described by the group representation $SU(3)_c \times SU(2)_L \times U(1)_\gamma$. Here $SU(3)_c$ describes the strong interactions; $SU(2)_L$ describes the weak interactions (with the subscript denoting the fact that the weak force only couples to left-handed fermions); and $U(1)_\gamma$ describes the electromagnetic interactions mediated by the photon and the Z boson.

Like other GUT models, models based on the E_6 gauge group attempt to describe all observed interactions within a single group. The minimal group for which this is possible is $SU(5)$, however, models based on $SU(5)$ have finite proton lifetime. Models based on the E_6 group are interesting as they are consistent with physical observations and are fairly minimal in the number of new particles introduced. When considering string theory, E_6 is after $SO(10)$ the next most minimal single representation possible, and, unlike with $SO(10)$, the number of generations is specified by the theory and is not arbitrary. Another attractive aspect of E_6 as the grand unification group is that the gauge symmetry breaking can occur at intermediate energy scales. Since string theory hypothesizes the existence of a particle known as the Graviton, which would mediate the gravitational force, E_6 based GUT models are able to solve the gravity problem described previously. In addition to this, the E_6 group contains all Standard Model fermions, two Higgs doublets and a right-handed neutrino, which provides a possible dark matter candidate [46] [53][38].

Additional gauge bosons are a natural consequence of the E_6 symmetry breaking to groups of rank 5 or 6:

$$\begin{aligned} E_6 \rightarrow & \\ & SU(3)_c \times SU(2)_L \times U(1)_\gamma \times U(1)_\eta \\ & \\ & SU(3)_c \times SU(2)_L \times U(1)_\gamma \times U(1)' \times U(1)'', \\ & SU(3)_c \times SU(2)_L \times SU(2)' \times U(1)' \times U(1)'', \end{aligned} \tag{1.1}$$

where the first group representation is of rank 5 and the last two are of rank 6. Groups denoted by with the prime symbol in the two separate rank 6 scenarios are independent. Using the decomposition

$$\begin{aligned} E_6 &\rightarrow SO(10) \times U(1)_\psi \\ &\rightarrow SU(5) \times U(1)_\chi, \end{aligned} \tag{1.2}$$

the terms $U(1)' \times U(1)''$ can be written as $U(1)_\psi \times U(1)_\chi$. These groups form an orthogonal basis, and thus the mixing of their associated states (Z_χ and Z_ψ) yields the massive gauge bosons, $Z'(\theta)$ and $Z''(\theta)$ generated in the breaking of E_6 to the rank 6 group representations:

$$Z'(\theta) \equiv Z_\psi \cos\theta - Z_\chi \sin\theta,$$
$$Z''(\theta) \equiv Z_\chi \cos\theta + Z_\psi \sin\theta, \quad (1.3)$$

where θ is the (unspecified) mixing angle between the two states.

While the E_6 breaking to a rank 6 group representation leads to two additional neutral gauge bosons light enough to couple to the Standard Model Z boson, in the rank 5 scenario the Z" is so heavy (on the order of, or greater than 10 TeV mass) that it does not couple to the Z or the Z'. This scenario, which effectively considers only one additional Z', is the most commonly considered for the sake of simplicity. Note that the mixing angle θ is not specified in this set of models; limits on the mass of $Z'(\theta)$ for various θ values are discussed in the following section.

1.5. Current limits on the minimal mass of a leptonically decaying Z'

The best limits on the mass of a Z' boson that decays to leptons have been set by the LHC experiments ATLAS [43] and CMS [65]. For a Z' in the E_6 model, ATLAS has set limits for several values of the mixing angle, θ: $\theta = 0°$ ($Z' \equiv Z_\chi$), $\theta = 90°$ ($Z' \equiv Z_\psi$), $\theta = -52.5°$ ($Z' \equiv Z_\eta$), $\theta = 37.8°$ ($Z' \equiv -Z_I$), $\theta = 23.3°$ ($Z' \equiv Z_S$) and $\theta = 75.5°$ ($Z' \equiv Z_N$). CMS has set limits on the mass of the Z_ψ. The limits are summarized in Table 1.1 and use a combination of information from the electron and muon channels.

Table 1.1. Best limits on the mass of the Z' decaying leptonically, in the context of the E6 model. Limits are shown for several values of the mixing angle θ.

	Z_ψ	Z_χ	Z_η	Z_I	Z_S	Z_N
ATLAS [21]	1.49 TeV	1.64 TeV	1.54 TeV	1.56 TeV	1.60 TeV	1.52 TeV
CMS [36]	1.62 TeV	-	-	-	-	-

Limits have also been set by both experiments on a Z' having couplings to quarks and leptons of the Standard Model equal to that of the Z boson. This is known as the Z' of the Sequential Standard Model (SSM) [62][93]. Such a Z' can only exist if its couplings to non-Standard Model fermions differ from those of the Z boson. The SSM Z' is not considered as physically well-motivated as those of the E6 models, yet limits are usually set on it's mass to serve as a benchmark between experiments. Using a combination of information from electron and muon channels, ATLAS has set a limit [21] on the mass of the SSM Z' of 1.83 TeV, while CMS has set a limit [36] of 1.94 TeV.

Limits on the Z' boson from ATLAS are shown in Figure 1.4 and the limits from CMS are shown in Figure 1.5. As both experiments have conducted general, model independent searches for dilepton resonances, limits on the existence of other particles decaying to a same flavor dilepton final state are also depicted in the CMS plot.

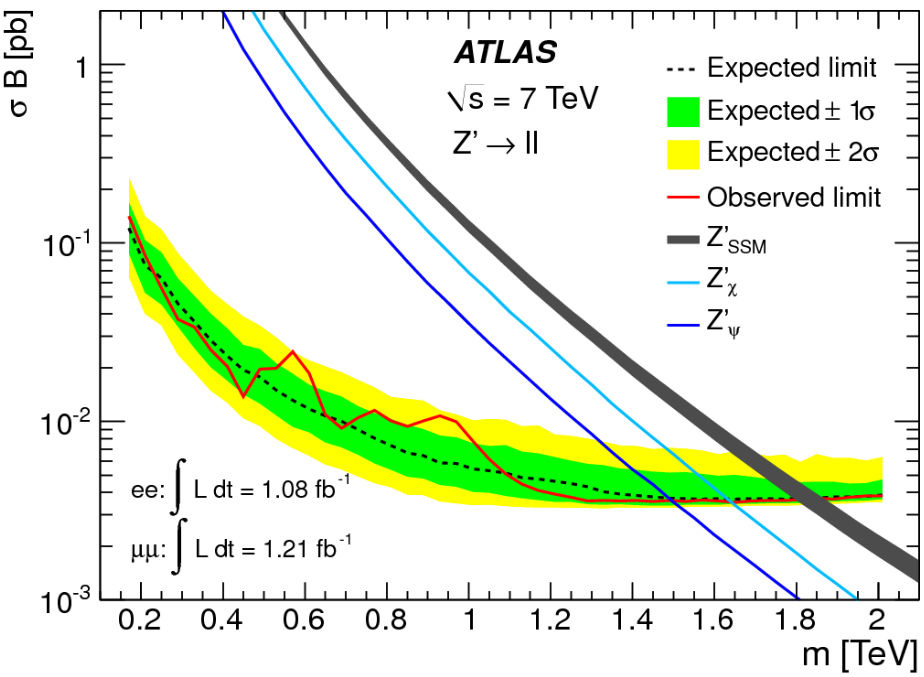

Figure 1.4. Limits set on the mass of a leptonically decaying Z'. Only results for the SSM Z' (gray band), Z_ψ (blue line) and Z_χ (cyan line) are shown. In the case of the SSM, the thickness of the gray band indicates the theoretical uncertainty. For all models, the point where each line intersects with the observed limit on cross section times branching ratio (red line) corresponds to the limit on the Z' invariant mass.

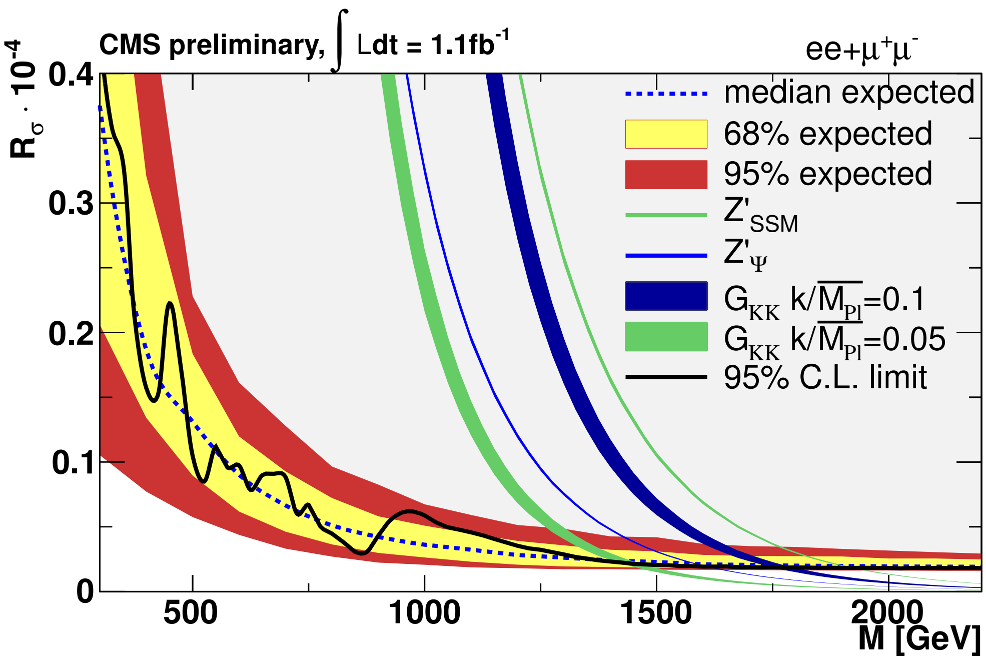

Figure 1.5. Limits set on the mass of a leptonically decaying Z', along with other non-Standard Model particles decaying to same flavor dileptons. The limit on the Z_ψ is shown by the thin blue line, and the SSM Z' by the thin green line. The point where these lines intersect with the observed 95% confidence level observed limit on the dilepton cross section (thin black line) corresponds to the limit on the Z' invariant mass. The thick green and blue bands correspond to limits on the hypothetical Graviton decaying to dielectrons or dimuons, in the Kaluza-Klein model [87][60].

During the 2011 LHC run, several limits on the Z' mass were released by ATLAS [24][23][22][21] and the rate of improvement has been rapid. This has not been due to any fundamental change in the analysis since the winter of 2010, when the first results of this search from both experiments were made public. Rather, the improvement has been due to the steady increase in integrated luminosity delivered by the LHC. The limits on the mass of the Z' shown in Chapter 4 of this thesis represent one point in the aforementioned series. While they are not the current best, the methodology used to obtain them is consistent with that used to obtain the results discussed in this section.

1.6. Alternative Z' search method: forward-backward asymmetry

In addition to direct searches conducted using the dielectron invariant mass spectrum, a Z' particle particle can be searched for using lepton forward-backward asymmetry. This asymmetry, characteristic of the Drell-Yan [83] process, is expected in the Standard Model.

1.6.1. The Drell-Yan process

The Drell-Yan process, $q\bar{q} \rightarrow Z/\gamma^* \rightarrow l^+l^-$, occurs when a Z boson or virtual photon is produced and subsequently decays to a pair of oppositely charged leptons. The process is depicted in Figure 1.6.

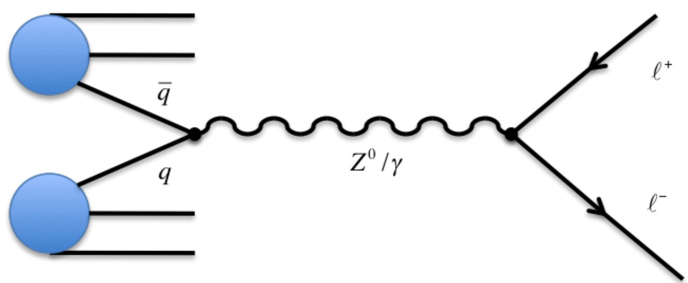

Figure 1.6. The annihilation of a quark anti-quark pair into a Z boson or virtual photon, subsequently decaying into two oppositely charged leptons.

1.6.2. Forward-backward asymmetry, A_{FB}, in the Standard Model

Angular asymmetry of the decay products in the Drell-Yan process is predicted by the Standard Model. Measured near the Z pole, the asymmetry can be used to obtain precision measurements of other electroweak Standard Model parameters, such as the electroweak mixing angle, θ_W. For masses far above that of the Z boson, the Standard Model predicts a constant asymmetry value of 0.6.

It can be seen that this asymmetry is naturally expected by simplifying the equation for the differential cross section of the process depicted in Figure 1.6 with respect to the angle θ^*, the angle between the incoming quark and outgoing lepton in the dilepton rest frame. This differential cross section is given by [64]:

$$\begin{aligned}\frac{d\sigma}{d\cos\theta^*} =& \frac{1}{3}\int_0^1 dx_a \int_0^1 dx_b \sum_q q(x_a,s)\overline{q}(x_b,s)\left(\frac{\pi\alpha^2}{2s}\right)\left\{Q_q^2 Q_l^2(1+\cos^2\theta^*)\right.\\ &+ 2Q_q Q_l \mathrm{Re}\chi(s)\left[g_V^l g_V^q(1+\cos^2\theta^*) + 2g_A^l g_A^q\cos\theta^*\right]\\ &+ |\chi(s)|^2\left[\left((g_V^l)^2+(g_A^l)^2\right)\left((g_V^q)^2+(g_A^q)^2\right)(1+\cos^2\theta^*)\right.\\ &+ \left.\left. 8g_V^l g_A^l g_V^q g_A^q\cos\theta^*\right]\right\},\end{aligned} \tag{1.4}$$

where $Q_{q(l)}$ is the charge of the quark (lepton), $\frac{1}{3}$ is the color factor, $q(x_a,s)$ and $\overline{q}(x_b,s)$ are the parton distribution functions (PDFs) for the quark and the antiquark and $g_A^{l(q)}$ $\left(g_V^{l(q)}\right)$ are the axial (vector) couplings of the leptons (quarks) of Figure 1.6.

Then, the differential cross section with respect to $\cos\theta^*$ can be simplified as:

$$
\begin{aligned}
\frac{d\sigma}{d\cos\theta^{*}} =& C\frac{4}{3}\frac{\pi\alpha^{2}}{s}R_{f}\left[\frac{3}{8}\left(1+\cos^{2}\theta^{*}\right)+A_{FB}\cos\theta^{*}\right] \\
R_{f} =& R^{VV}+R^{AA} \\
A_{FB} =& \frac{R^{VA}}{R_{f}} \\
R^{VV} =& Q_{l}^{2}Q_{q}^{2}+2Q_{l}Q_{q}g_{V}^{q}g_{V}^{l}Re\left(\chi\left(s\right)\right)+g_{V}^{l^{2}}\left(g_{V}^{q^{2}}+g_{A}^{q^{2}}\right)\left|\chi\left(s\right)\right|^{2} \\
R^{AA} =& g_{A}^{l^{2}}\left(g_{V}^{q^{2}}+g_{A}^{q^{2}}\right)\left|\chi\left(s\right)\right|^{2} \\
R^{VA} =& \frac{3}{2}g_{A}^{q^{2}}g_{A}^{l}\left(Q_{l}Q_{q}Re\left(\chi\left(s\right)\right)+2g_{V}^{q}g_{V}^{l}\left|\chi\left(s\right)\right|^{2}\right) \\
\chi\left(s\right) =& \frac{1}{\left(\cos^{2}\theta_{W}\sin^{2}\theta_{W}\right)}\frac{s}{\left(s-M_{Z}^{2}+i\Gamma_{Z}M_{Z}\right)},
\end{aligned}
\tag{1.5}
$$

where C is the color factor, M_Z is the mass of the Z and Γ_Z is the Z width. It can be seen from Equation 1.5 that the forward backward ratio, A_{FB}, is in a sense a ratio of mixing between the axial and vector couplings. Physically, this means that asymmetry in the decay of Figure 1.6 exists due to interference between the amplitudes of the Drell-Yan process as mediated by the two neutral electroweak guage bosons: the photon (which couples only electromagnetically via the vector components) and the Z boson (which couples both weakly via the axial components and electromagnetically via the vector components).

Integrating A_{FB} over $\cos\theta$, we find that

$$
A_{FB} = \frac{\int_{0}^{+1}\frac{d\sigma}{d\cos\theta}d\cos\theta+\int_{0}^{-1}\frac{d\sigma}{d\cos\theta}d\cos\theta}{\int_{-1}^{+1}\frac{d\sigma}{d\cos\theta}d\cos\theta} = \frac{N_{F}-N_{B}}{N_{F}+N_{B}}. \tag{1.6}
$$

Here N_F is the number of events for which the value of $\cos\theta$ is greater than zero and N_B is the number of events for which the value of $\cos\theta$ is less than zero.

1.6.3. Current measurements of A_{FB} vs dielectron invariant mass

Measurements of A_{FB} have focused on two goals: precision measurement near the Z pole, in order to obtain the value of $\sin^2\theta_W$, and measurement as a function of invariant mass, which is one topic of this thesis. The best[2] published measurements to date as a function of invariant mass have been made by the D0 collaboration, which has published a measurement of A_{FB} vs invariant mass for e^+e^- pairs between 50 and 1000 GeV using 5.0 fb^{-1} of data [39] (see Figure 1.7).

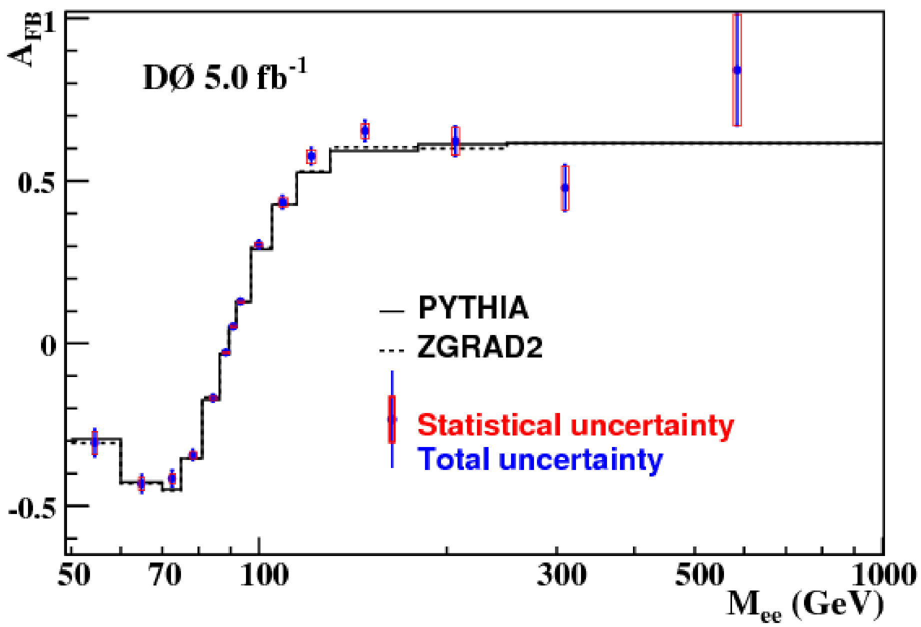

Figure 1.7. A_{FB} vs dielectron invariant mass, measured by the D0 collaboration. The blue dots represent the values measured on data, while the blue error bars are statistical only and the red error bars include systematic effects. The black line shows the Standard Model expectation as obtained from simulated data samples. Below the Z pole the value of A_{FB} dips below zero due to photon self-interference (higher order radiative corrections) [90].

[2]Here 'best' is taken to mean the measurement probing farthest in terms of dielectron invariant mass.

1.6.4. Lepton forward-backward asymmetry in the presence of a Z'

As was shown in Section 1.6.2, lepton forward-backward asymmetry exists due to the interference between the amplitudes of the two neutral bosons mediating the electromagnetic and weak forces, the photon and the Z. If a Z' boson exists, it will have both axial and vector couplings like the Z, and the resulting $\gamma/Z/Z'$ interference should be observable by measuring A_{FB} as a function of e^+e^- invariant mass [76]. As seen in the previous section, a measurement of A_{FB} up to 1 TeV has just recently been made. In making this measurement with 5.0 fb^{-1} $p\overline{p}$ collision data at $\sqrt{s}$ =1.96 TeV, the D0 collaboration identified 227 e^+e^- events in the high mass region from 250 to 1000 GeV. In the same mass window, ATLAS has identified approximately 500 events with only 1 fb^{-1} of data, see the analysis presented in Chapter 5 of this thesis. This is due to the much higher center of mass collision energy at the LHC as compared to the Tevatron. As direct searches have excluded a Z' in E_6 models lighter than 1.49-1.64 TeV, a measurement of A_{FB} at the energy frontier is an especially interesting endeavor.

1.7. Purpose of this thesis

This thesis outlines the author's contributions to a direct search for the Z' particle using the e^+e^- invariant mass spectrum and a measurement of A_{FB} using electrons. Both analyses are done using the ATLAS detector at the Large Hadron Collider, described in the next chapter. The analyses reflect collaborative work done by members of the ATLAS experiment. However, the entire analysis must be presented in order to place the author's work, which has been emphasized in this thesis, in context. In both cases, the author has made significant contribution to the analysis.

Chapter 2

THE LHC AND THE ATLAS DETECTOR

Physics as we know it will be over in six months.
In reaction to the Dirac equation

Max Born (1882-1970)
German physicist, Nobel laureate

2.1. The Large Hadron Collider

The Large Hadron Collider is a 27 kilometer in circumference particle accelerator located near Geneva, Switzerland. Two beams of protons traveling around this ring at 2.998 $\times 10^8$ m/s are made to collide at the sites of the LHC experiments: ATLAS, CMS, LHCb and ALICE. First data from proton-proton collisions were recorded September 10, 2008, but due to an incident occurring shortly thereafter, data taking stopped until March 30, 2010.

With the mere 40 pb^{-1} of data collected in 2010, knowledge of the Standard Model was enriched by several interesting results and papers from the LHC experiments, and limits were set on many new models of physics. In 2011, the experiments at the LHC continue to probe the high-energy frontier for new phenomena. As of the time of writing this thesis, well over 1 fb^{-1} data have been recorded by the ATLAS detector; the possibilities of what we may find in the next few years truly stretch the imagination.

2.1.1. The LHC accelerator complex

The Proton Synchrotron (PS) and Super Proton Synchrotron (SPS) [88] are important early steps in getting the proton beams accelerated through the LHC up to their energy of 3.5 TeV per beam. The protons, taken from the nuclei of hydrogen atoms, are injected from the linear accelerator (LINAC2) into the PS Booster. From here they enter the PS, shown in Figure 2.1, a schematic of the LHC accelerator complex. From the PS, the protons ender the SPS. Even after being accelerated in the PS and SPS, protons must travel around the LHC ring itself for 20 minutes before reaching their final energy.

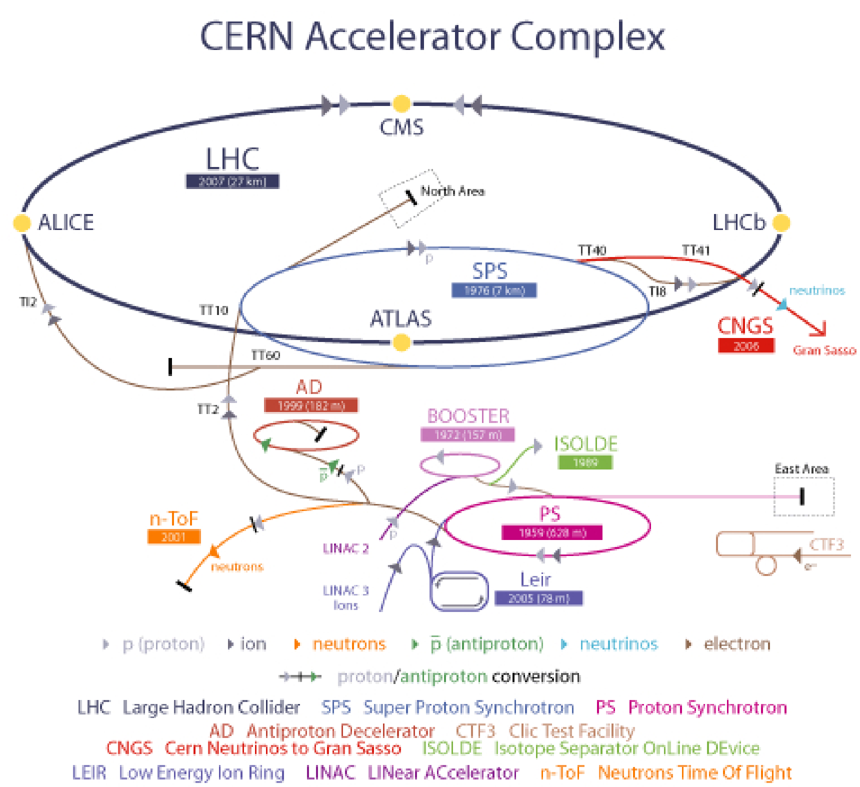

Figure 2.1. The many steps required to bring the protons of the LHC beams up to their full energy [88].

2.1.2. Guiding and containing the proton beams

Due to the fact that a charged particle bends in a magnetic field according to $F = q\vec{v} \times \vec{B}$, magnets are used to control the direction and spread of the proton beams. Two different types of magnets are employed for these purposes, dipoles and quadrupoles. Both types are super-conducting electromagnets, which must be operated at very low temperature. Consequently, the LHC is kept at -271 K.

Dipole magnets are used to steer the beams[1]. They produce a magnetic field that is homogeneous, and thus a charged particle (such a as a proton) travels in a circular trajectory in their presence. Quadrupole magnets are used to focus the beams, making it narrower, so that when they collide it is with greater intensity. Greater intensity is desirable as an increased density of protons in the beam cross section increases the probability that a collision will occur. The quadrupole magnets generate a magnetic field of variable strength, the magnitude increasing as the particle travels further (radially) from the magnet's longitudinal axis. Examples of dipole and quadrupole magnets are shown in Figure 2.2.

[1] And also to decorate the centers of round-abouts in St. Genis.

a)  b) 

Figure 2.2. Examples of a) dipole [35] and b) quadrupole magnets [33] used in the LHC.

2.1.3. Underlying event

As there are three quarks in every proton, the beam collision produces many particles. However, not all of these particles are produced with the same energy. The parton-parton interaction with the highest energy parton in each of the proton beams is referred to as the 'hard' process, or hard scattering. This is the process likely to produce an interesting event, such as the production of a Higgs or a Z boson. When the other partons in the proton fragment or collide with each other it is at lower energy. This is called the 'underlying event', and is corrected for when measuring the energy of particles from the hard process. A diagram of the hard process and underlying event in pp collisions is shown in Figure 2.3.

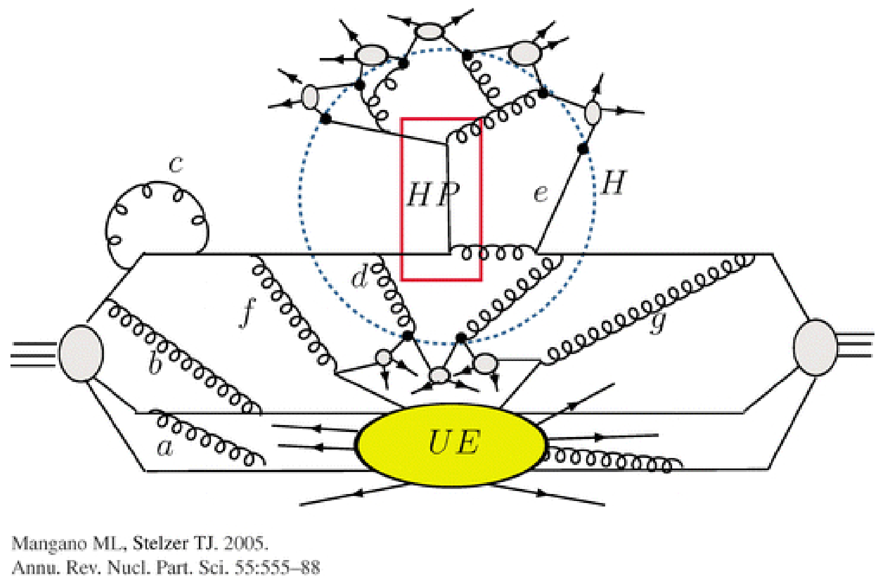

Figure 2.3. Colliding protons indicated by pink circles on the extreme left and right sides of the diagram. The underlying event is shown in yellow and labeled "UE" while the hard process is contained by the red square and labeled "HP." The end products of the hard process are contained by the blue circle (drawn with dashed line).

2.1.4. Pile-up

The proton beams circulating the LHC do not use one proton after another in a continuous stream. Instead, in order to separate collisions, protons are grouped together in bunches, with the bunches separated by a given time interval. If the rate of bunches per unit time is increased, the rate of collisions and of potentially interesting events also increases. In 2011, the LHC has operated in two configurations: in early 2011, the beams were circulated at 50 bunches per nanosecond and for the bulk of the data taking they were circulated at 75 bunches per nanosecond. There are plans to return to 50 bunches per nanosecond spacing for the remainder of 2011.

Even though increasing the number of bunches per unit time circulated increases the rate of collision events, it also introduces the problem of pile-up. This is the term used when a devastating car accident occurs on a busy highway; a car rear-ends the one in front of it, and is subsequently hit by the car behind, which is hit by the car behind it, and so on, until there is a multi-vehicle collision that is very messy to sort out afterwards. The same is true when the word pile-up is applied to collisions in particle physics, describing the situation of more than a single proton-proton collision occurring simultaneously. In such a case, not only is there information from the underlying event to account for, but there is more than one process, and thus many decay products. This can lead to inaccuracies in reconstructing particles from the remnants they decay to.

2.2. The ATLAS Detector

The ATLAS[2] detector, which stands for **A** **T**orroidal **L**HC **A**pparatu**S**, is the tool used in this thesis to attempt to discover new physics beyond the Standard Model. ATLAS consists of a series of nested subdetectors: the Inner Detector, whose layers of different tracking subsystems allow the reconstruction of charged particles' tracks; calorimeters, which measure the energy deposited by particles; and muon chambers on the outside. A combination of software and hardware known as the 'trigger' is used to select only those events that are interesting for analysis.

An illustration of the ATLAS detector with rectangular coordinate system superimposed is shown in Figure 2.4. The z axis is taken to be parallel to the beam direction and the x-y plane defines the transverse plane. A common means of in-

[2] ATLAS is also the name of the collaboration that built, maintains and uses the ATLAS detector to analyze data from proton-proton and heavy nuclei (lead) collisions at the LHC.

dicating position in ATLAS is by the (η, ϕ) coordinate. The pseudorapidity, η, is defined as

$$\eta = -\ln\left(tan\left(\frac{\theta}{2}\right)\right), \tag{2.1}$$

where the angle θ is that between the particle direction and the z axis. The angle ϕ is the angle between the projection of the particle's location onto the x-y plane and the x axis. This coordinate system is shown in Figure 2.5.

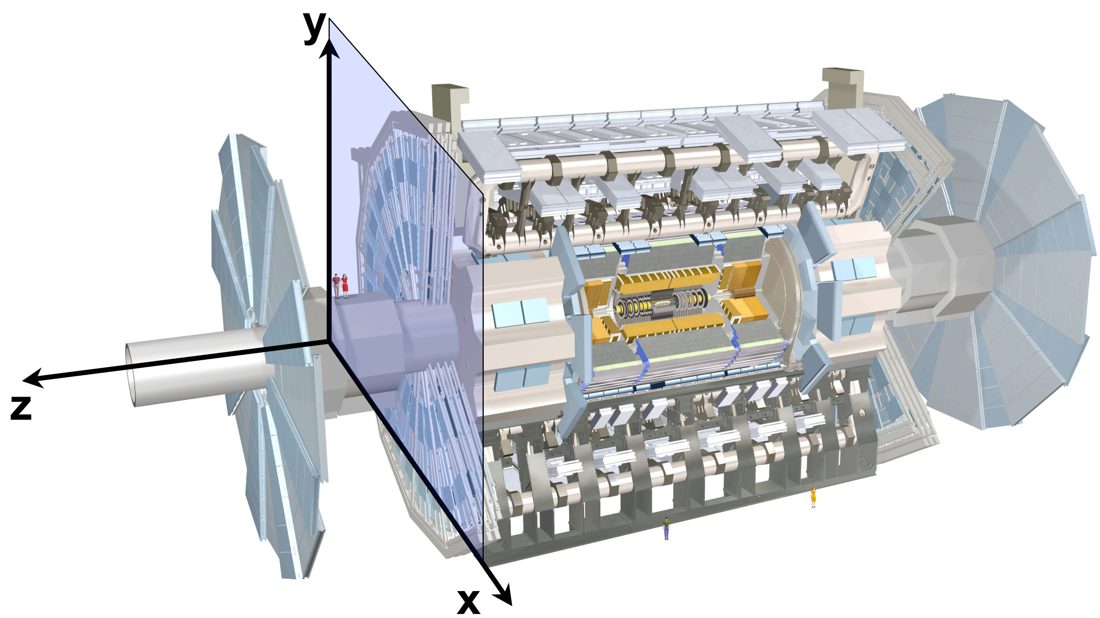

Figure 2.4. An illustration of the ATLAS detector, shown along with the rectangular coordinate system used. The z axis is in the direction of the LHC beam, the y axis points upward, and the x axis points towards the center of the LHC ring. The shaded plane shown in the figure is the transverse plane.

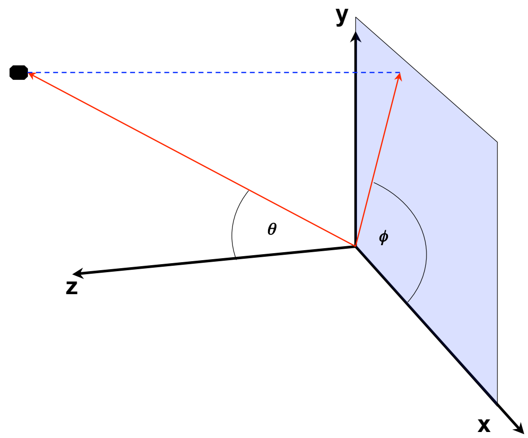

Figure 2.5. Schematic demonstrating θ and ϕ coordinates, with a particle's momentum vector shown by the solid black line from the origin to the large black point. The commonly used position coordinate η can be obtained from the θ angle.

The remainder of this chapter will focus only on those aspects of the detector necessary for data analysis using electrons, namely, the inner detector, the electromagnetic calorimeter and the trigger.

2.2.1. Inner Detector

The Inner Detector is used to identify and measure the properties of the tracks of charged particles. As there will be up to 1000 particles produced every 25 nanoseconds [13] when the LHC reaches it's design instantaneous luminosity of $10^{34} cm^2/s$, it is important that the tracking systems have good resolution, in order to separate and accurately identify individual tracks associated with specific particles.

An illustration of the Inner Detector is shown in Figure 2.6. As can be seen, the detector consists of several tracking subsystems: the Pixel detector, the Silicon detector and the Transition Radiation Tracker (TRT). It also contains a central solenoid magnet, which produces the 2 T field in which the entire Inner Detector is immersed. The magnetic field causes the trajectories of charged particles to bend, which allows for momentum and charge measurement from the curvature of their tracks. The entire Inner Detector covers a range of $|\eta| < 2.5$.

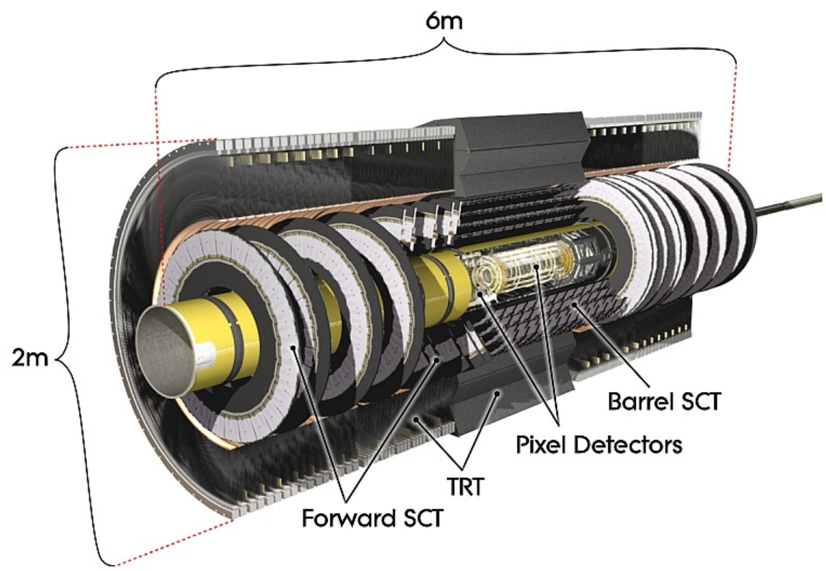

Figure 2.6. The ATLAS inner detector has three tracking subsystems: the Pixel detector, the Silicon detector, and the TRT. It also contains a central solenoid magnet [13].

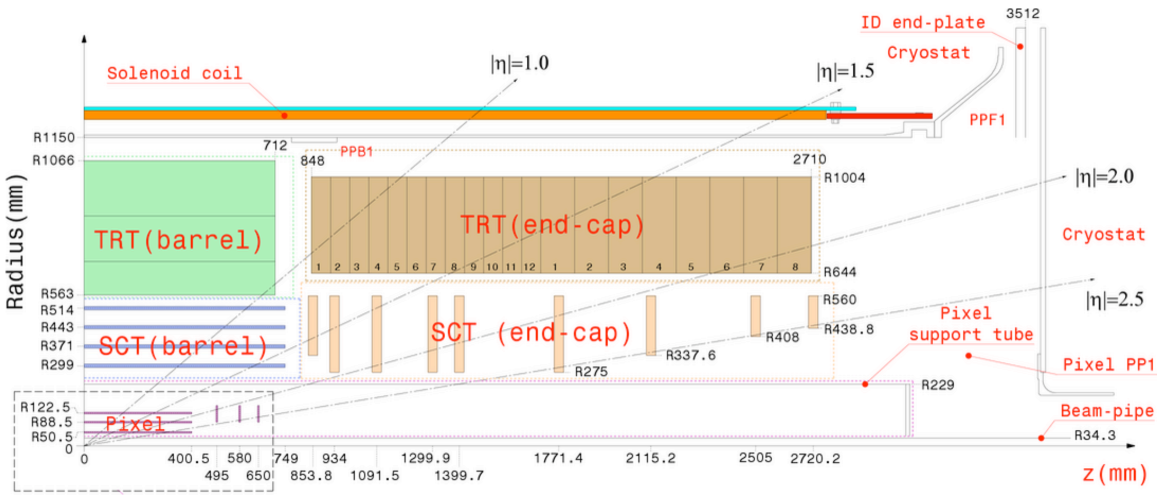

Figure 2.7. A schematic of the Inner Detector illustrating coverage in η [13].

2.2.1.1. *Pixel detector*

The pixel and silicon detectors are known as the 'precision trackers,' due to the fact that they have the best spatial resolution. These detectors surround the beam axis, wrapped around it, in the central region of the detector known as the barrel (see Figure 2.7). In the portions of the detector known as the endcaps, the detectors are perpendicular to the beam axis, mounted on disks.

The pixel modules each have a minimum pixel size of 50 $\times$ 400 μm^2. The modules are organized in different layers, with the three layers of the barrel region segmented cylindrically and the three layers of the endcaps regions stacked in the transverse direction. The three layers of the barrel contain a combined 1456 tracking modules and the each endcap contains 288 modules. The pixel detector has approximately 80.4 million read out channels. The position resolution of this detector is 15 μm in the $R-\phi$ direction and 100 μm in the z direction.

2.2.1.2. *Silicon detector*

The silicon detector, also called the semiconductor tracker (SCT), consists of 4088 silicon strip modules. These modules are arranged in four layers in the barrel and nine disks on each endcap. In the barrel, the strips are positioned at a small angle (40 mrad) in order to measure both position coordinates. In the endcap, strips running parallel to the beam axis are also used. There are a total of 6.3 million read out channels in the SCT. The position resolution of this detector is 17 μm in the $R - \phi$ direction and 580 μm in the z direction.

2.2.1.3. *Transition radiation track detector (TRT)*

The TRT, which has coverage of $|\eta|$ <2.0, can record up to 36 hits per track. This detector utilizes 4 mm in diameter straw tubes reinforced with carbon fibers and containing a 30 μm in diameter gold-plated tungsten wire at the center. The tubes are filled with a mixture of xenon (70%), carbon dioxide (27%) and oxygen (3%) gasses [1]. The mixture is chosen for both stability and to enhance the rate of transition radiation. In this process of ionization, a photon is emitted when a charged particle moves through the tracker. This process occurs at a higher rate for lighter and faster moving particles (such as electrons) than for heavier, slower moving ones (such as charged pions). Therefore, in addition to track reconstruction, information from the TRT allows for a certain degree of background rejection.

The barrel of the TRT has 105,088 readout channels. It contains 144 cm long straws that run parallel to the beam axis. The TRT endcaps contain 122,880 readout channels each. They contain 39 cm long straws that run radially from the beam axis outward, and are arranged into 20 separate wheels. The TRT only provides position information in the $R - \phi$ direction, and has an accuracy of approximately 130 μm.

2.2.2. Calorimeters

The ATLAS calorimeters are used to measure the energies and positions of various particles via total absorption. The process of absorption leads to the original particles showering, producing other particles upon interaction with the material. Particle showers will first pass through the electromagnetic calorimeter, which is closer to the beam pipe, and secondly through the hadronic calorimeter if they have not already been fully absorbed. Both the electromagnetic and hadronic calorimeters are sampling calorimeters, which means that they have alternating layers of absorber material where the particle showers are produced, and active (scintillating in the hadronic calorimeter and ionizing in the electromagnetic calorimeter) material where energies are measured. This also means that extensive calibrations are necessary to correct the total deposited energy for the fraction of energy absorbed in the inert (absorber) material.

The electromagnetic calorimeter is specifically designed to measure the properties of particles that interact electromagnetically, causing incident particles to produce electromagnetic showers until total absorption of the showering particles occurs. Electromagnetic showers, shown in Figure 2.8a, contain only electromagnetic particles.

The hadronic calorimeter causes particles such as nucleons, mesons, or other particles made of quarks, to shower hadronically when they enter the calorimeter. The incident particle interacts with the absorber material via the strong force; the particles then produced in the hadronic shower may interact with the material in the detector via the strong force, or weakly or electromagnetically (seen in Figure 2.8b). Consequently, some hadronic showers will also be partially detected by the electromagnetic calorimeter.

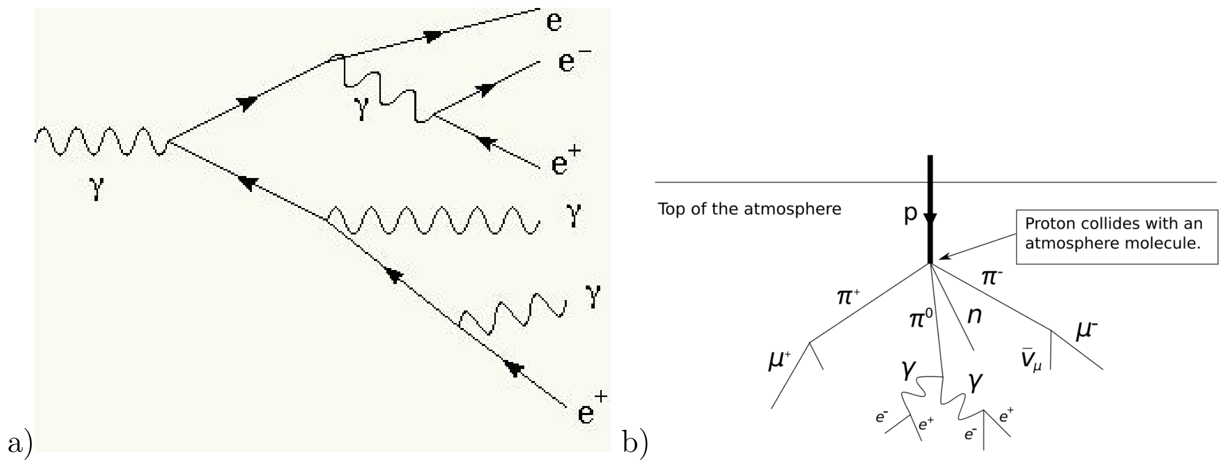

Figure 2.8. a) An example of an electromagnetic shower. A photon enters the absorber material of the electromagnetic calorimeter, and interacts with the material by conversion into an electron-positron pair. The electrons further shower by radiating photons (Bremsstrahlung). b) An example of a hadronic shower. A proton enters the absorber material, which in the figure is the Earth's atmosphere, and produces a particle shower. [95].

The entire calorimeter consists of three cryostats: a central barrel, and two endcaps. The barrel cryostat contains the Electromagnetic Barrel Calorimeter (EMBC). Each endcap cryostat contains an Electromagnetic Endcap Calorimeter (EMEC), a Hadronic Endcap Calorimeter (HEC) and a Forward Calorimeter (FCAL). The cryostats are responsible for temperature control.

2.2.2.1. Electromagnetic (EM) calorimeter

The electromagnetic calorimeter measures the energies of electrons and photons with full coverage in ϕ and coverage up to $|\eta|$ <4.9. It contains the EMEC ($1.375 < |\eta| < 3.2$), the EMBC ($|\eta| < 1.475$) and the FCAL ($3.1 < |\eta| < 4.9$). In the EMEC and the EMBC, the absorber layers are made of stainless steel and lead, which alternate with the ionizing Liquid Argon (LAr). Readout electrodes made from copper and kapton are kept at high voltage and are inserted in the center of the LAr layers. The FCAL is positioned close to the beam pipe and is made from copper and tungsten. All components can be seen in Figure 2.9.

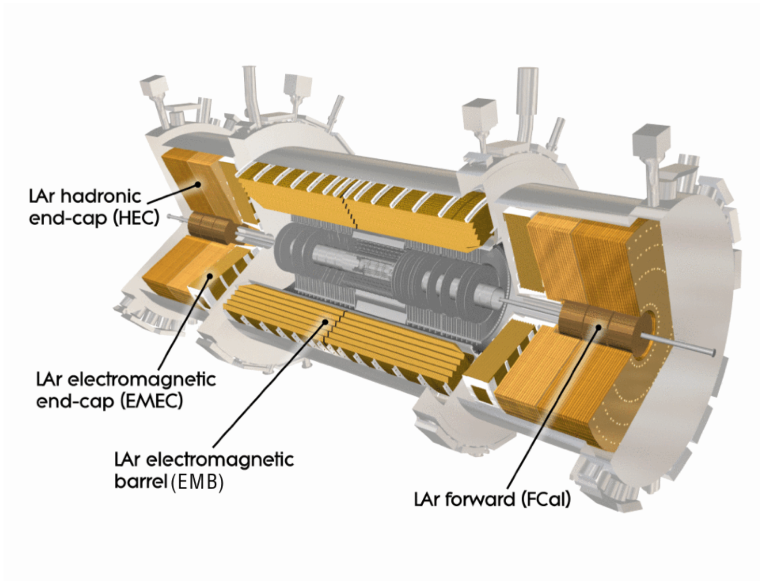

Figure 2.9. An illustration of the Liquid Argon calorimeter. The LAr calorimeter contains the EM calorimeter and the hadronic LAr calorimeter (HEC), which is discussed in the next section.

The EM calorimeter components are built in a series of layers, the number of which varies based on the specific partition and the region in η. The number of layers can be seen in Table 2.1. In addition to longitudinal segmentation, the calorimeter is also segmented into smaller units called cells. The size of the cells varies as well, based on partition and position in η. The cell size is given in Table 2.2.

Table 2.1. Number of layers in the EM calorimeter.

Partition	η region	Number of layers
EMBC	$\lvert\eta\rvert < 1.35$	4
	$1.35 < \lvert\eta\rvert < 1.475$	3
EMEC	$1.375 < \lvert\eta\rvert < 1.5$	2
	$1.5 < \lvert\eta\rvert < 1.8$	4
	$1.8 < \lvert\eta\rvert < 2.5$	3
	$2.5 < \lvert\eta\rvert < 3.2$	2
FCAL	$3.1 < \lvert\eta\rvert < 4.9$	3

Table 2.2. Cell size in the EM calorimeter [10].

Partition	η region	Layer	Cell size ($\Delta\eta \times \Delta\phi$)
EMBC	$\lvert\eta\rvert < 1.35$	Layer 0 (Presampler)	0.025×0.1
	$\lvert\eta\rvert < 1.475$	Layer 1	0.003×0.1
	$\lvert\eta\rvert < 1.475$	Layer 2	0.025×0.025
	$\lvert\eta\rvert < 1.475$	Layer 3	0.05×0.025
EMEC	$1.375 < \lvert\eta\rvert < 1.5$	Layer 1	0.025×0.1
	$1.5 < \lvert\eta\rvert < 1.8$	Layer 1	0.003×0.1
	$1.8 < \lvert\eta\rvert < 2.0$	Layer 1	0.006×0.1
	$2.0 < \lvert\eta\rvert < 2.5$	Layer 1	0.1×0.1
	$1.375 < \lvert\eta\rvert < 2.5$	Layer 2	$0.025 \times 0.0.025$
	$2.5 < \lvert\eta\rvert < 3.2$	Layer 2	0.1×0.1
	$1.5 < \lvert\eta\rvert < 2.5$	Layer 3	0.05×0.025
FCAL	$3.1 < \lvert\eta\rvert < 4.9$	All layers	0.2×0.2

The small cell size (also referred to as fine granularity) of the EM calorimeter can be exploited to reject background, as it allows for detailed knowledge of the EM shower's shape. This is detailed in Chapter 3.

A final important point about the EM calorimeter is its energy resolution. For physics analysis, it is essential to have good electromagnetic energy resolution, as this propagates directly to the mass resolution of a particle decaying to electrons or photons (such as a Z').[3] The electromagnetic energy resolution of the EM calorimeter is described by the following equation:

$$\frac{\sigma_E}{E} = \frac{b}{\sqrt{E}} \oplus 0.7\%, \tag{2.2}$$

where b is known as the sampling term. The sampling term, and thus the energy resolution, varies depending on position in $|\eta|$. Figure 2.10 shows the sampling term for electrons and photons as a function of $|\eta|$. The best value for this term is in the center of the calorimeter, where $b = 8.7\%$. Due to the increasing amount of material present, this term worsens until it reaches it's highest value of 21% at $\eta = 1.55$.

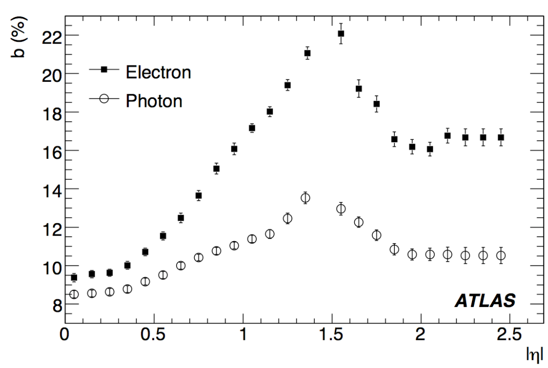

Figure 2.10. Sampling term as a function of η position, shown for electrons (black squares) and photons (open circles). Variation in the sampling term is due to the change in the amount of material in front of the calorimeter as a function of η [11].

[3]Good position resolution is also important, as the invariant mass of such a particle is given by $M = \sqrt{2E_1E_2(1 - cos\theta_{12})}$. The position resolution for electrons is given by the resolution of the tracking systems, already described.

2.2.3. Trigger

At peak instantaneous luminosity, events will be produced in ATLAS at a rate of 40 MHz. This rate must be brought down to 200 Hz, which is the rate at which events can be written to storage disk. This reduction is accomplished by use of the trigger, a three-level scheme for keeping interesting events and discarding, before writing to disk, those less interesting [14].

2.2.3.1. L1: the Level 1 Trigger

Via high-speed hardware links into the calorimeters and muon systems, the L1 trigger simply rejects events based on object multiplicity and energy thresholds. This must be done within 2.5 μs of an event, reducing the event rate from 40 MHz to 75 kHz. The objects that are used in the trigger decision are not fully-reconstructed physics objects, such as electrons or muons. Rather, the L1 trigger uses as it's input: electromagnetic clusters in the EM calorimeter (described in Chapter 3); tau particles; missing transverse energy; the scalar sum of transverse energies recorded in the calorimeters; and total transverse energy of jets reconstructed at Level 1. All online (at the trigger level) energies are computed using cell sizes of 0.1×0.1.

By varying the transverse energy threshold, imposing trigger-level isolation requirements or varying the number of cells at the online level used to define the cluster, there are up to 8 different possible thresholds at Level 1 for EM objects.

2.2.3.2. L2: the Level 2 Trigger

In contrast to the L1 trigger, which uses energy thresholds read by direct hardware links to the detector, the L2 trigger uses software-based algorithms to further analyze those events accepted at L1. This is accomplished by defining a region of interest

(ROI) around the object triggered at L1–the E_T threshold used and the η,ϕ coordinate of the triggered object from L1 is input to the L2 trigger as a 'seed.' The seed is analyzed using the smaller granularity available from the detector systems (as opposed to the online granularity described in the previous section), within the ROI. Further information from the detector, not available at L1, such as energies in smaller cell size and information from the Inner Detector, can be used at L2, allowing for higher purity of retained events.

The L2 trigger must process a new event every 40 ms, but the actual processing time is closer to 10 μs. At this level, the rate is reduced from 75 kHz to 2 kHz.

2.2.3.3. EF: the Event Filter Trigger

The Event Filter trigger is the final step in reducing the rate of events to one that can be manageably written to storage. Events are read into this trigger at the 2 kHz rate provided by L2, and ultimate reduction of the rate to 200 Hz is necessary at this point. The EF trigger accomplishes this by spending about 4 s processing time per event, taking seeds from L2 (analogous to the procedure between L2 and L1) and analyzing them with the same algorithms used for offline analysis. Therefore, the full event and physics object information is available to the EF trigger, allowing the required large number of events to be rejected while still maintaining high purity.

Any of the triggers described may be prescaled in order to lower the bandwidth. This entails writing to disk only a fraction of the events passing the trigger. It is possible to prescale triggers without stopping a run. The trigger configuration is decided not run-by-run, but in time intervals about two minutes long called luminosity blocks. A single luminosity block is the smallest unit at which data quality are monitored, and the trigger conditions are always consistent within such a block.

Chapter 3

ELECTRON RECONSTRUCTION AND IDENTIFICATION

This in effect is, the faith of all physicists; the deeper we seek, the more is our wonder excited, the more is the dazzlement for our gaze.

Abdus Salam (1926-1996)
Pakistani physicist, Nobel laureate

3.1. Electron reconstruction in ATLAS

The physics analyses described in this thesis are dependent on accurate reconstruction of electrons, accomplished with the use of the LAr calorimeter (described in Section 2.2.2.1) and the tracking systems of the Inner Detector (described in Section 2.2.1).

In ATLAS, this is handled using three separate algorithms:

- The **standard eγ** algorithm is cluster-seeded and uses a sliding-window approach to locate the cluster, an energy deposit with characteristics described in Section 3.2, in the calorimeter. The electron's cluster is later matched with a track, also described in Section 3.2. The standard algorithm is used for electrons with $p_T > 3$ GeV, in the region $|\eta| < 2.47$.

- The **soft electron** algorithm is track-seeded and designed to reconstruct very low p_T electrons ($p_T < 3$ GeV) efficiently. Each track is later matched with a cluster. Such objects are not used in the analyses presented here and details of the soft electron algorithm are not discussed.

- The **forward electron** algorithm is used to reconstruct objects in the far forward regions of the LAr calorimeter where there is no tracking system available ($2.5 < |\eta| < 4.9$). The reconstruction of forward electrons differs from the standard eγ algorithm, not only due to the lack of track information, but also due to the large cell size in the Forward Calorimeter.

3.2. Standard eγ

Reconstruction of standard eγ objects begins with an energy deposition in the LAr calorimeter, known as a 'cluster.'[1] Clusters are identified by the sliding window approach. This algorithm is not specific to particle physics. For example, in Figure 3.1 the sliding window algorithm is illustrated using density of tree cover in a region.

[1] Not every single cell or group of cells with a recorded energy goes on to become a cluster. The precise requirements for cluster definition are defined in this section.

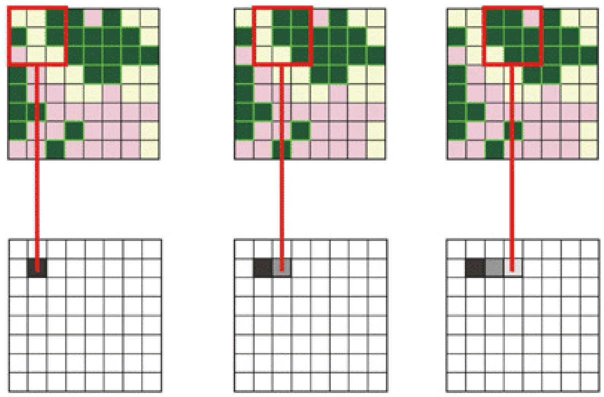

Figure 3.1. Sliding window algorithm [86]: An input map (top) is analyzed within an analysis window (red square) and the density of tree cover is calculated. The result is recorded in an output map (bottom) in the pixel corresponding to the center of the analysis window, with lighter color signifying higher ratio of forest (green) to agriculture (tan) and urban (pink) pixels. The analysis window starts in the upper-left corner and moves left-to-right pixel by pixel. At the end of the first row the analysis window moves down one pixel and begins left-to-right in the same fashion until the output map is complete. The output map can be analyzed for the pixel with the highest density, corresponding to the analysis window with most tree cover.

3.2.1. Sliding window method in ATLAS

In ATLAS, a completely analogous approach to that shown in Figure 3.1 is used for cluster finding. Instead of the pixels in the illustration, the inputs are known as calorimeter towers [94]. These towers are built within $|\eta| \leq 2.5$, the region for which the standard eγ reconstruction algorithm is in general valid. The towers are made by dividing the $\eta \times \phi$ space of the electromagnetic barrel and endcaps into a grid consisting of 200 divisions in η and 256 in ϕ, with size $\Delta\eta \times \Delta\phi$ of 0.025×0.025, which in the second layer of the calorimeter corresponds to the size of a single cell. Within each division, the energy of all encompassed calorimeter cells in all layers is combined to yield the total 'tower' energy; the combination of all cells in all layers is referred to as the tower.

3.2.2. Precluster formation

The tower grid is used as the input for cluster finding. Towers are scanned using a 5×5 analysis window, with a 1×1 unit corresponding to a single tower. Those 5×5 regions with energy greater than 3 GeV are classified as 'preclusters.' The analysis window size is chosen to maximize cluster finding efficiency, but the large size may result in duplicate clusters for a single particle. Therefore, steps must be taken to remove duplicate preclusters.

3.2.3. Duplicate precluster removal

The first of these steps is identifying each precluster's position, the tower that is the energy-weighted barycenter in a $3{\times}3$ window around the precluster's geometrically central tower. Next, preclusters with position within 2×2 towers of each other are considered duplicates. In this situation, the precluster with the highest E_T is kept as the final cluster, and the others are discarded.

3.2.4. Clusters from preclusters

The tower signifying the precluster's position is used as the geometric center of the cluster formed from it. The rest of the cluster is composed of those calorimeter cells in the region surrounding the center. The region size depends on the type of particle and area of the detector the cluster lies within. For electron clusters in the barrel the size is 3×7 cells and in the endcaps it is 5×5 cells. The asymmetric size in the barrel is to accommodate the fact that clusters in the barrel are larger in ϕ.

3.2.5. Track association

The next step in standard eγ electron reconstruction is cluster-track association. There are two categories of tracks: those which consist of only hits in the TRT [26], and those which have hits in additional tracking systems.

3.2.5.1. Non-TRT-only tracks

For tracks with hits in additional systems, track-cluster association is performed in two steps. First, the η and ϕ positions at the origin of the track are matched to the η and ϕ position of the cluster. If these positions agree within 0.05 units in η and 0.1 units in ϕ, the track is kept for the second step. A less stringent requirement in ϕ is used to keep the electron reconstruction efficiency independent of electron p_T. The second step extrapolates the track through each calorimeter layer using the location of the interaction point. The difference in η and ϕ between the track position and the cluster position in each layer is recorded. Finally, for all candidate tracks the distance between the track position and the cluster position in the second layer is used to select the best track match, the one with the smallest such distance.

3.2.5.2. TRT-only tracks

In the case of tracks that only leave hits in the TRT, the position information is not as precise. Therefore, a limit on the maximal distance between track and cluster is not imposed and the track with the smallest track-cluster distance in η in the second layer is used.

3.3. Forward electron

The forward electron reconstruction algorithm is valid within the range $2.5 < |\eta| < 4.9$, in which there is no tracking and electron reconstruction must rely entirely on calorimeter information. Because of this it is impossible to distinguish between electrons and photons, and it may be more accurate to call forward electrons 'forward EM' objects. However, all such objects are classified as electrons.

3.3.1. Topological clusters

Due to the coarser granularity of the calorimeter in the forward region, a different clustering algorithm using reconstructing topological ('topo') clusters is employed. Instead of the methodical approach of the sliding window algorithm, the generation of topological clusters is done by grouping together calorimeter cells with energy higher than that expected due to normal electronic noise. This results in a main feature of 'topo' clusters, variable size.

This conglomeration of cells imposes a lower limit on the energy of any cell accepted into the cluster, expressed as a fraction of the expected noise level for that specific cell. For the first cell, called the seed, the required energy threshold is $|E| \geq 4\sigma$. This means that the cell energy, E, must be larger than four standard deviations in comparison to the expected noise level. For surrounding cells that may be added a lower threshold is allowed; neighboring cells passing the threshold $|E| \geq 2\sigma$ are added to the seed to form the cluster [89]. Neighboring cells to the seed are added to the cluster's core if they pass an intermediate threshold. Keeping the cells on the perimeter that pass only this lower energy requirement allows the full cluster to be reconstructed, which is very useful when calculating cluster moments used in forward electron identification. These will be described further in Section 3.4.4.

Only those topo clusters with transverse energy greater than 5 GeV are accepted as forward electrons. The electron's position is given by the energy weighted barycenter of the cluster across all layers.

3.4. Electron identification

The process used to identify clusters with matching tracks as electrons accepts many fakes in addition to real electrons. Most fake particles are from the decay of hadrons, such as charged pions. These fakes differ in several respects from real electrons produced at the interaction point of pp collisions, and sets of electron selection criteria have been designed to discriminate against them. These criteria are ranked loose, medium and tight, with 'loose' having the highest efficiency and lowest background rejection, while 'tight' has the best background rejection while maintaining an efficiency suitable for physics analyses with a high event rate, e.g., studies of the properties of W and Z bosons.

Different selections are used for standard and forward electrons. Although the forward electron identification criteria also aim to reduce background from hadronic decays, there are only two levels of identification in the forward region–loose and tight. As with the standard electrons, the loose forward electron selection is more efficient than tight, but suppresses a lower amount of background. In the forward region, it is not possible to have as varied a set of identification requirements due to the lack of tracking, and also due to the large calorimeter cells of the forward region.

In all sets of requirements described, the cuts on the parameters within the selection criteria usually vary with the electron's location in η and transverse momentum. In this case, the numerical cut values used are presented after a description of the quantity on which requirements are imposed [8][9].

3.4.1. Standard loose electrons

The loose criteria consists of requirements on [25]:

- The location of the electron's cluster in η, used as an input to determine the cut value on the other criteria.

- $R_\eta(37)$, the ratio in energies between a 3 cells $\times$7 cells and a 7 cells $\times$7 cells area around the electron's cluster in the second layer. This value gives a measure of how much of the cluster's energy is contained within it's core. (See Table 3.2.)

- Cluster lateral (in η direction) width in the second layer. Fakes from hadrons tend to deposit broader clusters. (See Table 3.3.)

- Amount of energy deposited in the first layer of the hadronic calorimeter behind the cluster. (See Table 3.1.)

3.4.2. Standard medium electrons

The medium criteria builds on the loose selection, adding requirements on the electron's cluster in the strips (first) calorimeter layer. This layer has finer granularity than the second layer (see Figure 3.2) and therefore can more effectively reject background from hadrons (see Figure 3.3). The medium criteria consists of cuts on:

- All requirements from the loose definition.

- Fraction of the electron's total cluster energy found in the strips layer, required to be less than 5%.

- Energy of the second highest energy cell in the strips layer, used as input to the next cut.

- Energy difference between the first highest and second highest energy cells in the strips layer, divided by the sum of their energies. (See Table 3.4.) This cut is designed to detect the double-cluster pattern shown in Figure 3.3b. Neutral meson decay is usually the source of a cluster with double maxima.

- Width of the electron's cluster in the strips layer. (See Table 3.5.)
- The electron's track must have at least one hit in the pixel detector.
- The electron's track must have at least seven hits in the silicon detector.
- The absolute value of the distance of the track's closest approach to the interaction vertex, $|d_0|$, is less than 5 millimeters.
- The distance $|\Delta\eta|$, which is the difference between the cluster η and the η of the track (extrapolated into the calorimeter) in the strips layer, must be less than 0.01. The use of stringent track-cluster matching requirements decreases the background from the decay products of hadronic showers.

3.4.3. Standard tight electrons

The tight criteria improve on the medium by requiring even more strict track-cluster matching requirements. Not only does this serve to reduce hadronic background, it also reduces the rate of electron charge misidentification due to an incorrect track being assigned to a true electron's cluster. Additionally, this series of cuts uses information from the TRT, which is quite powerful for discriminating against hadronic background. The tight criteria consists of:

- All requirements from the medium definition.
- At least one of the electron's track's hits in the pixel detector must be in the first layer.
- The distance $|\Delta\phi|$, which is the difference between the cluster ϕ and the ϕ of the track (extrapolated into the calorimeter) in the second layer, must be less than 0.02.

- Comparison of cluster energy, E, taken from the calorimeter, and track momentum, p, is used. For true electrons, the value $\frac{E}{p}$ is expected to be close to one. The minimum $\frac{E}{p}$ values allowed are shown in Table 3.6 and the maximum values allowed are shown in Table 3.7.

- More stringent requirement on the distance between the cluster's η and the track (extrapolated) η in the strips layer is used (smaller distance required). The value of $|\Delta\eta|$ must be less than 0.005.

- Smaller value than medium for the absolute value of the distance of the track's closest approach is required. The impact parameter $|d_0|$ must be less than 1 millimeter.

- Check whether the electron matches in position with a reconstructed photon. This can eliminate fakes from photon conversions.

- Number of hits the electron's track has in the TRT. (See Table 3.8.)

- Fraction of TRT hits that are high-threshold hits. Tracks with a low fraction of high-threshold TRT hits are more likely to result from hadron fakes. (See Table 3.9.)

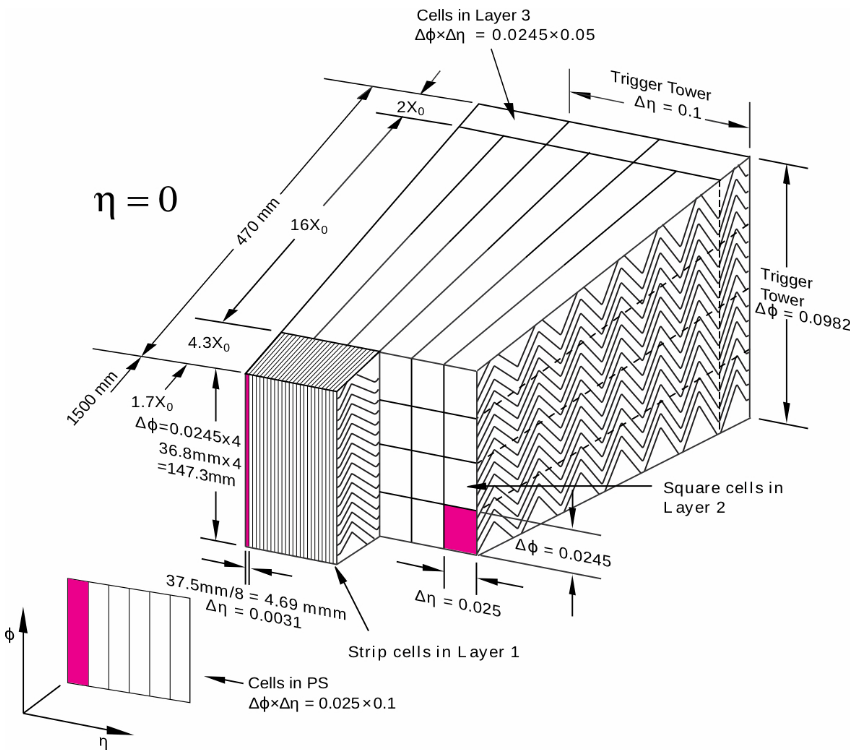

Figure 3.2. Illustration of cell size in each of the three layers of the LAr calorimeter [12].

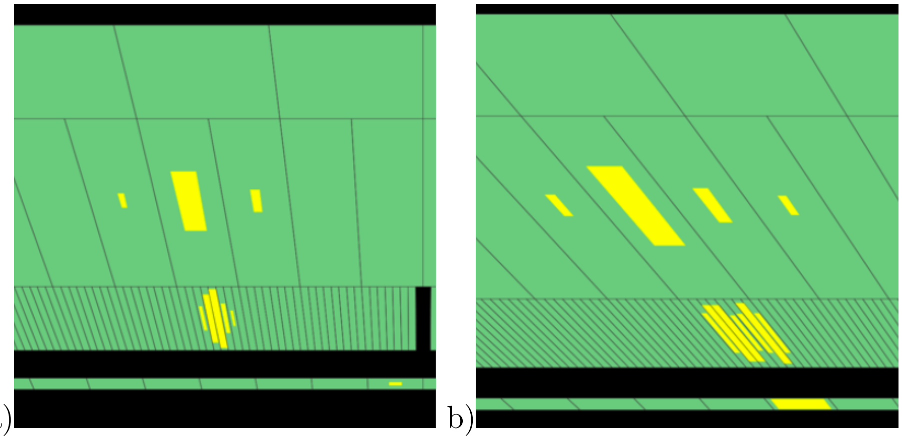
a) b)

Figure 3.3. a) A photon candidate with cluster shown in the first and second layers and b) a neutral pion candidate. The cluster of a prompt electromagnetic object (photon) is narrower than the pion's cluster. This is true in both layers, but notably in the first, where the 'double cluster' of the $\pi^0 \to \gamma\gamma$ decay is seen [27].

Table 3.1. Cuts on hadronic leakage in bins of electron p_T and $|\eta|$.

p_T (GeV)	$|\eta|$ =	$[0, 0.1)$	$[0.1, 0.6)$	$[0.6, 0.8)$	$[0.8, 1.15)$	$[1.15, 1.37)$
$[0, 5)$		0.031	0.031	0.021	0.021	0.019
$[5, 10)$		0.018	0.018	0.016	0.015	0.016
$[10, 15)$		0.015	0.015	0.014	0.014	0.016
$[15, 20)$		0.012	0.012	0.010	0.010	0.012
$[20, 30)$		0.010	0.010	0.010	0.010	0.010
$[30, 40)$		0.008	0.008	0.008	0.008	0.008
$[40, 50)$		0.008	0.008	0.008	0.008	0.008
$[50, 60)$		0.008	0.008	0.008	0.008	0.008
$[60, 70)$		0.008	0.008	0.008	0.008	0.008
$[70, 80)$		0.008	0.008	0.008	0.008	0.008
≥ 80		0.008	0.008	0.008	0.008	0.008
p_T (GeV)	$|\eta|$ =	$[1.37, 1.52)$	$[1.52, 1.81)$	$[1.81, 2.01)$	$[2.01, 2.37)$	$[2.37, 2.47)$
$[0, 5)$		0.028	0.065	0.065	0.046	0.034
$[5, 10)$		0.028	0.053	0.038	0.028	0.025
$[10, 15)$		0.020	0.039	0.032	0.027	0.023
$[15, 20)$		0.015	0.029	0.022	0.015	0.021
$[20, 30)$		0.010	0.020	0.015	0.014	0.014
$[30, 40)$		0.010	0.014	0.015	0.010	0.010
$[40, 50)$		0.010	0.015	0.015	0.010	0.010
$[50, 60)$		0.010	0.015	0.015	0.010	0.010
$[60, 70)$		0.010	0.015	0.015	0.010	0.010
$[70, 80)$		0.010	0.015	0.015	0.010	0.010
≥ 80		0.010	0.015	0.015	0.010	0.010

Table 3.2. Cuts on $R_\eta(37)$ in bins of electron p_T and $|\eta|$.

p_T (GeV)	$|\eta|$ =	$[0, 0.1)$	$[0.1, 0.6)$	$[0.6, 0.8)$	$[0.8, 1.15)$	$[1.15, 1.37)$
$[0, 5)$		0.700	0.700	0.700	0.700	0.700
$[5, 10)$		0.700	0.700	0.700	0.700	0.700
$[10, 15)$		0.860	0.860	0.860	0.860	0.860
$[15, 20)$		0.860	0.860	0.860	0.860	0.860
$[20, 30)$		0.930	0.930	0.930	0.925	0.925
$[30, 40)$		0.930	0.930	0.930	0.925	0.925
$[40, 50)$		0.930	0.930	0.930	0.925	0.925
$[50, 60)$		0.930	0.930	0.930	0.930	0.925
$[60, 70)$		0.930	0.930	0.930	0.930	0.925
$[70, 80)$		0.930	0.930	0.930	0.930	0.925
≥ 80		0.930	0.930	0.930	0.930	0.925
p_T (GeV)	$|\eta|$ =	$[1.37, 1.52)$	$[1.52, 1.81)$	$[1.81, 2.01)$	$[2.01, 2.37)$	$[2.37, 2.47)$
$[0, 5)$		0.690	0.848	0.876	0.870	0.888
$[5, 10)$		0.715	0.860	0.880	0.880	0.880
$[10, 15)$		0.730	0.860	0.880	0.880	0.880
$[15, 20)$		0.740	0.915	0.915	0.900	0.900
$[20, 30)$		0.750	0.915	0.920	0.900	0.900
$[30, 40)$		0.790	0.915	0.920	0.900	0.900
$[40, 50)$		0.790	0.915	0.920	0.900	0.900
$[50, 60)$		0.790	0.915	0.920	0.900	0.900
$[60, 70)$		0.790	0.915	0.920	0.900	0.900
$[70, 80)$		0.790	0.915	0.920	0.900	0.900
≥ 80		0.790	0.915	0.920	0.900	0.900

Table 3.3. Cuts on cluster lateral width in bins of electron p_T and $|\eta|$.

p_T (GeV)	$\lvert\eta\rvert$ =	$[0, 0.1)$	$[0.1, 0.6)$	$[0.6, 0.8)$	$[0.8, 1.15)$	$[1.15, 1.37)$
$[0, 5)$		0.014	0.014	0.014	0.014	0.014
$[5, 10)$		0.013	0.013	0.014	0.014	0.014
$[10, 15)$		0.013	0.013	0.014	0.014	0.014
$[15, 20)$		0.012	0.012	0.013	0.013	0.013
$[20, 30)$		0.011	0.011	0.012	0.012	0.013
$[30, 40)$		0.011	0.011	0.012	0.012	0.012
$[40, 50)$		0.011	0.011	0.012	0.012	0.012
$[50, 60)$		0.011	0.011	0.012	0.012	0.012
$[60, 70)$		0.011	0.011	0.012	0.012	0.012
$[70, 80)$		0.011	0.011	0.012	0.012	0.012
≥ 80		0.011	0.011	0.012	0.012	0.012
p_T (GeV)	$\lvert\eta\rvert$ =	$[1.37, 1.52)$	$[1.52, 1.81)$	$[1.81, 2.01)$	$[2.01, 2.37)$	$[2.37, 2.47)$
$[0, 5)$		0.028	0.017	0.014	0.014	0.014
$[5, 10)$		0.026	0.017	0.014	0.014	0.014
$[10, 15)$		0.025	0.017	0.014	0.014	0.014
$[15, 20)$		0.025	0.017	0.014	0.014	0.014
$[20, 30)$		0.025	0.014	0.013	0.013	0.013
$[30, 40)$		0.025	0.013	0.013	0.013	0.013
$[40, 50)$		0.025	0.013	0.013	0.013	0.013
$[50, 60)$		0.025	0.013	0.920	0.013	0.013
$[60, 70)$		0.025	0.013	0.920	0.013	0.013
$[70, 80)$		0.025	0.013	0.920	0.013	0.013
≥ 80		0.025	0.013	0.920	0.013	0.013

Table 3.4. Cuts on difference between the first highest and second highest cell energy, divided by their sum, in bins of electron p_T and η. A value of '-9999' essentially corresponds to no cut in this bin (any value will be greater than -9999).

p_T (GeV)	$\|\eta\|$ =	$[0, 0.1)$	$[0.1, 0.6)$	$[0.6, 0.8)$	$[0.8, 1.15)$	$[1.15, 1.37)$
$[0, 5)$		0.39	0.39	0.20	0.07	0.06
$[5, 10)$		0.61	0.61	0.32	0.11	0.13
$[10, 15)$		0.67	0.67	0.61	0.43	0.32
$[15, 20)$		0.75	0.75	0.67	0.51	0.47
$[20, 30)$		0.835	0.835	0.835	0.73	0.70
$[30, 40)$		0.835	0.835	0.835	0.73	0.70
$[40, 50)$		0.835	0.835	0.835	0.73	0.70
$[50, 60)$		0.835	0.835	0.835	0.73	0.70
$[60, 70)$		0.835	0.835	0.835	0.73	0.70
$[70, 80)$		0.835	0.835	0.835	0.73	0.70
≥ 80		0.835	0.835	0.835	0.73	0.70
p_T (GeV)	$\|\eta\|$ =	$[1.37, 1.52)$	$[1.52, 1.81)$	$[1.81, 2.01)$	$[2.01, 2.37)$	$[2.37, 2.47)$
$[0, 5)$		-9999.	0.07	0.43	0.75	-9999.
$[5, 10)$		-9999.	0.12	0.51	0.62	-9999.
$[10, 15)$		-9999.	0.36	0.82	0.82	-9999.
$[15, 20)$		-9999.	0.43	0.86	0.84	-9999.
$[20, 30)$		-9999.	0.8	0.9	0.9	-9999.
$[30, 40)$		-9999.	0.8	0.9	0.9	-9999.
$[40, 50)$		-9999.	0.8	0.9	0.9	-9999.
$[50, 60)$		-9999.	0.8	0.9	0.9	-9999.
$[60, 70)$		-9999.	0.8	0.9	0.9	-9999.
$[70, 80)$		-9999.	0.8	0.9	0.9	-9999.
≥ 80		-9999.	0.8	0.9	0.9	-9999.

Table 3.5. Cuts on cluster width in the first layer, in bins of electron p_T and η. A value of '9999' essentially corresponds to no cut in this bin (all clusters are narrower than 9999 in η).

p_T (GeV)	$\|\eta\|$ =	$[0, 0.1)$	$[0.1, 0.6)$	$[0.6, 0.8)$	$[0.8, 1.15)$	$[1.15, 1.37)$
$[0, 5)$		3.48	3.48	3.78	3.96	4.20
$[5, 10)$		3.18	3.18	3.54	3.90	4.02
$[10, 15)$		2.85	2.85	3.20	3.40	3.60
$[15, 20)$		2.76	2.76	2.92	3.30	3.45
$[20, 30)$		2.50	2.50	2.70	3.14	3.23
$[30, 40)$		2.45	2.45	2.70	2.98	3.17
$[40, 50)$		2.27	2.27	2.61	2.90	3.17
$[50, 60)$		2.27	2.27	2.61	2.90	3.17
$[60, 70)$		2.27	2.27	2.61	2.90	3.17
$[70, 80)$		2.27	2.27	2.61	2.90	3.17
≥ 80		2.27	2.27	2.61	2.90	3.17
p_T (GeV)	$\|\eta\|$ =	$[1.37, 1.52)$	$[1.52, 1.81)$	$[1.81, 2.01)$	$[2.01, 2.37)$	$[2.37, 2.47)$
$[0, 5)$		9999.	4.02	2.70	1.86	9999.
$[5, 10)$		9999.	3.96	2.70	1.80	9999.
$[10, 15)$		9999.	3.70	2.40	1.72	9999.
$[15, 20)$		9999.	3.67	2.40	1.72	9999.
$[20, 30)$		9999.	3.58	2.32	1.59	9999.
$[30, 40)$		9999.	3.52	2.25	1.58	9999.
$[40, 50)$		9999.	3.36	2.25	1.55	9999.
$[50, 60)$		9999.	3.36	2.25	1.55	9999.
$[60, 70)$		9999.	3.36	2.25	1.55	9999.
$[70, 80)$		9999.	3.36	2.25	1.55	9999.
≥ 80		9999.	3.36	2.25	1.55	9999.

Table 3.6. Cuts on minimum allowed value of $\frac{E}{p}$, in bins of electron p_T and η.

p_T (GeV)	$\lvert\eta\rvert$ =	$[0, 0.1)$	$[0.1, 0.6)$	$[0.6, 0.8)$	$[0.8, 1.15)$	$[1.15, 1.37)$
$[0, 5)$		0.80	0.80	0.80	0.80	0.80
$[5, 10)$		0.80	0.80	0.80	0.80	0.80
$[10, 15)$		0.80	0.80	0.80	0.80	0.80
$[15, 20)$		0.80	0.80	0.80	0.80	0.80
$[20, 30)$		0.80	0.80	0.80	0.80	0.80
$[30, 40)$		0.70	0.70	0.70	0.70	0.70
$[40, 50)$		0.70	0.70	0.70	0.70	0.70
$[50, 60)$		0.70	0.70	0.70	0.70	0.70
$[60, 70)$		0.70	0.70	0.70	0.70	0.70
$[70, 80)$		0.70	0.70	0.70	0.70	0.70
≥ 80		0.00	0.00	0.00	0.00	0.00
p_T (GeV)	$\lvert\eta\rvert$ =	$[1.37, 1.52)$	$[1.52, 1.81)$	$[1.81, 2.01)$	$[2.01, 2.37)$	$[2.37, 2.47)$
$[0, 5)$		0.80	0.80	0.80	0.80	0.80
$[5, 10)$		0.80	0.80	0.80	0.80	0.80
$[10, 15)$		0.80	0.80	0.80	0.80	0.80
$[15, 20)$		0.80	0.80	0.80	0.80	0.80
$[20, 30)$		0.80	0.80	0.80	0.80	0.80
$[30, 40)$		0.70	0.70	0.70	0.70	0.70
$[40, 50)$		0.70	0.70	0.70	0.70	0.70
$[50, 60)$		0.70	0.70	0.70	0.70	0.70
$[60, 70)$		0.70	0.70	0.70	0.70	0.70
$[70, 80)$		0.70	0.70	0.70	0.70	0.70
≥ 80		0.00	0.00	0.00	0.00	0.00

Table 3.7. Cuts on maximum allowed value of $\frac{E}{p}$, in bins of electron p_T and η.

p_T (GeV)	$\lvert\eta\rvert$ =	$[0, 0.1)$	$[0.1, 0.6)$	$[0.6, 0.8)$	$[0.8, 1.15)$	$[1.15, 1.37)$
$[0, 5)$		2.5	2.5	2.5	2.5	2.5
$[5, 10)$		2.5	2.5	2.5	2.5	2.5
$[10, 15)$		2.5	2.5	2.5	2.5	2.5
$[15, 20)$		2.5	2.5	2.5	2.5	2.5
$[20, 30)$		2.5	2.5	2.5	2.5	2.5
$[30, 40)$		3.0	3.0	3.0	3.0	3.0
$[40, 50)$		3.0	3.0	3.0	3.0	3.0
$[50, 60)$		5.0	5.0	5.0	5.0	5.0
$[60, 70)$		5.0	5.0	5.0	5.0	5.0
$[70, 80)$		5.0	5.0	5.0	5.0	5.0
≥ 80		10.0	10.0	10.0	10.0	10.0
p_T (GeV)	$\lvert\eta\rvert$ =	$[1.37, 1.52)$	$[1.52, 1.81)$	$[1.81, 2.01)$	$[2.01, 2.37)$	$[2.37, 2.47)$
$[0, 5)$		2.5	3.0	3.0	3.0	3.0
$[5, 10)$		2.5	3.0	3.0	3.0	3.0
$[10, 15)$		2.5	3.0	3.0	3.0	3.0
$[15, 20)$		2.5	3.0	3.0	3.0	3.0
$[20, 30)$		2.5	3.0	3.0	3.0	3.0
$[30, 40)$		3.0	3.0	4.0	4.0	3.0
$[40, 50)$		3.0	4.0	5.0	5.0	4.0
$[50, 60)$		5.0	5.0	5.0	5.0	5.0
$[60, 70)$		5.0	5.0	5.0	5.0	5.0
$[70, 80)$		5.0	5.0	5.0	5.0	5.0
≥ 80		10.0	10.0	10.0	10.0	10.0

Table 3.8. Cuts on number of TRT hits required, in bins of electron η. The η range of $|\eta| \leq 2.0$ corresponds to the region where the TRT system exists. The required number of hits is expressed by the function $N(\eta) = d\eta^3 + c\eta^2 + b\eta + a$.

$\|\eta\|$ =	d	c	b	a
$[0, 0.1)$	0	1455	-129.1	18.14
$[0.1, 0.625)$	91.51	-89.96	27.93	14.42
$[0.625, 1.07)$	0	230.2	-403.0	181.3
$[1.07, 1.304)$	0	0	37.29	-25.59
$[1.304, 1.752)$	180.8	-851.8	1323.0	-655.9
$[1.752, 2.0]$	0	0	-70.9	144.8

Table 3.9. Cuts on minimum fraction of high-threshold TRT hits, in bins of electron η.

$\|\eta\|$ =	$[0, 0.1)$	$[0.1, 0.625)$	$[0.625, 1.07)$	$[1.07, 1.304)$	$[1.304, 1.752)$	$[1.752, 2.0]$
	0.08	0.085	0.085	0.115	0.13	0.155

The efficiencies for medium and tight cuts are shown in Table 3.10 [19]. Two values are shown, one that is obtained from a sample of electrons from Z$\rightarrow$ee decay and one obtained from an electron sample coming from W boson decay, W$\rightarrow$eν. A comparison to the value on simulated samples is also given. Efficiencies for loose electrons are not included, as the efficiency is near 100% and these criteria are very rarely used for physics analysis.

While the efficiencies in Table 3.10 are integrated over the range $|\eta| < 2.47$, excluding the region $1.37 < |\eta| < 1.52$, and the p_T range 20-50 GeV, binned efficiencies for medium electrons are shown in Figure 3.4. Medium electrons are the most common choice for physics analysis.

Table 3.10. Efficiencies for medium and tight electrons, integrated over η and p_T. The first error listed is statistical, while the second is systematic. The error on the efficiencies from Monte Carlo simulation is negligible.

Criteria	Sample	Data efficiency [%]	Simulation eff. [%]	Data/Simulation ratio
Medium	W→eν	$94.1 \pm 0.2 \pm 0.6$	96.9	$0.971 \pm 0.002 \pm 0.007$
	Z→ee	$94.7 \pm 0.4 \pm 1.5$	96.3	$0.984 \pm 0.004 \pm 0.015$
Tight	W→eν	$78.1 \pm 0.2 \pm 0.6$	77.5	$1.009 \pm 0.003 \pm 0.007$
	Z→ee	$80.7 \pm 0.5 \pm 1.5$	78.5	$1.028 \pm 0.006 \pm 0.016$

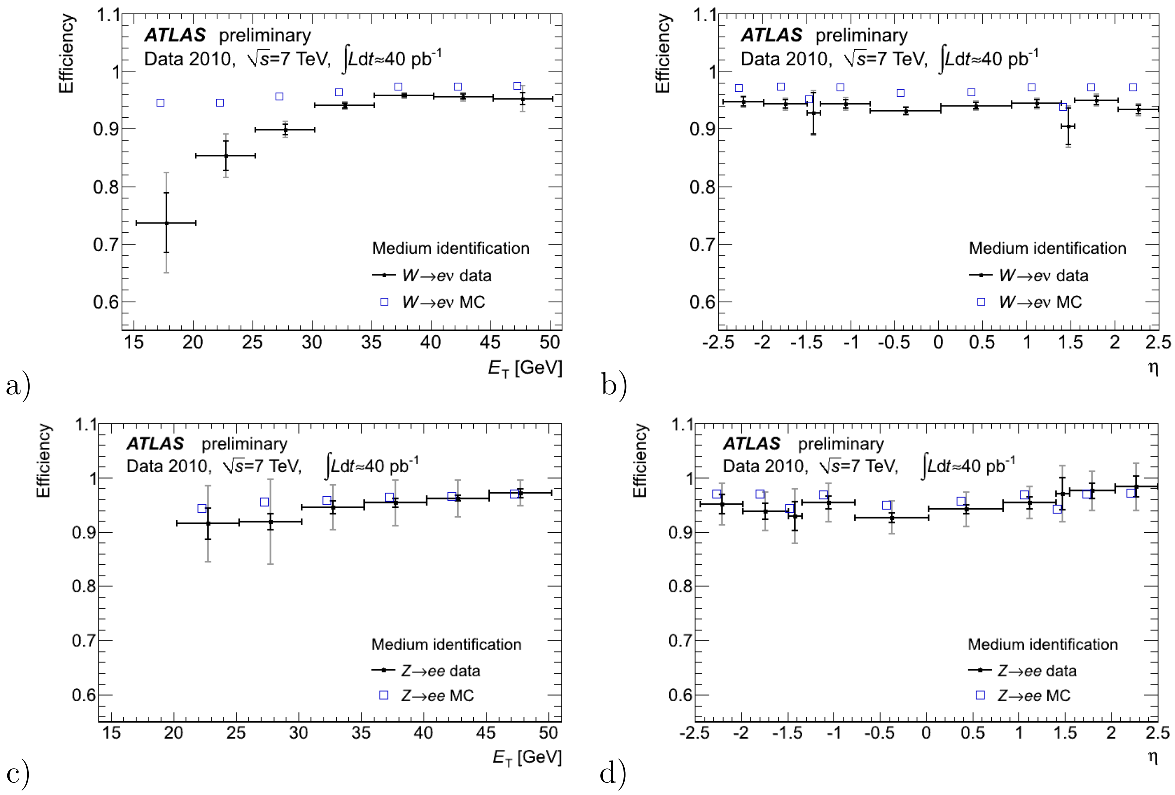

Figure 3.4. a) Medium electron efficiencies integrated over η and binned in electron p_T, and b) integrated in p_T and binned in electron η. Efficiencies are obtained using a sample of electrons from the W→eν process in data (black solid points with error bars) and simulation (blue open squares). c) Medium electron efficiencies integrated over η and binned in electron p_T, and d) integrated in p_T and binned in electron η. Efficiencies are obtained using a sample of electrons from the Z→ee process in data (black solid points with error bars) and simulation (blue open squares) [19].

3.4.4. Forward electrons

As alluded to in Section 3.3.1, the forward electron identification scheme uses various moments of the topo cluster, separately and in combination, to reject fakes from hadrons. The cut values are, as with standard electron identification, binned in η. However, for forward electrons only two η regions are used: the endcap in the forward region, corresponding to $2.5 < |\eta| < 3.2$ and the FCAL, corresponding to $3.2 < |\eta| < 4.9$ [7][6].

3.4.4.1. Forward loose

For the forward loose identification criteria, cuts on the values of the following cluster moments are used:

- The variance of λ, the distance of each cell from the cluster center (energy-weighted barycenter) along the shower axis. The shower axis is a straight-line extrapolation from the interaction point to the cluster center, shown in Figure 3.5. This parameter is required to be less than 6000 mm in the endcap and less than 7300 mm in the FCAL.

- The variance of R, the radial distance of each cell to the shower axis itself. This parameter is required to be less than 2600 mm in the endcap and less than 1000 mm in the FCAL.

- The difference between central cell's distance from calorimeter front along the shower axis, subtracted from the mean value for all cells in the cluster. This parameter is required to be less than 280 mm in both the endcap and the FCAL.

3.4.4.2. Forward tight

For the forward tight identification criteria, cuts on the values of the following cluster moments are used:

- All requirements from loose.

- Fraction of the cluster's total energy that is deposited in it's highest energy cell. This fraction is required to be greater than 39% in the endcap and 45% in the FCAL.

- The distance of each cell to the cluster center as measured along the longitudinal (ϕ) direction. This parameter is required to be less than 0.22 in the endcap and 0.3 in the FCAL.

- The distance of each cell to the barycenter between the first and second highest energy cells (cluster core) as measured along the lateral (η) direction. This parameter is required to be less than 0.57 in the endcap and 0.3 in the FCAL[2].

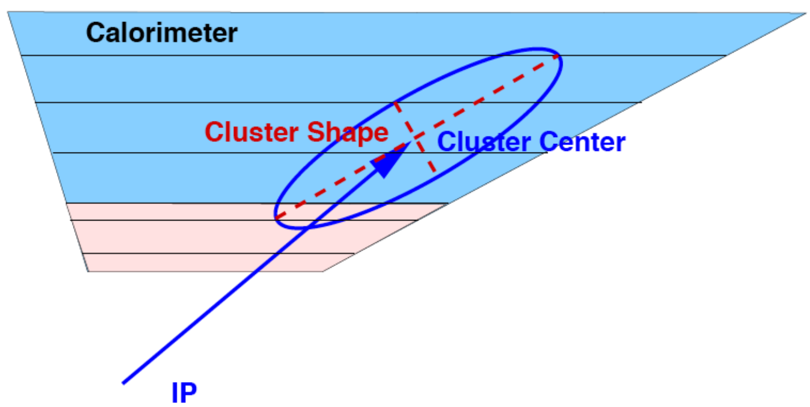

Figure 3.5. Illustration of topo cluster and shower axis [81].

Measurements made on 36 pb^{-1} data collected in 2010 found an identification efficiency for the forward loose cuts of approximately 85% and 55% for forward tight[3]. The result [55], along with comparison to Monte Carlo truth efficiency measurements, is shown in Table 3.11.

[2]The parameter η is unitless, see Equation 2.1.

[3]The method used to obtain efficiencies from the data is called tag-and-probe. It is discussed at length in Chapter 5, Section 5.5

Table 3.11. Forward electron identification criteria efficiencies, ϵ, for the endcaps (EMEC) and forward calorimeter (FCAL). Measurements from data are shown along with estimates from Monte Carlo truth information.

	$\epsilon_{MC} \pm stat$	$\epsilon_{data} \pm stat \pm syst$
EMEC-Loose	0.907 ± 0.001	$0.831 \pm 0.013 \pm 0.046$
FCAL-Loose	0.890 ± 0.001	$0.875 \pm 0.026 \pm 0.072$
EMEC-Tight	0.728 ± 0.001	$0.582 \pm 0.014 \pm 0.036$
FCAL-Tight	0.594 ± 0.002	$0.532 \pm 0.023 \pm 0.043$

3.5. Object quality requirements

In addition to the electron identification requirements, in analysis with electrons a requirement is placed on the quality of the electron. Here quality does not refer to ranking within the identification scheme, but rather to the quality of the electron's energy reconstruction. This requirement is necessary since non-operational parts of the calorimeter can lead to corruption in energy reconstruction.

3.5.1. Missing and problematic regions of the LAr calorimeter

In 2010 there were a number of non-operational Front End Boards (FEBs) in the LAr calorimeter, and consequently no energy was read out from the corresponding calorimeter cells. Though all such FEBs were fixed during the Winter 2010 shutdown, the problem has reemerged for six FEBs in 2011, albeit for a different reason. While the FEBs themselves are operational, there was a hardware failure on the crate controller board, leaving a 'hole' in the calorimeter in the region $0 < |\eta|1.4$ and $\phi = -0.65$ in the second and back layers [78].

This missing calorimeter information is problematic for correct electron reconstruction. The total cluster energy is the sum of the energies in all the cluster cells, across all calorimeter layers:

$$E_{clus} = \Sigma E_{cell}. \tag{3.1}$$

This cluster energy is smaller than the true[4] cluster energy if part of the cluster is in a region where there is no calorimeter information. In general the effect of the missing region on the accuracy of cluster energy reconstruction is directly proportional to the fraction of the cluster lying within the effected region. However, if enough of the energy deposit is within the effected region, this missing energy may cause the cluster to simply not be reconstructed at all.

3.5.2. Object quality criteria

If a cluster is reconstructed partially in an area of the detector that has no information, this leads to inaccurate energy reconstruction and it is not desirable to use the associated electron for analysis. Similar to the identification schemes discussed, an object quality set of criteria has been devised [28].

- If any part of the electron's cluster (any cell, in any layer) lies within a region effected by a dead high voltage module, the electron is rejected.
- If a cell in the cluster's core in any layer is in the region of a missing/non-operational FEB, the associated electron is rejected.
- If a cell in *any* part of the cluster in the first and second layers is in the region of a missing/non-operational FEB, the associated electron is rejected. Electrons

[4]The cluster's 'true' energy is that which would be reconstructed under perfect calorimeter conditions.

having clusters with a cell in a missing FEB in the back layer are still accepted, as the missing energy is accounted for in the calibration process [74].

Chapter 4

SEARCH FOR A NARROW DIELECTRON RESONANCE

The most exciting phrase to hear in science, the one that heralds new discoveries, is not 'Eureka!' but 'That's funny...'

Isaac Asimov (1920-1992)
American biochemist, Science-Fiction author

4.1. Introduction

This chapter outlines the search [23] for a narrow resonance at high mass decaying to two electrons, which can be interpreted as a Z', a heavy neutral gauge boson that was described in Chapter 1. No evidence for a Z' has been found; limits are set on it's possible cross section in the Sequential Standard Model (SSM) [62][93] and a Grand Unification model based on the E_6 group [53][46][38]. In the SSM the Z' has couplings to quarks and leptons equal to those of the Z boson of the Standard Model. The SSM is a 'toy' model, not really expected to be physical, but which serves as a benchmark for comparison between other scenarios. The Grand Unification model involves the breaking of the E_6 gauge group to $SU(5) \times U_\chi(1) \times U_\psi(1)$, where the simple gauge group $SU(5)$ contains the Standard Model gauge groups $SU(3) \times SU(2) \times U(1)$. The extra gauge groups $U_\chi(1)$ and $U_\psi(1)$ allow for the existence of extra Z bosons, where the observed $Z'(\theta)$ is a mix of the states Z_ψ and Z_χ belonging to the additional U(1) fields:

$$Z'(\theta) = Z'_\psi \cos(\theta) + Z'_\chi \sin(\theta), \tag{4.1}$$

Here the angle θ is the mixing angle that governs the value of the $Z'(\theta)$ particle's couplings to quarks and leptons.

The Z' mass and width are arbitrary in both the GUT model based on E_6 and in the SSM. In this analysis, a resonance with narrow natural width is searched for, with the width on the scale of the mass resolution of the ATLAS detector. In the case of a Z' decaying to electrons, this mass resolution is essentially dominated by the electromagnetic energy resolution of the LAr calorimeter, discussed in Section 2.2.2.1.

4.2. Data sample

The sample used is of pp collision data collected during the 2011 run of the LHC up until April 28 2011, for which the Good Runs List (GRL) provided by the ATLAS eγ performance group is passed. This GRL is a list of runs for which the parts of the detector necessary for electron and photon analyses were known to be in proper operating condition, including the inner detector, the LAr calorimeter, the solenoid, and the trigger used to select events. It also only includes those runs during which the LHC machine provided stable beams at the desired collision energy of 3.5 TeV per beam. The e20_medium trigger is used, which selects events for which there is at least one electron passing medium quality requirements and having $p_T > 20$ GeV. The integrated luminosity of this sample is 167 pb^{-1}.

4.3. Selection of dielectron pairs

The following requirements are imposed to select events for the analysis. Only one dielectron invariant mass pair per event is used. In addition to the GRL and trigger described, selected events are as follows:

- The event contains at least one primary vertex with at least 3 associated tracks.

- It contains two electrons reconstructed with the standard eγ reconstruction algorithm, described in Chapter 3, Section 3.1.

- Both electrons are central electrons, with "central" corresponding to a pseudorapidity region of $|\eta| < 2.47$, excluding the crack region between the barrel and endcaps of the LAr calorimeter ($1.37 < |\eta| < 1.52$). This crack region is excluded in most electron and photon analyses, as the reconstruction efficiency of electromagnetic objects is low here.

- Both electrons have transverse momentum greater than 25 GeV; this is calculated using energy information from the calorimeter, and directional information from the track, in the case of a track with four combined hits in the pixel and silicon detectors. In the case that the electron's track does not have the appropriate number of hits, directional information from the calorimeter is used. In this case, the position information is taken from all layers of the calorimeter for which the electron has deposited some amount of energy. As the trigger is at 20 GeV, electrons with $p_T > 25$ GeV are chosen so that the trigger efficiency is constant for each event. (See Figure 4.1.)

- Both electrons pass object quality requirements as outlined in Chapter 3, Section 3.5.

- Both electrons pass medium quality cuts, as outlined in Chapter 3, Section 3.4.

- Both electrons possess a hit in the first layer of the pixel detector of the tracking system, provided that the track is reconstructed in an area with fully functioning tracking modules and such a hit would be expected. This is required because frequently good quality electrons will generate such a hit, whereas fakes from pion decay will not.

- The event passes cleaning requirements to eliminate noise bursts in the LAr calorimeter. A noise burst [30] occurs when a large fraction (see Figure 4.2 for illustration) of the cells in the electromagnetic barrel or one of the endcaps has large readout energy (generally 5σ larger than the expected noise).

- Although a Z' would decay to an electron-positron pair, no requirement is placed on the charge of the electrons. This is due to the fact that at high p_T the efficiency to correctly identify an electron's charge begins to drop. Studies using Monte Carlo simulation (this study is shown in detail in Chapter 5, Section 5.5) have shown a noticeable drop in efficiency starting for objects with p_T >500 GeV. As electrons from the decay of a Z' of mass 1 TeV or larger will largely be in this p_T region, a requirement on charge is not used.

- Only events with $m_{ee} \geq 70$ GeV are accepted.

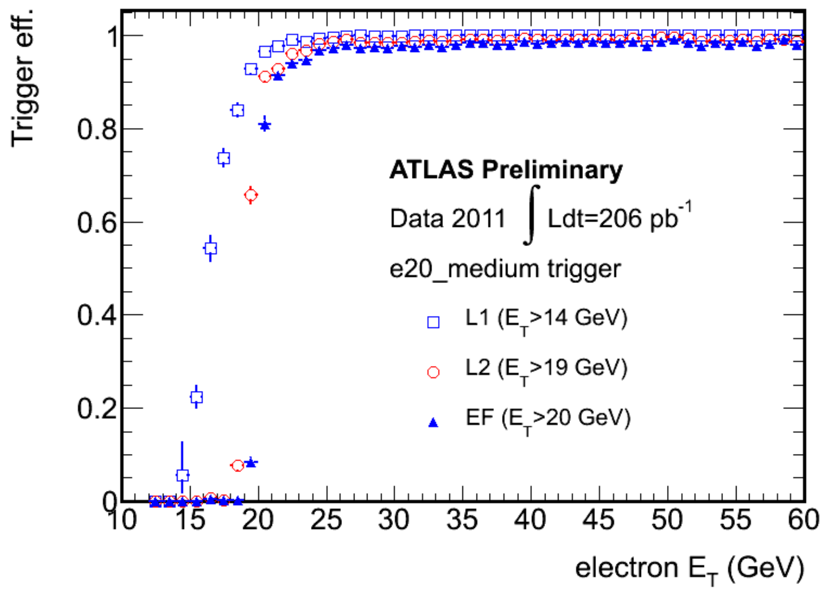

Figure 4.1. Trigger efficiency for the e20_medium trigger [18]. Note that the efficiency near 20 GeV is still increasing, and the efficiency does not plateau until approximately 25 GeV. The trigger efficiency was measured using a sample of electrons from Z→ee decay, using slightly more data than was used in this analysis. The decision to use electrons with p_T >25 GeV was based on a similar study using 2010 data.

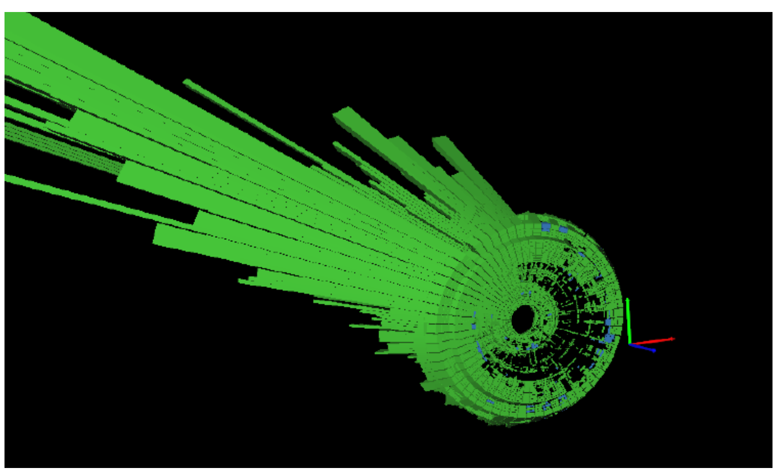

Figure 4.2. Event display of a noise burst in the LAr calorimeter [49].

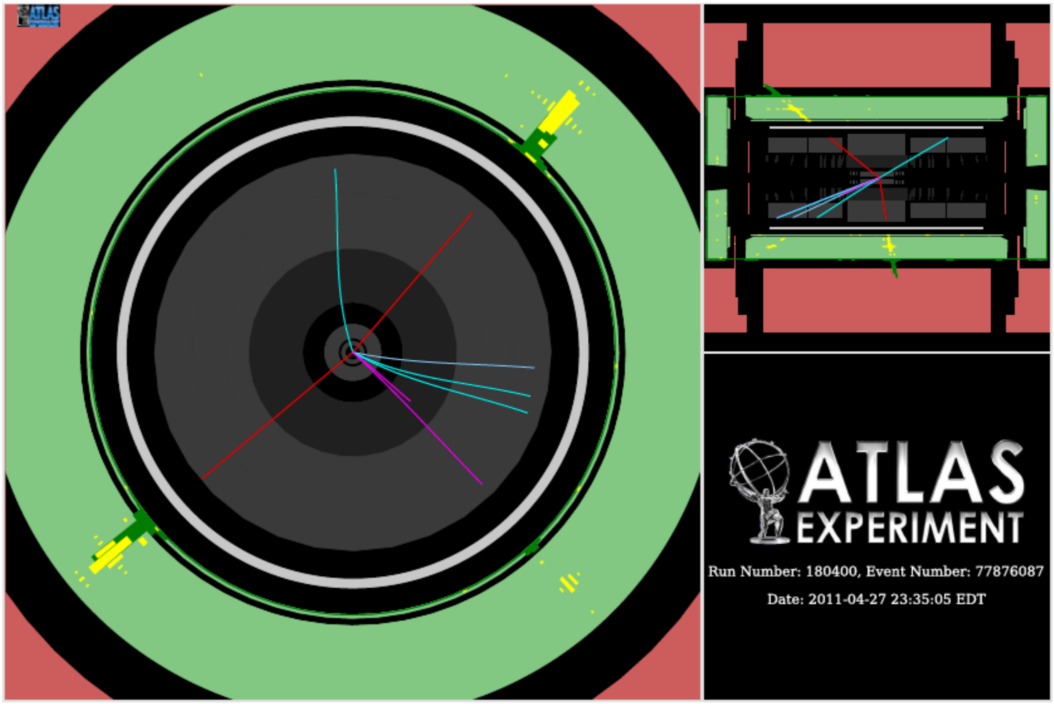

Figure 4.3. Event display of the event passing analysis selections with the highest dielectron invariant mass [23].

4.4. Background estimate

The backgrounds that have been considered are those from $t\bar{t}$ decay, $W \rightarrow e\nu + jets$, diboson decay (WW, WZ, ZZ), dijet events and the irreducible Drell-Yan process, $Z/\gamma* \rightarrow e^+e^-$. Of these, all have been estimated using Monte Carlo simulated samples on which the analysis selection has been imposed, and the result of which is normalized to the data luminosity. A special case is the dijet background. Due to the low incidence of jet-electron misidentification, the statistics of the Monte Carlo dijet samples are not high enough to adequately estimate this, especially for higher invariant mass values. Therefore, a procedure must be implemented to estimate this particular background from the data itself, see Section 4.4.2.[1]

Other possible sources of background that have not been described in detail in this analysis are those coming from prompt photons misidentified as electrons, and electrons from the decay of cosmic muons. Both backgrounds have been found to be negligible, via study on simulated samples [71]. To understand the contribution of photon backgrounds, I performed the analysis selections on simulated samples of prompt diphoton production and γ+jet production. Approximately five events are expected at 167 pb^{-1}, which is negligible. In the case of misidentified photons, the requirement that the electron's track have at least one hit in the first layer of the pixel detector (the 'b-layer') is especially helpful, as it has been determined by the author that this part of the tracking system is quite powerful for reducing electron-photon ambiguity (Appendix A of this document).

4.4.1. Backgrounds from Monte Carlo

To normalize the $t\bar{t}$, $W \rightarrow e\nu + jets$ and $DY \rightarrow e^+e^-$ backgrounds to each other, the highest-order available estimates of the different process' cross sections have been used. The background processes along with their associated generators and parton distribution functions (PDFs) are shown in Table 4.1. All samples are simulated using Geant4 [47] full-simulation [16] modeling of the detector. The order to which cross sections have been computed, programs used, corrections applied and uncertainty on the final cross section for each process are shown in Table 4.2. To normalize these backgrounds to the data, the number of events observed in the Z peak region ($70 \leq m_{ee} \leq 120$ GeV) is used.

[1]The first method described for estimating the dijet background was the main contribution of the author to this analysis. The analysis as a whole was performed by forty-one members of the ATLAS experiment, including the author.

Table 4.1. Summary of generators and PDF sets used for the Monte Carlo simulated background samples used in the Z' search.

Process	Generators	PDF
$t\bar{t}$	MC@NLO [79] 3.41,	CTEQ [51]
	Herwig [45][44]	
	JIMMY 4.31 [50]	
Diboson	Herwig 6.510	MRST2007 LO* [4]
$W \to e\nu + jets$	Alpgen [57],	CTEQ
	Herwig 6.510	
	JIMMY 4.31	
$DY \to e^+e^-$	Pythia 6.421[84],	MRST2007 LO*
	Photos [61] (final state radiation)	

Table 4.2. Summary of the order to which cross sections for backgrounds in the Z' search have been computed, along with program used for computation, corrections applied and uncertainty on cross section (derived from PDF uncertainty).

Process	Order	Program	Corrections	Uncertainty
$t\bar{t}$	NNLO	-	-	10% [82][91][56]
Diboson	NLO	-	-	5%
$W \to e\nu$	NLO	-	Rescaled to NNLO	30%
+ jets		-	$W \to e\nu + X$	
Drell-Yan	NNLO	PHOZPR [72]	QCD	3%
		HORACE [31][32]	and	-
		MSTW 2008 PDFs [3]	EW k-factors	4.5%

In the case of the exclusive $W \to e\nu + jets$ process, only a next-to-leading order (NLO) value of the cross section is calculated. However, the inclusive cross section for the process $W \to e\nu + X$ (also including the case of $W \to e\nu + nothing$) is known to next-to-next-to-leading order, and the NLO value is scaled to this.

Two separate correction factors, known as k-factors, have been defined. The QCD k-factor corresponds to a ratio between the cross section as calculated at leading order and next-to-next-to-leading order, while the electroweak k-factor takes into account higher order corrections due to virtual gauge boson loops in the diagram shown in Figure 4.4. These corrections are mass-dependent, as is described in Table 4.3. For the $DY \to e^+e^-$ sample, both k-factors have been used to scale the cross section.

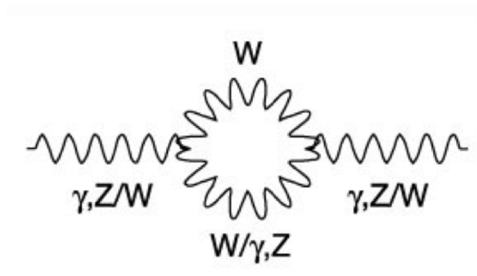

Figure 4.4. Feynman diagram depicting higher-order corrections to the propagation of γ, Z or W gauge bosons. In the case of the γ and Z, the loop consists of two W bosons [63].

Table 4.3. Mass-dependent electroweak and QCD k-factors applied to the DY background sample.

Electroweak	
Mass bin	k-Factor
[70,110] GeV	-
(110,250] GeV	$0.841 + 0.00258m_{ee} - .0000108m_{ee}^2 + .0000000154m_{ee}^3$
(250,1750] GeV	$1.067 - .0000634m_{ee}$
m_{ee} >1.75 TeV	$0.873 + 0.000183m_{ee} - .0000000797m_{ee}^2$
QCD	
Mass bin	k-Factor
[70,172] GeV	1.1555
m_{ee} >172 GeV	$1.16260 - .0000311495m_{ee} - .0000000575063m_{ee}^2$

4.4.2. Dijet background estimated from data

Two methods have been used to estimate the amount of dijet contamination in the dielectron sample used for the analysis. These are called the 'reverse ID' method, which relies on selecting a sample of electrons that pass a looser quality selection and then fail aspects of the final selection, and the 'isolation template' method, which uses isolation profiles of signal and background processes. Here isolation refers to the amount of energy, not belonging to the electron itself, found in a cone surrounding the electron's cluster. The isolation requirement is discussed in more detail in Section 4.4.2.2.

4.4.2.1. Reverse ID method

This method begins with selection of two samples of events, one set passing the 2g20_loose trigger (sample A), which is used to estimate the background at invariant masses less than 200 GeV, and one passing the e60_loose trigger (sample B), which is used to estimate the background at higher invariant mass. The first trigger is selected because it is the lowest-p_T threshold, un-prescaled trigger imposing loose cuts on two electrons, and the second because it is the lowest-p_T un-prescaled trigger with loose cuts on only one electron.

Sample A requirements

- Event passes primary vertex and noise burst cleaning requirements of the main analysis.

- Event passes the 2g20_loose trigger. This requires two clusters in the electromagnetic calorimeter, each having $p_T > 20$ GeV, and passing the loose requirements for photons at the trigger level. These requirements are equivalent to those at the cluster level for loose electrons, described in Chapter 3, Section 3.4.

- Two electrons reconstructed with the standard eγ algorithm are used, which pass the loose requirements (including track-cluster matching, not implemented in the trigger selection), are within the η region used for the analysis, pass object quality requirements and have at least one hit in the first layer of the pixel detector if one is expected. As in the standard analysis, since the trigger is at 20 GeV, electrons with $p_T > 25$ GeV are chosen.

- Both electrons explicitly *fail* the medium electron selection.

The difference between the medium and loose selections is that medium requires more strict track quality and uses the finely-segmented strip layer of the LAr calorimeter to reject wider showers. In effect, this means that electrons passing loose requirements but failing medium are more likely to be jets that mimic electrons to some extent. Thus, sample A's distribution can be considered to be background-like for the dielectron analysis. However, because both electrons are required to pass the loose requirement, the events of sample A do not extend to the 1 TeV range, and the background template extracted in this way does not give information about the shape of the dijet background at high invariant mass. For this reason, a separate sample has been constructed.

Sample B requirements

- Event passes primary vertex and noise burst cleaning requirements of the main analysis.

- Event passes the e60_loose trigger. This requires at least one electron with $p_T > 60$ GeV, and passing the loose requirements for electrons at the trigger level. These requirements are equivalent to those at for loose offline electrons, described in Chapter 3, Section 3.4. A track-cluster matching requirement is imposed on the electrons at the trigger level, which leads to a loss of efficiency of about 1%.

- Two electrons reconstructed with the standard eγ algorithm are used. Only one is required to pass the loose requirements, but both are within the η region used for the analysis, pass object quality requirements and have at least one hit in the first layer of the pixel detector if one is expected. As the trigger is at 60 GeV, the leading p_T electron is required to have $p_T > 60$ GeV, whereas the second electron is required to have $p_T > 25$ GeV as in the main analysis.

- Both electrons explicitly *fail* the medium electron selection. The subleading container level electron specifically fails at least one of the cuts on the cluster variables in the strips layer. This means that the object may either pass or fail cuts on the cluster variables in the middle layer, and may either pass or fail the medium electron tracking cuts.

Samples A and B are normalized to each other using the number of events in each sample in the mass window 200-300 GeV, for which there are sufficient events in each sample. The normalized distribution is shown in Figure 4.5.

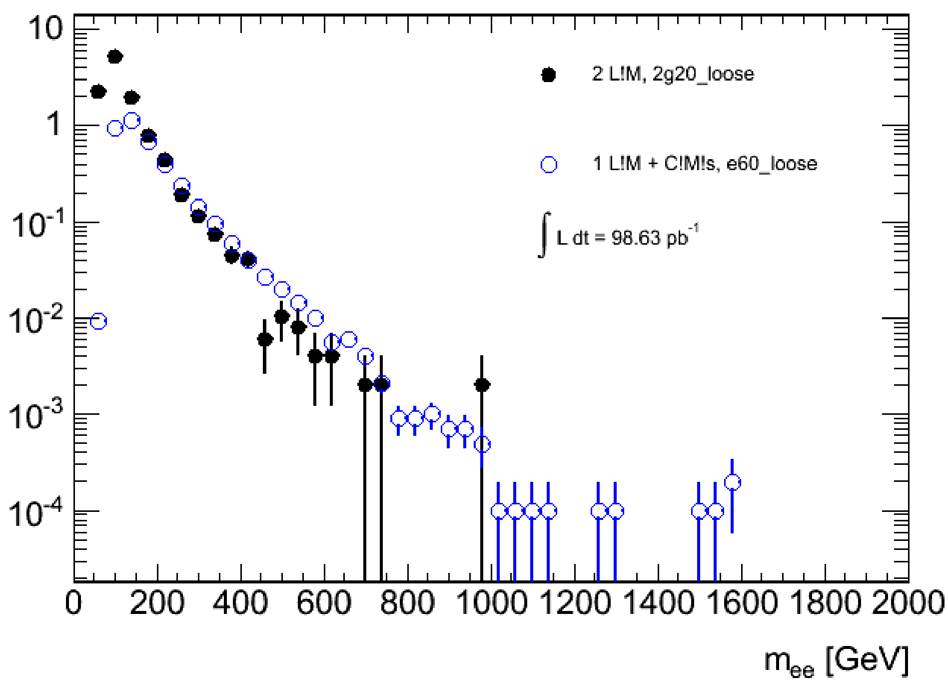

Figure 4.5. Final dijet background templates used for the analysis. The black dots show the template derived from sample A. The blue open circles show the template derived from sample B, where the leading electron passes loose cuts and fails medium. The subleading electron is container level, failing medium explicitly due to failing at least one of the cuts on the electron cluster in the strip layer. This means that the container level electron may either pass or fail all the other medium requirements, including cuts on the cluster shape and energy density in the middle layer (in common with loose cuts) and the tracking cuts. Note that the sample B derived template extends to a much higher invariant mass region than does the sample A template.

Using a sum of the final result shown in Figure 4.5 and the Monte Carlo simulated backgrounds described in Section 4.4.1, a fit is made to the data in order to extract the correct normalization of the template. Systematic uncertainty on the number of dijet events estimated in this way is taken from the differences in shape by using variations on the template, as shown in Figure 4.5.

4.4.2.2. Isolation template method

This method uses a measure of the electrons' isolation, which in this case is defined as the amount of energy deposited in the calorimeter *not* belonging to the electron's cluster, within a cone $\Delta R < 0.2$ around the electron's cluster, where

$$\Delta R = \sqrt{(\eta_{el} - \eta_c)^2 + (\phi_{el} - \phi_c)^2}. \tag{4.2}$$

Here, $\eta_{el}(\phi_{el})$ signifies the $\eta(\phi)$ position of the electron's cluster center and $\eta_c(\phi_c)$ the $\eta(\phi)$ position of the calorimeter cell for which the distance ΔR should be calculated.

The isolation distribution of the electrons passing the analysis criteria are compared to those of prompt electrons, which are those produced at the interaction point and are considered to be 'signal-like', and dijet events. Both these comparison distributions are taken from the data itself. In the case of the prompt electrons this is accomplished by identifying a sample from W boson decays. To obtain a pure sample, tight electrons are used along with requiring at least 35 GeV missing transverse energy in the event, and only candidates with transverse mass greater than 40 GeV are accepted. The strict cut on the amount of missing transverse energy required effectively reduces the background from jets. The background-like isolation template is obtained by reconstructing events that explicitly fail the electron identification criteria as detailed in the reverse ID method description. It is expected that the isolation distribution for true electrons coming from the decay of an electroweak boson is narrow, peaking near 0 GeV, with the width coming from energy leakages from the electron's cluster into the surrounding regions, and energy from the underlying event or pileup. In contrast, for jet events and electrons from the decay of hadrons, the isolation distribution is wide and peaks at a larger value, near 10 GeV.

Fits are made to the data isolation distribution using a combined function incorporating the signal-like isolation template and the background like one. The fraction of signal and background estimated by this method is returned by the fit.

4.4.2.3. Combined dijet background estimate

The results of Sections 4.4.2.1 and 4.4.2.2 are combined to yield the final dijet background estimate used in the analysis. This is accomplished by plotting both estimates together and generating a best-line fit to a power law function in dielectron invariant mass, with two parameters: the exponent and total number of events with dielectron mass greater than 110 GeV. Both background estimates along with the fit are shown in Figure 4.6.

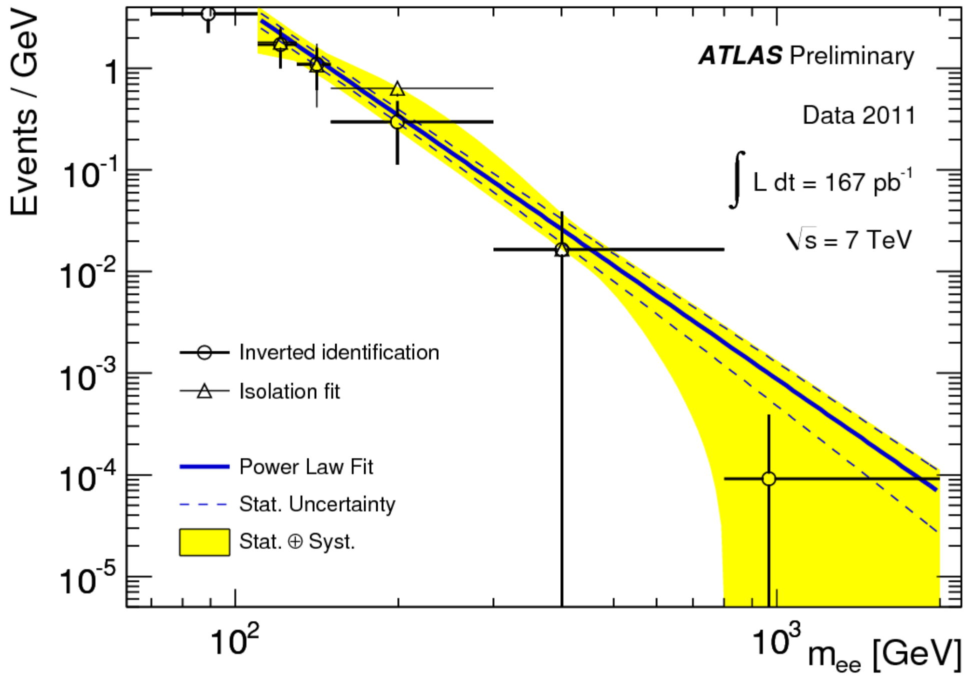

Figure 4.6. Background estimates obtained via the reverse ID and isolation template methods, along with the best-line power law fit. The integral of the fit function in each invariant mass bin is ultimately used to obtain the estimated number of dijet events per bin. Here, the open circles show the background estimate obtained using the reverse ID method described in Section 4.4.2.1 and the open triangles show the estimate obtained with the isolation fits method of Section 4.4.2.2.

4.5. Signal Monte Carlo samples

As the Z' of the SSM is the benchmark for the analysis, the signal sample was generated in Pythia 6.421 [84] using SM couplings to quarks and leptons and MRST2007 [4] LO* PDFs. Final state radiation is handled using PHOTOS [61]. The same QCD k-factor as was used for the Drell-Yan background sample is applied to the Z' sample, but recalculated for the appropriate mass. The electroweak k-factor is not applied, as the coupling of the Z' of the SSM to W and Z bosons is not specified. Z' samples with masses of 1, 1.25 and 1.5 TeV are used for plots. For limits, a special sample was generated and is described in Section 4.8.

4.6. Number of observed and expected events

Shown in Table 4.4 is the total number of events that were observed in the data using the analysis described in Sections 4.2 through 4.4, along with the expected amount of background, in each invariant mass bin. The uncertainties correspond to combined statistical and systematic uncertainties, discussed in Section 4.7. Central values or uncertainties listed as '0' correspond to values of less than 0.05. Fractional values occur for background estimates. In the case of the dijet background, this may happen as the number of events is taken from the integral of the function shown in Figure 4.6. In the case of the remaining backgrounds, this is due to the fact that the number of events surviving analysis selections is then normalized using the cross sections in Table 4.2.

Table 4.4. Summary of number of observed and expected events. Fractions of events are due to normalization.

Mass m_{ee} [GeV]	70-110	110-130	130-150	150-170	170-200
Drell Yan	41774.5 ± 34.4	530.4 ± 16.4	186.9 ± 6.2	100.2 ± 3.6	78.7 ± 3.0
$t\bar{t}$	32.5 ± 3.3	16.1 ± 1.7	11.1 ± 1.2	8.2 ± 0.8	7.9 ± 0.8
Diboson	58.5 ± 3.3	4.7 ± 0.5	3.6 ± 0.4	3.0 ± 0.4	2.4 ± 0.3
$W \rightarrow e\nu + jets$	23.3 ± 6.5	11.8 ± 3.3	6.1 ± 1.7	7.2 ± 2.1	6.8 ± 2.0
Dijet	166.3 ± 61.1	41.1 ± 21.1	26.5 ± 10.1	16.0 ± 7.7	16.6 ± 5.7
Total BG	42055.0 ± 70.6	604.1 ± 27.0	234.1 ± 12.0	134.6 ± 8.8	112.4 ± 6.8
Data	42055	576	231	116	110
Mass m_{ee} [GeV]	200-240	240-300	300-400	400-800	800-2000
Drell Yan	46.4 ± 1.9	31.6 ± 1.2	16.6 ± 0.7	8.6 ± 0.5	0.4 ± 0.0
$t\bar{t}$	6.1 ± 0.6	4.5 ± 0.4	2.5 ± 0.2	0.8 ± 0.1	0.0 ± 0.0
Diboson	2.2 ± 0.3	1.6 ± 0.3	1.2 ± 0.2	0.4 ± 0.1	0.1 ± 0.1
$W \rightarrow e\nu + jets$	3.8 ± 1.1	1.6 ± 0.5	1.1 ± 0.3	0.9 ± 0.3	0.1 ± 0.0
Dijet	9.9 ± 8.8	7.0 ± 6.8	4.6 ± 3.2	3.3 ± 1.8	0.5 ± 0.5
Total BG	68.5 ± 9.1	46.3 ± 7.0	26.1 ± 3.3	13.9 ± 1.9	1.1 ± 0.5
Data	59	48	22	8	1

Combined expected signal and background plots for the dielectron invariant mass is shown in Figure 4.7. The background expectation and the number of observed events for several other single and dielectron observables are shown in Figures 4.8 and 4.9.

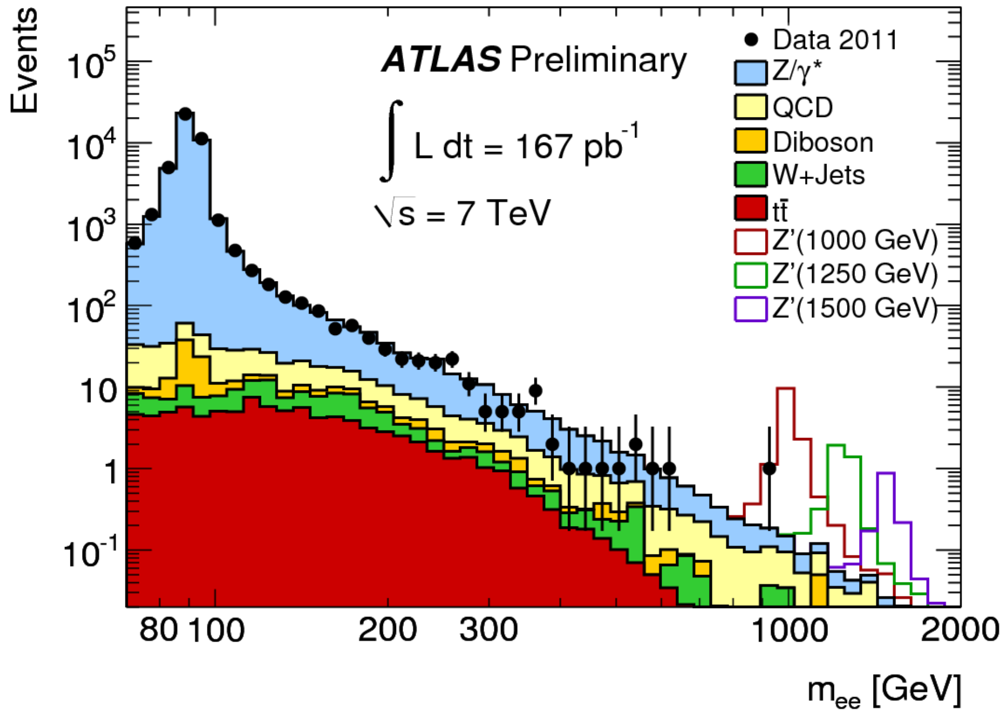

Figure 4.7. Dielectron invariant mass. This reflects the numbers given in Table 4.4. The number of events observed in the data is shown by the black points, while the various background estimates described are separated according to the legend. Here the label 'QCD' refers to the dijet background estimate. At the right hand side of the plot, three Z' signal samples have been included, normalized to the data luminosity, to indicate what a signal would look like. The masses used are 1 TeV (red line), 1.25 TeV (green line) and 1.5 TeV (violet line). The significance of the single event near 950 GeV is discussed in Section 4.8.2. [23]

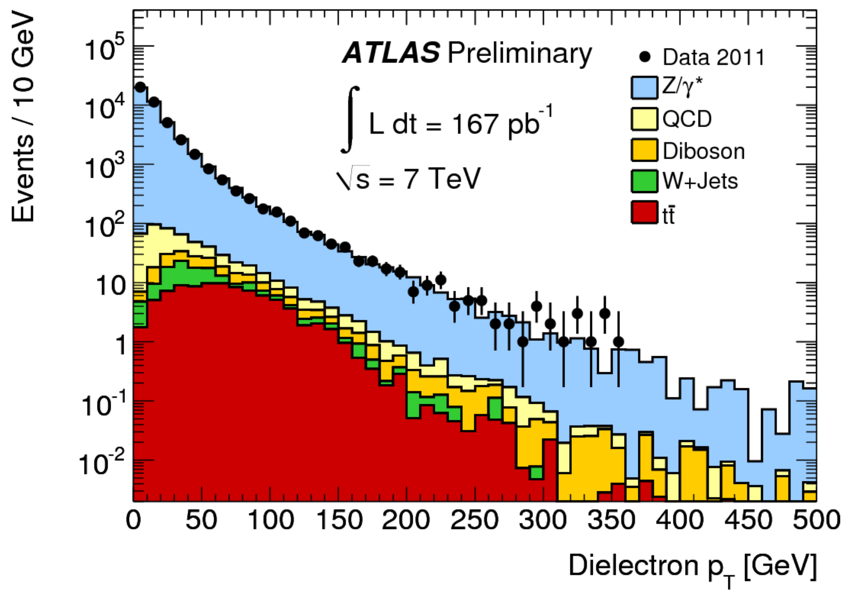

a)

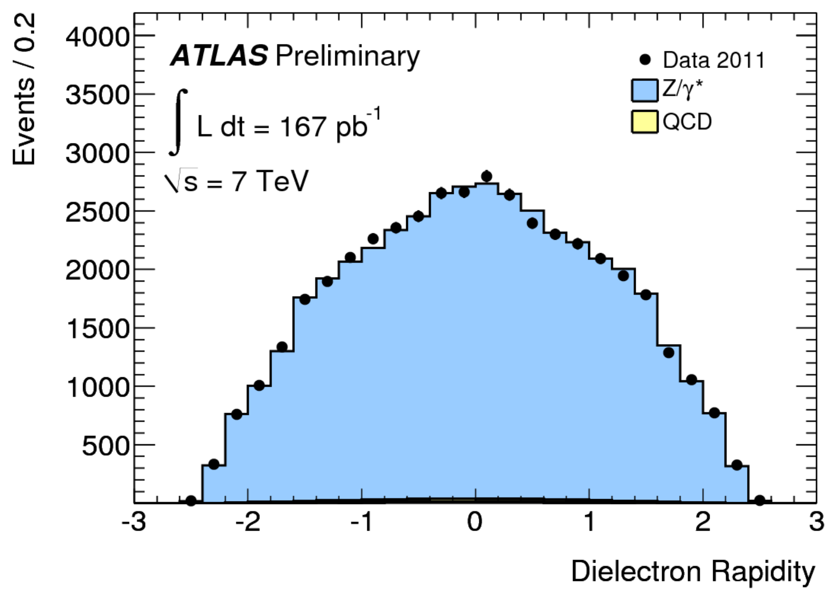

b)

Figure 4.8. (a) Dielectron p_T and (b) dielectron rapidity, $y = \frac{1}{2}\ln\left(\frac{E+p_z}{E-p_z}\right)$. The observed events in data are shown by the black points. The p_T distribution is in logarithmic scale to clearly show the high p_T tail of the distribution, and because of this all backgrounds are included in the plot. In the case of the rapidity distribution, only the dijet (QCD) background is shown. Since the plot is in linear scale, the other backgrounds would not be visible if included. (Note that the dijet background is also not large enough, integrated over all invariant mass bins, to be visible.) [23]

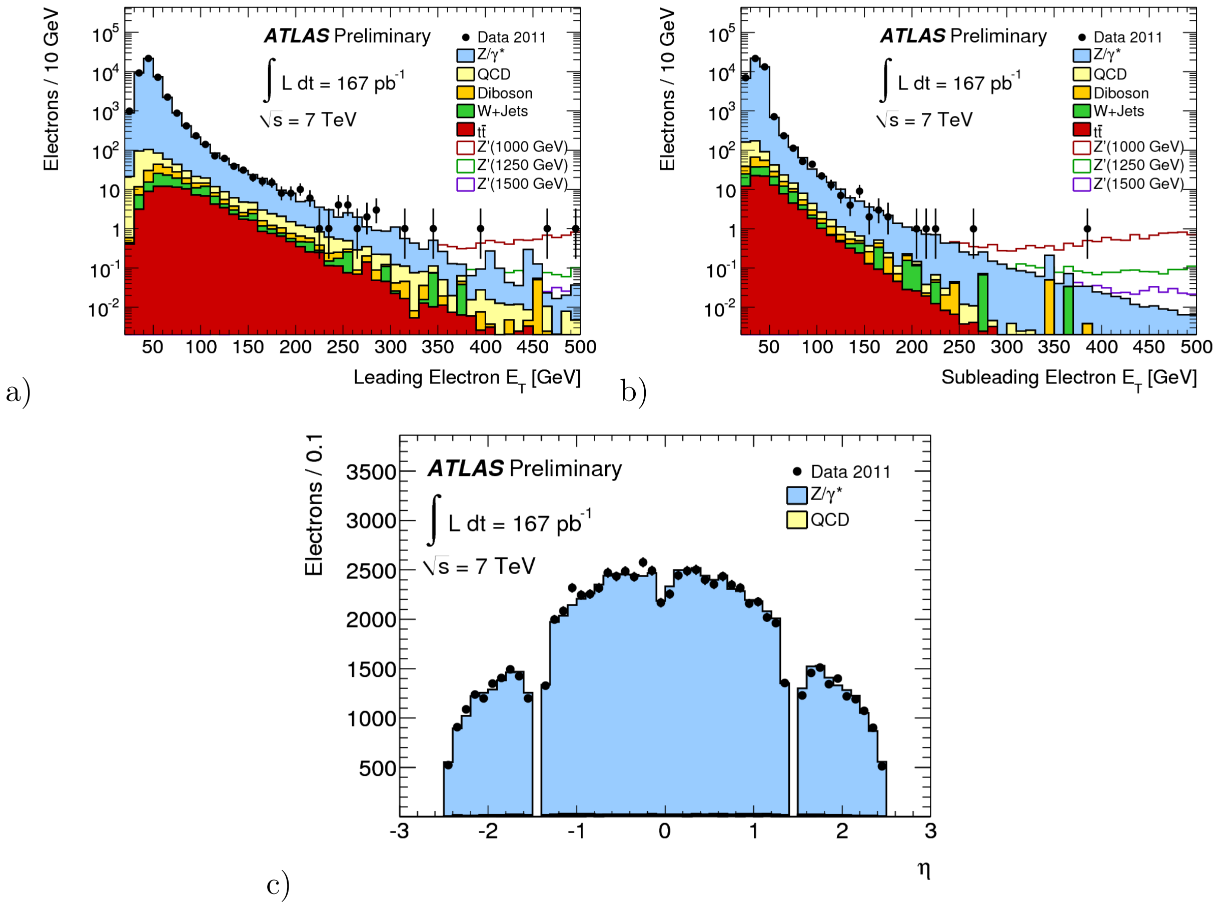

Figure 4.9. (a) Leading electron p_T, (b) subleading electron p_T and (c) η for both electrons. In the case of the p_T distributions (a) and (b), as in Figure 4.8a, logarithmic scale is used in order to show the tails at high p_T, and consequently all backgrounds are shown. Here, the same three signal Z' samples shown in Figure 4.7 are also included. In the η distribution shown in (c), as in Figure 4.8b, the plot is in linear scale, and as such it does not make sense to include all backgrounds. [23]

4.7. Systematic uncertainties

Systematic effects on the measurement are as follows:

- Uncertainty on electromagnetic energy resolution (variation in this parameter produces a fluctuation in the width of a reconstructed resonance). At high values of electron p_T, the actual resolution itself is dominated by a constant term (Equation 2.2) having value $(1.1 \pm 0.2)\%$ in the barrel and $(1.8 \pm 0.4)\%$ in the endcaps. The systematic uncertainty on these values has negligible effect on the final results.

- Uncertainty on the electromagnetic energy scale (variation in this parameter produces a shift in the mean position of a reconstructed resonance). The exact value of the uncertainty depends on the electron's location in η and it's p_T, with possible values ranging from 0.5% to 1.5%. The effect of this on the final exclusion limit is negligible, as a change in energy scale does not produce a change in the actual shape of the signal or the background.

- Efficiency of reconstruction and identification of electrons at high p_T has been found to be stable, so there are no systematic uncertainties corresponding to these efficiencies that affect the analysis.

- Uncertainty of 5% on the Z/γ^* cross section [24].

- Uncertainty on k-factors [24]. The QCD k-factor applied to both the signal samples and the Drell-Yan background has an uncertainty of 4% for both. The weak k-factor, applied to the Drell-Yan background only, has an uncertainty of 5.5%.

- Uncertainty on the PDFs used in the simulated samples, both signal and background, corresponds to 7.5% [3].

- The dijet background estimate from data carries a systematic uncertainty of 35% [23].

In total, the expected number of signal events has a 10% systematic uncertainty, while the amount of expected background has 36% uncertainty due to systematic effects.

4.8. Extraction of limits on the Z' cross section

This section details the statistical method used to determine whether or not there is evidence for a Z' signal in the observed data spectrum, and the procedure for setting limits in the case of no discovery.

4.8.1. Testing for discovery using p-value

A signal is searched for in the mass range $m_{ee} > 110$ GeV, using a Bayesian approach to hypothesis testing [2]. Here, a p-value is defined, which gives the probability of the observed data given the parameters of the model being tested. The calculation of the p-value begins with the likelihood function for a given model, M, and specific data set, $\vec{D}$:

$$L(\vec{\lambda}, \vec{\nu}|\vec{D}, M) = \frac{P(\vec{D}|\vec{\lambda}, \vec{\nu}, M)P_0(\vec{\lambda}, \vec{\nu}|M)}{\int P(\vec{D}|\vec{\lambda}, \vec{\nu}, M)P_0(\vec{\lambda}, \vec{\nu}|M)d\vec{\lambda}d\vec{\nu}}. \tag{4.3}$$

Here, $\vec{\lambda}$ and $\vec{\nu}$ are the parameters of the model, M, where the $\vec{\lambda}$ are the parameters of interest (for example, in this case the dielectron invariant mass distribution is the parameter being analyzed) and the $\vec{\nu}$ are nuisance parameters, meaning they are not included explicitly in M, but can effect the final result (these are often detector related parameters, such as energy resolution).

The function $P_0(\vec{\lambda}, \vec{\nu}|M)$ is referred to as the 'prior', and reflects assumptions about the parameters $\vec{\lambda}$ and $\vec{\nu}$ that are made before data from the experiment are considered. Also, the denominator of Equation 4.3 can be written simply as $P(\vec{D})$, the probability of observing the data.

In this analysis, the binned likelihood function is given by [69]:

$$
\begin{aligned}
L(\vec{D}|\sigma_{obs},\nu_i) = \prod_{k=1}^{bin} \frac{\mu_k^{n_k} e^{-\mu_k}}{n_k!} \prod_{i=1}^{sys} G(\nu_i, 0, 1), \\
\text{where} \ \ \mu_k = \sum_j (\sigma_{obs})_j T_{jk}(1+\nu_i\epsilon_{jik}).
\end{aligned}
\tag{4.4}
$$

The parameters used in Equation 4.4 are as follows:

- μ_k is the expected number of events in mass bin k, which is the Poisson mean of the expected signal and background events, with n_k the number of observed events in mass bin k.

- T_{jk} are the templates corresponding to the shape of the distribution, in the case of signal (j=1) and background (j=2), binned in invariant mass bins k. The templates carry no information about the expected number of events, and describe only the shape of the distribution. These templates are taken from a special simulated sample that is generated such that the differential cross section with respect to dielectron invariant mass is flat (i.e., the sample is not generated for a Z' particle with any preferred mass). This sample can be reweighted to consider a Z' of any mass and width.

- The ν_i are various systematic uncertainties; when considered in each mass bin this is expressed as $\nu_i\epsilon_{jik}$. They are assumed to follow a Gaussian distribution, G, with mean at 0 and variance equal to 1.

- σ_{obs} is the observed cross section of the signal process, returned by the fit of the likelihood function. Here, the cross section observed is $\sigma_{obs} = \sigma_{Z'} Br_{ee} L A_{ee}$, where $\sigma_{Z'}$ is the Z' cross section, Br_{ee} is the branching ratio for decay to dielectrons, L is the integrated luminosity of the data set and A_{ee} is the acceptance of the dielectron channel.

The likelihood function given by Equation 4.4 can be marginalized, meaning the number of parameters is reduced, by integrating the prior over all possible values of one of the parameters:

$$L(\vec{D}|\sigma_{obs}) = \int L(\sigma_{obs}, \nu_1, \nu_2 \cdots \nu_N) d\sigma_1 d\sigma_2 \cdots d\sigma_N. \tag{4.5}$$

Markov Chain Monte Carlo technique, a method of random number selection, is used to evaluate this integral.

The marginalized likelihood of Equation 4.5 can be used to obtain the p-value. For ease of notation, I introduce functions, f, that stand for likelihoods:

$$\begin{aligned} f^*(\vec{x}) &= L(\vec{x}|\sigma_{obs}), \\ f^D &= L(\vec{D}|\sigma_{obs}). \end{aligned} \tag{4.6}$$

Note that these are simply the marginalized likelihood of Equation 4.5, but in the case of $f^*(\vec{x})$, for a non-specified data set $\vec{x}$ as opposed to the observed data, $\vec{D}$. Then, the p-value is given by:

$$p - value = \frac{\int_{f^*(\vec{x}) < f^D} f^*(\vec{x})\ d\vec{x}}{\int f^*(\vec{x})\ d\vec{x}}. \tag{4.7}$$

.

The data set $\vec{x}$ is supplied by simulated data generated according to the hypothesis that one wants to test (for example, a background only hypothesis). Figure 4.10 illustrates how the ratio of Equation 4.7 can lead to a value close to 1 (good agreement between the data and the model represented by the simulated data set) or a small value (poor agreement).

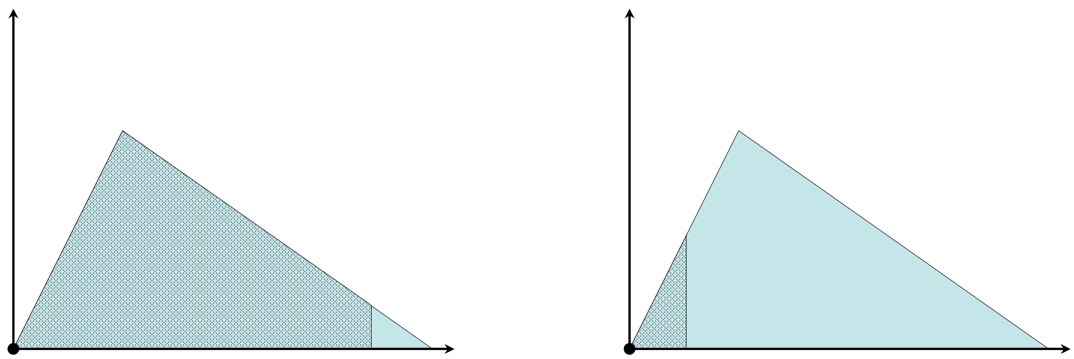

a) b)

Figure 4.10. The light area represents the total integral $\int f^*(\vec{x})d\vec{x}$, while the hatched area represents the integral $\int_{f^*(\vec{x})<f^D} f^*(\vec{x})d\vec{x}$. In a) the p-value is close to one, signifying good agreement between the data and the model being tested. In b) the p-value is small, signifying poor agreement. In the case that the Standard Model is the model being tested, a small p-value such as represented by b) could be evidence for new physics.

Given a background-only hypothesis for the simulated data $\vec{x}$, and the observed data as described in this chapter, the p-value, is 94%. This means that there is a 94% chance for the observed dielectron distribution to occur in the absence of a signal, and therefore no evidence for a Z' is seen. For evidence of a signal, a p-value of 0.135% is required (corresponding to 3σ significance) and for discovery a p-value of 0.0000287% is required (corresponding to 5σ significance). As no significant excess of events beyond the background expectation was observed, limits are set on the cross section of a Z' in the two models introduced earlier.

4.8.2. Limit setting

Since there is no evidence for a Z' in the data set observed, limits at the 95% confidence level are set. As in the case with the discovery statistic (p-value), for limit setting a Bayesian approach is used.

The first step is conversion of the marginalized likelihood of Equation 4.5 into a posterior probability distribution. This probability summarizes one's knowledge after performing the experiment, and it relies on information from the 'prior' discussed earlier, which contains information on the model known before the experiment is done. The posterior probability is given by:

$$P(\vec{\lambda}, \vec{\nu}, M|\vec{D}) = \frac{L(\vec{D}|\vec{\lambda}, \vec{\nu}, M)P_0(\vec{\lambda}, \vec{\nu}, M)}{\sum_M \int L(\vec{D}|\vec{\lambda}, \vec{\nu}, M)P_0(\vec{\lambda}\vec{\nu}, M)\ d\vec{\lambda}d\vec{\nu}}. \tag{4.8}$$

In this analysis a prior flat in $\sigma_{Z'}$ is used, $\pi(\sigma_{Z'}) = 1$. To obtain the 95% confidence limit, the posterior probability density specific to this analysis is used:

$$0.95 = \frac{\int_0^{(\sigma_{Z'})_{95}} L(\vec{D}|\sigma_{Z'})\pi(\sigma_{Z'})\ d\sigma_{Z'}}{\int_0^{\inf} L(\vec{D}|\sigma_{Z'}\pi(\sigma_{Z'})\ d\sigma_{Z'}}, \tag{4.9}$$

where $(\sigma_{Z'})_{95}$ is the 95% Bayesian upper limit on the Z' cross section. The limits obtained in this way, on the Z' cross section multiplied by dielectron branching ratio, are shown in Figure 4.11.

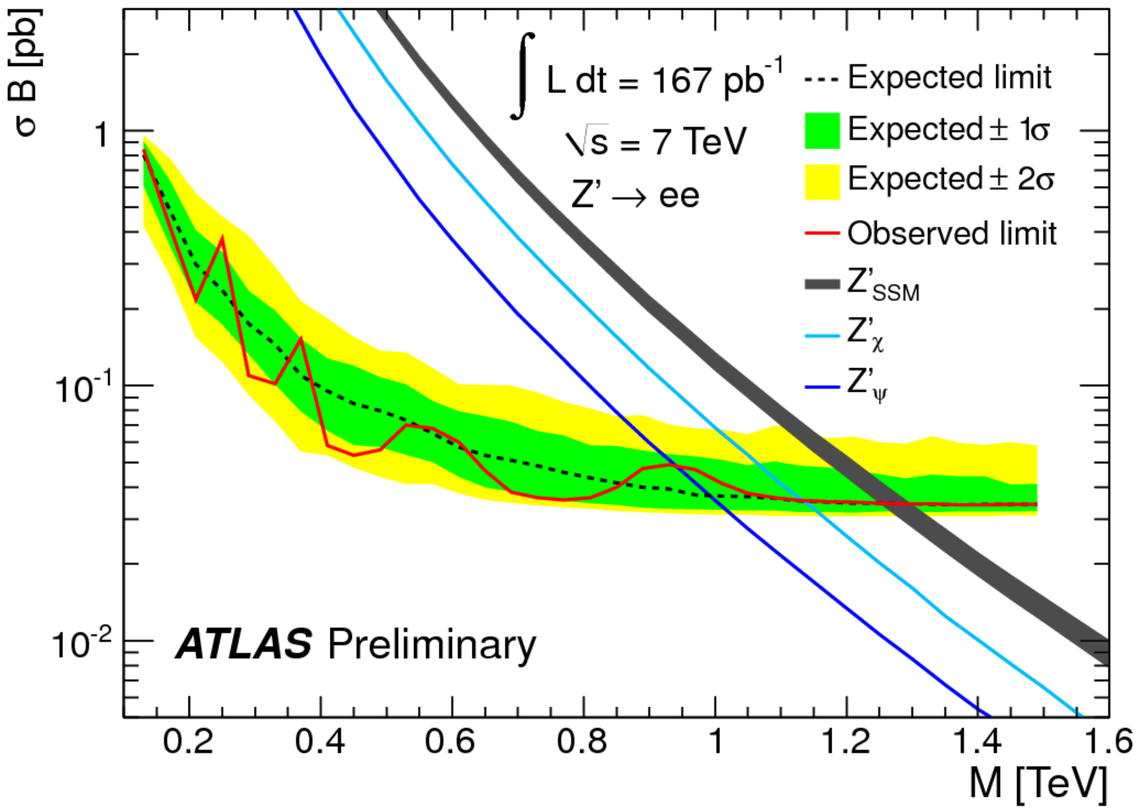

Figure 4.11. Limits set on the Z' cross section multiplied by dielectron branching ratio. The expected limit is shown by the black dashed line, with the observed limit given by the red line. $\pm1\sigma$ and $\pm2\sigma$ deviations from the expected limit are shown by the green and yellow bands, respectively. Fluctuations of the red line above the black dashed one represent an excess of events above the background expectation; in no case is there a deviation outside of 2σ in this respect. The single event observed near 950 GeV causes the limit to fluctuate within 1σ of the expected value. Limits on $\sigma_{Z'} \times Br(ee)$ have also been interpreted as Z' mass limits in the context of the SSM model and for two Z' particles from an E6 model (Z'_χ and Z'_ψ). This is indicated by the blue and dark grey bands. The points where these bands meet the red line, projected onto the invariant mass (x) axis indicates the mass limit. The thickness of the bands indicates the theoretical uncertainty on the model. [23]

Chapter 5

MEASUREMENT OF LEPTON FORWARD-BACKWARD ASYMMETRY IN e^+e^- PAIRS

In physics, your solution should convince a reasonable person. In math, you have to convince a person who's trying to make trouble. Ultimately, in physics, you're hoping to convince Nature. And I've found Nature to be pretty reasonable.

Frank Wilczek (1951-present)
American physicist, Nobel laureate

This chapter details the measurement of forward-backward charge asymmetry (A_{FB}) using e^+e^- pairs observed in collision data from the LHC with the ATLAS detector. The observed distribution of A_{FB} vs mass is checked against the Standard Model expectation using a simulated sample of the Drell-Yan process. In this way, the A_{FB} spectrum is used to search for new physics in the form of a Z'.

5.1. Measurement of A_{FB} at a pp collider

Recall from Chapter 1 that the asymmetry, A_{FB} is given by

$$A_{FB} = \frac{N_F - N_B}{N_F + N_B}, \tag{5.1}$$

where N_F is the number of invariant mass pairs having $\cos\theta^* > 1$ and N_B is the number of invariant mass pairs with $\cos\theta^* < 1$. The angle θ^* is that between the incoming quark that produces the intermediate Z/γ^* and the electron in the dielectron rest frame, with the z axis chosen such that it bisects the quark's direction of motion (see Figure 5.1). This is known as the Collins-Soper frame [52].

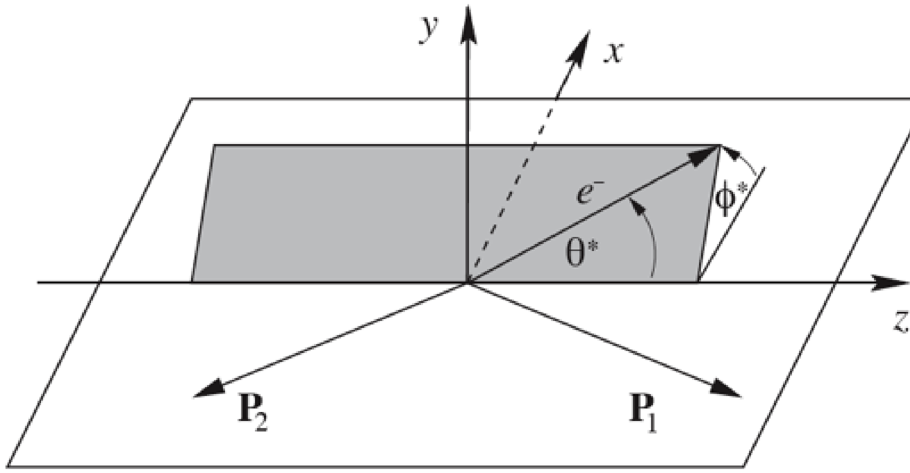

Figure 5.1. An illustration of the Collins-Soper frame used to define the angle θ^*, used in the calculation of A_{FB}.

Measurement of A_{FB} relies on the ability to identify accurately the momentum directions of the quark and electron shown in Figure 5.1. At a $p\overline{p}$ collider such as the Tevatron, the quark is with very high probability provided by the proton beam. However, at a pp collider like the LHC, the quark can originate from either proton beam with equal probability.

At the LHC, the most probable scenario for the origin of the quark and anti-quark pair is that of a valence quark and a sea anti-quark. As sea quarks carry a much smaller fraction of the proton's momentum than valence quarks do, the assumption is made that the Z/γ^* boson created from the annihilation of the $q\overline{q}$ pair follows the momentum direction of the quark. In this scheme, the quark direction is simply taken from the direction of the dielectron system.

The validity of this assumption as a function of Z rapidity is shown in Figure 5.2, measured using a simulated data sample. For increasingly high values of rapidity,

$|y_{ee}|$, the direction of the Z increasingly approximates the direction of the quark.

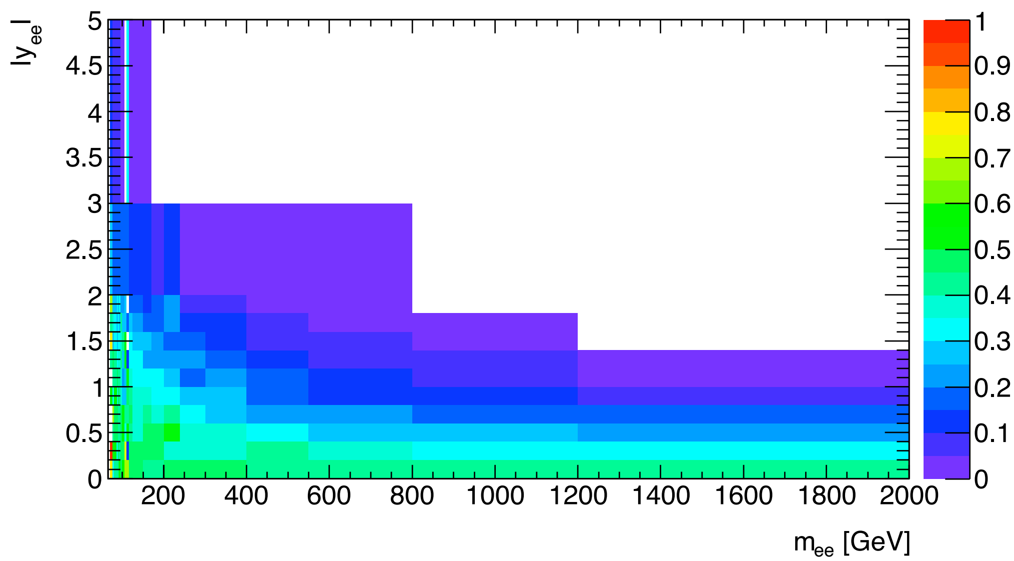

Figure 5.2. Probability (color-coded key) of selecting wrong quark direction by assuming the quark and dielectron directions of motion are equal, as a function of dielectron mass and rapidity. The probability is higher for lower $|y_{ee}|$. The information was obtained from a simulated sample of the Drell-Yan process.

Because of this, a rapidity cut is used in the measurement of A_{FB} vs dielectron mass. This allows for reasonable purity of events where the quark direction is correctly estimated. To minimize loss of efficiency from this cut, pairs with one electron with $|\eta| > 2.5$ are incorporated into the analysis. The design of the ATLAS calorimeter, described in Section 2.2.2, and the electron reconstruction algorithm discussed in Section 3.3.1 allow the use of electrons found at high psuedorapidity (η) values. This increases the number of high-rapidity $Z/\gamma*$ candidates observed.

5.2. Data sample and candidate selection

The sample used is of pp collision data collected during the 2011 run of the LHC up until June 28 2011, with the exception of seven runs taken in late March for which the solenoid magnet was not fully operational. Only runs and luminosity blocks that pass the Good Runs List (GRL) provided by the ATLAS eγ performance group are accepted. The e20_medium trigger is used, which selects events for which there is at least one electron passing medium quality requirements and having $p_T > 20$ GeV. The integrated luminosity of the sample is 1.073 fb^{-1}.

5.2.1. Event level selections

This section describes the preliminary selection performed for both analyses with only central electrons and with central and forward electrons. In both cases, one dielectron invariant mass pair per chosen event is used. In addition to the GRL and trigger described, selected events are as follows:

- The event contains at least one primary vertex with at least 3 associated tracks.
- The event passes cleaning requirements to eliminate noise bursts in the LAr calorimeter.

5.2.2. Central-central selection

This section describes the selection of dielectron pairs for which both objects are in the central region, $|\eta| < 2.5$. To be included in this analysis an event must contain two electrons reconstructed with the standard eγ reconstruction algorithm, described in Chapter 3, Section 3.1. The following requirements are placed on the electrons used in the analysis:

- Both electrons are central electrons, with "central" corresponding to a pseudorapidity region of $|\eta| < 2.47$, excluding the crack region between the barrel and endcaps of the LAr calorimeter ($1.37 < |\eta| < 1.52$). This crack region is excluded in most electron and photon analyses, as the reconstruction efficiency of electromagnetic objects is low there.

- Both electrons have transverse momentum greater than 25 GeV; this is calculated using energy information from the calorimeter, and in the case of a track with four combined hits in the pixel and silicon detectors, direction from the track. In the case that the electron's track does not have the appropriate number of hits, directional information from the calorimeter is used. In this case, the position information is taken from all layers in the calorimeter for which the electron has deposited some amount of energy.

- Both electrons pass object quality requirements as outlined in Chapter 3, Section 3.5.

- Both electrons pass medium quality cuts, as outlined in Chapter 3, Section 3.4.

- An opposite charge requirement is imposed.

- The absolute value of dielectron rapidity is required to be greater than 1.0. 44% of central-central pairs survive this selection.

5.2.3. Central-forward selection

In addition to pairs with two central electrons, pairs with one central and one forward electron (in the region $|\eta| > 2.5$ are also accepted, provided that certain requirements are met. To be included in this analysis an event must contain one electron reconstructed with the standard eγ reconstruction algorithm and a second electron reconstructed using the forward electron algorithm. The following requirements are placed on the electrons used in the analysis:

- The central electron must be in the η region as described for the central-central case and the forward electron must be within $2.5 < |\eta| < 4.9$.

- Both electrons are required to have p_T >25 GeV. For the central electron, the definition of p_T is as defined for the central-central analysis. The forward electrons must use $E_{T_{cluster}}$ as they are reconstructed outside the tracking volume.
- Both electrons pass object quality requirements.
- Both electrons pass tight quality cuts (standard electron tight in the case of the central electron, and forward tight in the case of the forward electron).
- The charge of forward electrons cannot be identified, so no charge requirement is imposed. The charge of the forward electron is taken to be opposite that of the central electron.
- The absolute value of dielectron rapidity is required to be greater than 1.0. 99.45% of central-forward pairs survive this selection.

For each event, an attempt is made to reconstruct both central-central and central-forward invariant masses. 87 overlapping events have been found, and these have been discarded.

5.3. Background estimate

In the case of both the central-central and the central-forward analyses, the non-dijet backgrounds have been estimated as described in Section 4.4.[1] The dijet background estimate uses a similar approach to that described in Section 4.4.2.1.

5.3.1. Dijet background estimated from data

The central-central dijet estimate is performed in the same way as was described in Section 4.4.2.1. In addition to the selection requirements previously listed, the

[1]Note that for this analysis the Drell-Yan simulated sample is the expected signal, and not a contribution to the background.

electrons are required to have opposite charge and the dielectron rapidity cut is also imposed ($|y_{ee}| > 1.0$). The templates from Samples A and B are shown normalized to each other in Figure 5.3, with a magnified version given in Figure 5.4. Recall that Sample A is constructed from a data set for which the 2g20_loose trigger is passed, with both electrons having p_T >25 GeV, and passing loose quality requirements while failing medium quality requirements. Sample B is constructed from a data set for which the e60_loose trigger is passed, with the leading electron having p_T >65 GeV, and passing loose quality requirements while failing medium quality requirements. The subleading electron is required to have p_T >25 GeV and fail medium quality requirements. (See Section 4.4.2.1 for further explanation.) The final central-central dijet template is shown in Figure 5.5.

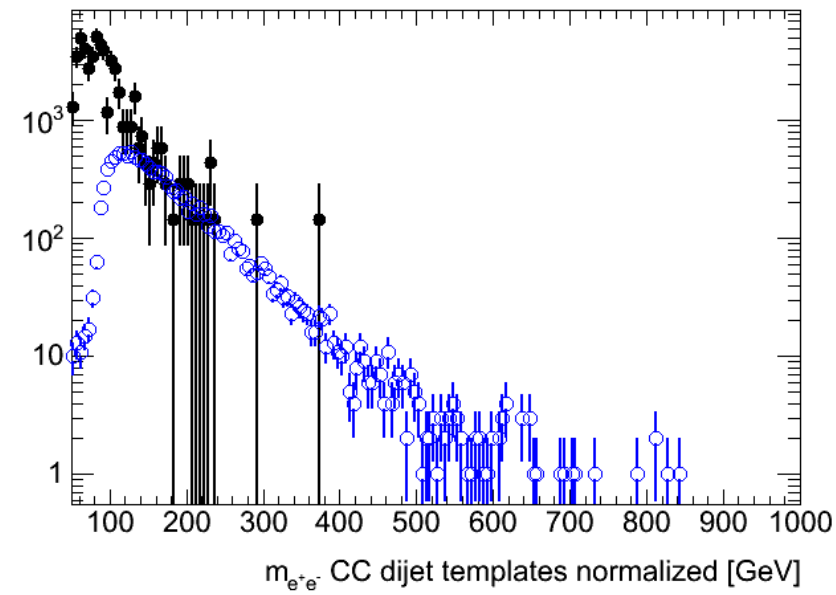

Figure 5.3. The two templates used to estimate dijet events in the central-central channel. The black dots represent the distribution used to describe low mass events below the turn-on curve of the high mass distribution (blue circles). The high mass distribution is used for events with m_{ee} >180 GeV. The templates are normalized to each other in the region 130< m_{ee} <240 GeV.

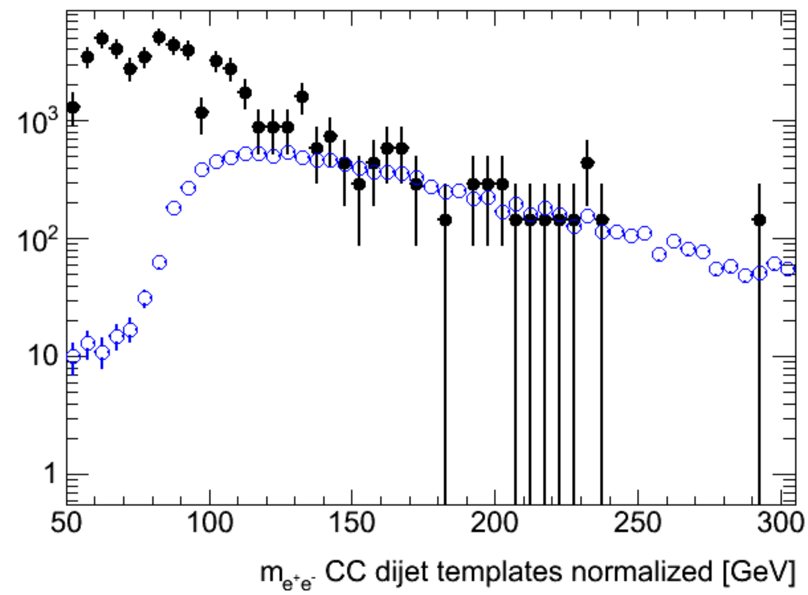

Figure 5.4. The two templates used to estimate the dijet events in the central-central channel. The mass region containing the turn-on curve for the high mass sample and the region used for normalization are emphasized in this plot.

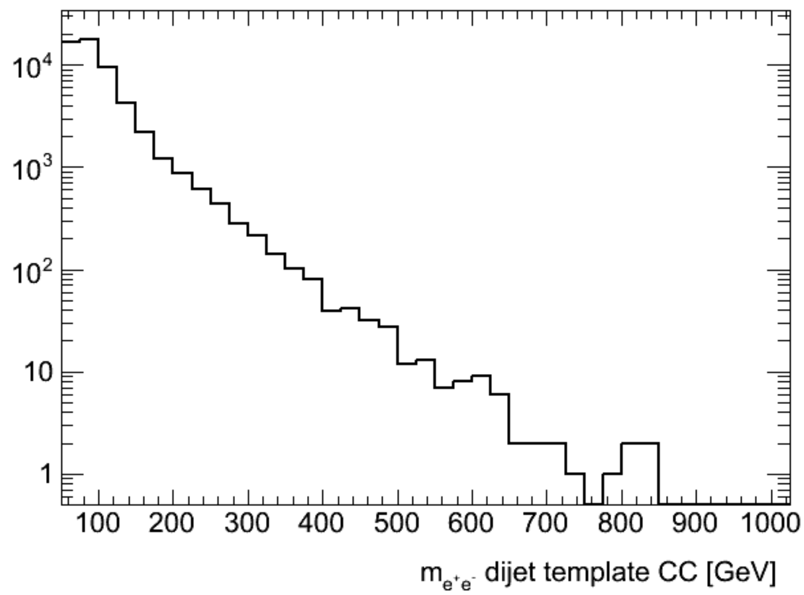

Figure 5.5. The template used to estimate dijet events in the central-central channel.

In the central-forward case, the dijet template is obtained from data using the following requirements:

- The e20_medium trigger is used.
- The central electron passes standard electron medium quality requirements, but fails tight quality requirements.
- The forward electron passes the forward electron loose quality requirements, but fails forward electron tight quality requirements.
- The central electron is required to have a calorimetric isolation greater than 7 GeV. This means that the sum of all track-based energies in a cone of radius 0.4 around the electron's track must be greater than 7 GeV. The isolation variable is corrected for the electron's own energy and for contributions from the underlying event.

As with the central-central case, the dielectron rapidity cut $|y_{ee}| > 1.0$ is imposed. The resulting template is shown in Figure 5.6.

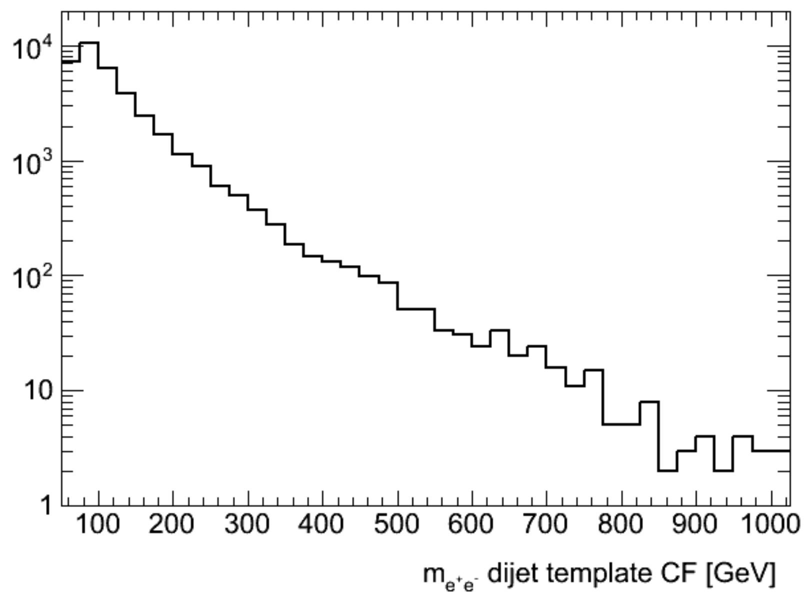

Figure 5.6. The template used to estimate dijet events in the central-forward channel.

These templates, along with the histograms of signal and background estimates of other processes from simulated samples, are fit to the data using a binned maximum likelihood fit [66]. The expected number of background events from a process, after normalization to the data, in bin i is given by [58]:

$$f_i = N_D \sum_{j=1}^{m} \frac{P_j A_{ji}}{N_j}, \tag{5.2}$$

where m is the number of input distributions, N_D is the number of observed events on data in bin i, N_j is the total number of events in distribution j (integrated over all bins), P_j is the fraction of the data distribution that can be described by input distribution j and A_{ij} is the un-normalized number of observed events in bin i in the input distribution j. Here the A_{ij} include uncertainties.

In calculating the maximum likelihood, the probabilities of observing a given number of data events, d_i, and a given number of events described by simulated samples or a background template, a_{ji}, are used. These probabilities follow a Poisson distribution:

$$
\begin{aligned}
P(d_i; f_i) &= e^{-f_i} \frac{f_i^{d_i}}{d_i!}, \\
P(a_{ji}; A_{ji}) &= e^{-A_{ji}} \frac{A_{ji}^{a_{ji}}}{a_{ji}!}.
\end{aligned} \tag{5.3}
$$

The natural logarithm of the likelihood is then given by:

$$
\ln L = \ln P(d_i; f_i) + \ln P(a_{ji}; A_{ji}) = \sum_{i=1}^{n} (d_i \ln f_i) - f_i + \sum_{i=1}^{n} \sum_{j=1}^{m} (a_{ji} \ln A_{ji}) - A_{ji}. \tag{5.4}
$$

The desired outcome is to know the value of P_j. This parameter is estimated by maximizing the likelihood of (5.4). To do this, the fitting program MINUIT [42] is used within a class of the ROOT [67] data analysis framework called TFractionFitter [75].

5.4. Number of observed and expected events

Shown in Tables 5.1 and 5.2 is the total number of events that were observed in the data using the central-central and central-forward analyses, along with the expected amount of background in each invariant mass bin used for the measurement. The uncertainties are statistical only. Central values or uncertainties listed as '0' correspond to values of less than 0.05. Fractional values occur for background estimates. This may happen as the number of events is taken from the normalization of the templates described in the previous section via a fit to the data.

Combined expected signal and background plots for the dielectron invariant mass are shown in Figure 5.7. The cos θ^* distributions for the backgrounds are shown in

Figures 5.8 (CC) and 5.9 (CF). The distribution of A_{FB} corrected for the presence of background is shown in Figure 5.10 for the central-central channel, Figure 5.11 for the central-forward and Figure 5.12 for all events.

Table 5.1. Summary of number of observed and expected events for the central-central analysis. Fractions of events are due to normalization.

m_{ee} [GeV]	70-80	80-85	85-87	87-89
Drell Yan	5647.0 ± 515.6	11815.0 ± 746.2	8136.2 ± 619.2	16809.1 ± 890.0
Diboson	33.3 ± 1.3	27.8 ± 0.9	23.0 ± 0.7	45.2 ± 1.0
$W \to e\nu$	65.8 ± 17.3	91.9 ± 20.5	16.5 ± 8.7	0 ± 0
$t\bar{t}$	18.7 ± 1.9	8.5 ± 1.3	7.3 ± 1.2	4.4 ± 0.9
Dijet	301.6 ± 46.0	245.5 ± 41.5	98.2 ± 26.2	91.2 ± 25.3
Total est.	6066.4 ± 517.9	12188.8 ± 747.6	8281.2 ± 619.8	16949.9 ± 890.4
Data	6735 ± 82.1	13984 ± 118.2	13373 ± 115.6	20657 ± 143.7
m_{ee} [GeV]	89-91	91-93	93-95	95-100
Drell Yan	26140.0 ± 1109.9	25182.9 ± 1089.3	14280.6 ± 820.3	9469.6 ± 668.0
Diboson	75.1 ± 1.3	76.6 ± 1.3	43.1 ± 1.0	38.2 ± 1.0
$W \to e\nu$	0 ± 0	24.3 ± 10.6	16.3 ± 8.6	61.0 ± 16.7
$t\bar{t}$	2.6 ± 0.7	1.3 ± 0.5	1.5 ± 0.5	9.7 ± 1.4
Dijet	63.1 ± 21.0	77.2 ± 23.3	77.2 ± 23.3	56.1 ± 19.8
Total est.	26280.8 ± 1110.0	25362.4 ± 1089.6	14418.7 ± 820.7	9634.6 ± 668.5
Data	26386 ± 162.4	21268 ± 145.8	9800 ± 99.0	6485 ± 80.5
m_{ee} [GeV]	100-110	110-120	120-250	250-1000
Drell Yan	2988.3 ± 374.4	730.1 ± 170.7	1928.6 ± 34.7	124.0 ± 2.4
Diboson	23.0 ± 1.0	12.8 ± 0.8	63.1 ± 2.1	5.5 ± 0.5
$W \to e\nu$	46.9 ± 14.7	8.9 ± 6.4	135.4 ± 24.9	0 ± 0
$t\bar{t}$	12.3 ± 1.6	10.2 ± 1.4	63.6 ± 8.3	7.4 ± 0.3
Dijet	287.6 ± 44.9	126.3 ± 29.8	357.0 ± 4.2	70.7 ± 1.8
Total est.	3358.1 ± 377.3	888.3 ± 173.4	2547.7 ± 255.0	207.6 ± 19.6
Data	2775 ± 52.7	973 ± 31.2	1936 ± 44.0	127 ± 11.3

Table 5.2. Summary of number of observed and expected events for the central-forward analysis. Fractions of events are due to normalization.

m_{ee} [GeV]	70-80	80-85	85-87	87-89
Drell Yan	2006.2 ± 293.2	4320.5 ± 430.3	3847.5 ± 406.0	6598.2 ± 531.7
Diboson	9.7 ± 0.7	7.1 ± 0.4	6.4 ± 0.4	11.0 ± 0.5
$W \to e\nu$	241.8 ± 31.7	111.8 ± 21.6	39.6 ± 12.8	47.6 ± 14.1
$t\bar{t}$	0 ± 0	1.2 ± 0.5	0 ± 0	0 ± 0
Dijet	160.4 ± 2.4	80.2 ± 1.7	34.0 ± 1.1	33.1 ± 1.1
Total est.	2418.2 ± 294.9	4520.8 ± 430.8	3927.5 ± 406.2	6689.9 ± 531.9
Data	3039 ± 55.1	6834 ± 82.7	6333 ± 79.6	9288 ± 96.4
m_{ee} [GeV]	89-91	91-93	93-95	95-100
Drell Yan	11324.1 ± 696.6	10797.9 ± 680.2	7659.3 ± 572.9	10156.8 ± 659.6
Diboson	18.8 ± 0.6	19.1 ± 0.6	12.5 ± 0.5	16.0 ± 0.6
$W \to e\nu$	34.7 ± 12.0	33.6 ± 12.0	70.0 ± 17.1	125.8 ± 22.9
$t\bar{t}$	0 ± 0	0 ± 0	0 ± 0	1.5 ± 0.5
Dijet	31.6 ± 1.1	33.5 ± 1.1	28.4 ± 1.0	67.8 ± 1.6
Total est.	11409.3 ± 696.7	10884.1 ± 680.3	7770.2 ± 573.1	10368.0 ± 660.0
Data	11103 ± 105.4	9812 ± 99.1	6450 ± 80.3	6016 ± 77.6
Mass m_{ee} [GeV]	100-110	110-120	120-250	250-1000
Drell Yan	2107.5 ± 299.7	1257.6 ± 225.8	1089.8 ± 24.9	60.2 ± 1.7
Diboson	8.6 ± 0.5	8.5 ± 0.8	45.4 ± 1.8	10.8 ± 0.9
$W \to e\nu$	197.3 ± 28.7	180.9 ± 27.4	1026.4 ± 65.4	119.0 ± 22.3
$t\bar{t}$	1.6 ± 0.5	2.5 ± 0.7	4.9 ± 0.8	1.4 ± 0.4
Dijet	110.5 ± 2.0	90.6 ± 1.8	407.1 ± 3.9	106.4 ± 2.0
Total est.	2425.4 ± 301.1	1540.0 ± 227.5	2573.6 ± 70.1	297.9 ± 22.4
Data	2260 ± 47.5	880 ± 29.7	2576 ± 50.7	396 ± 19.9

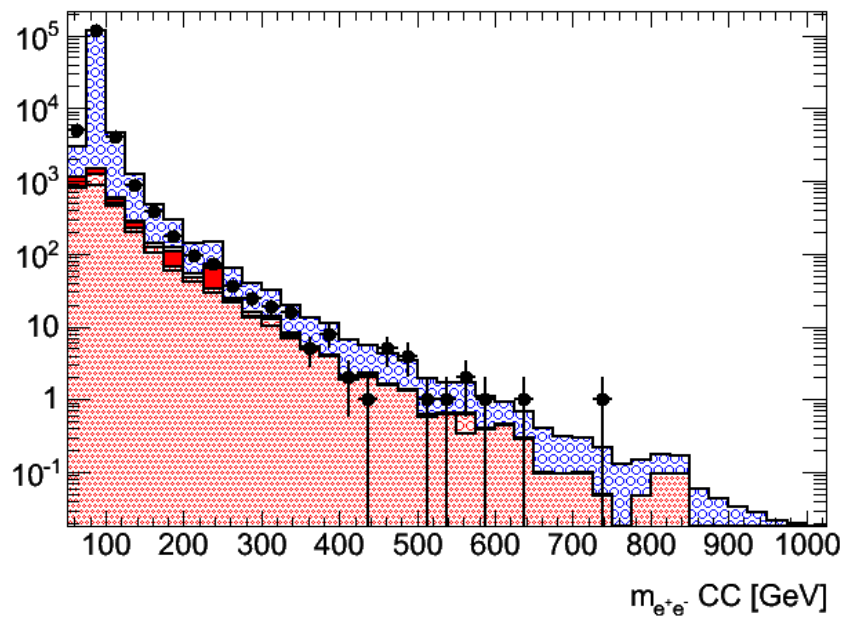

a)

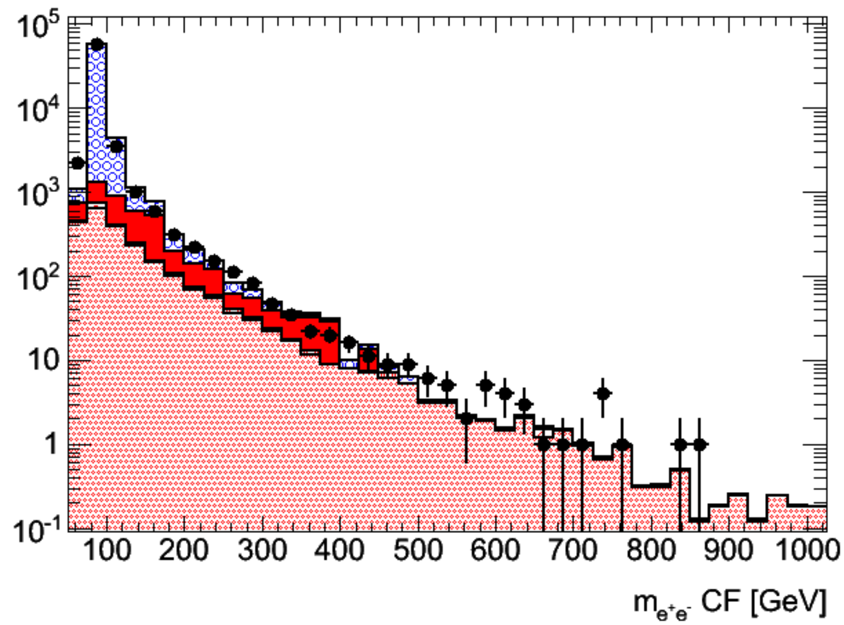

b)

Figure 5.7. Dielectron invariant mass for a) central-central and b) central-forward events. This reflects the numbers given in Tables 5.1 and 5.2. The number of events observed in the data is shown by the black points, while the various background estimates described are (from bottom to top): dijet events (small red circles), diboson (large red circles), $t\bar{t}$ (red hash lines), W$\rightarrow$eν (solid red) and Z/γ^* $\rightarrow$ee (blue large circles).

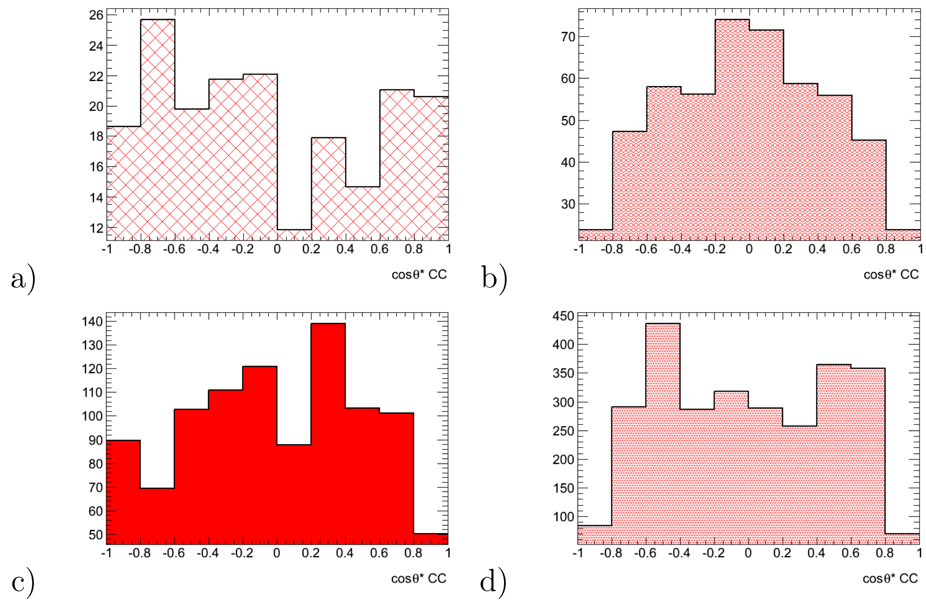

Figure 5.8. cos θ^* distributions for CC pairs in the (a) $t\bar{t}$, (b) diboson, (c) W→eν and (d) dijet samples.

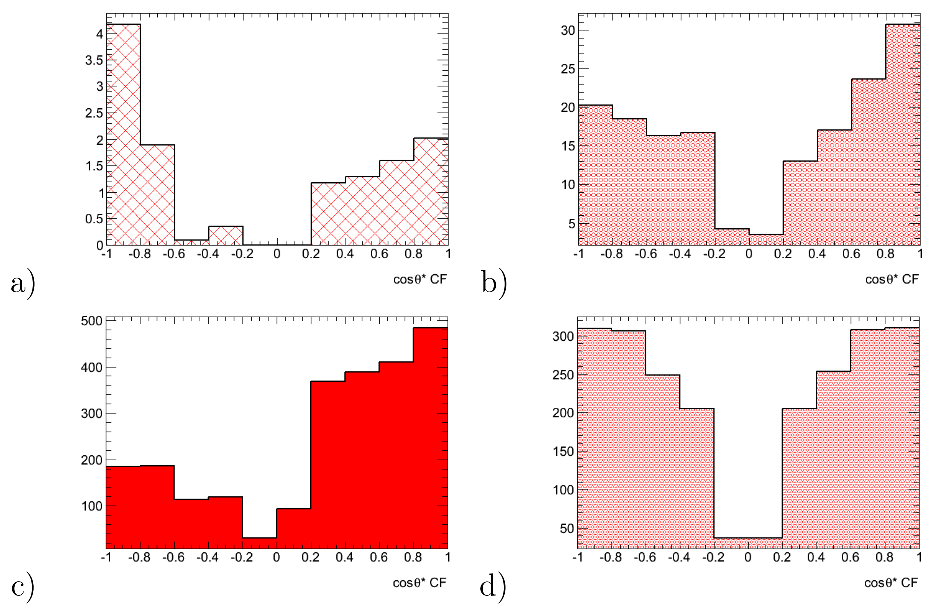

Figure 5.9. cos θ^* distributions for CF pairs in the (a) $t\bar{t}$, (b) diboson, (c) W→eν and (d) dijet samples.

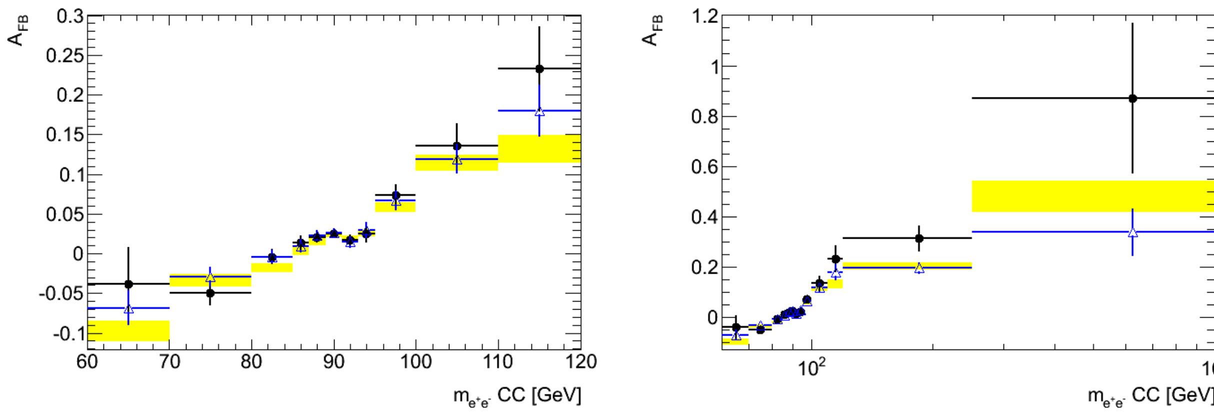

Figure 5.10. A_{FB} vs dielectron invariant mass for central-central pairs. The yellow bars indicate the Standard Model expectation as taken from reconstructed events on simulated data. The blue triangles show the uncorrected distribution, while the black dots show the value as corrected for the presence of background. Errors are statistical. The left plot shows the Z peak region in more detail.

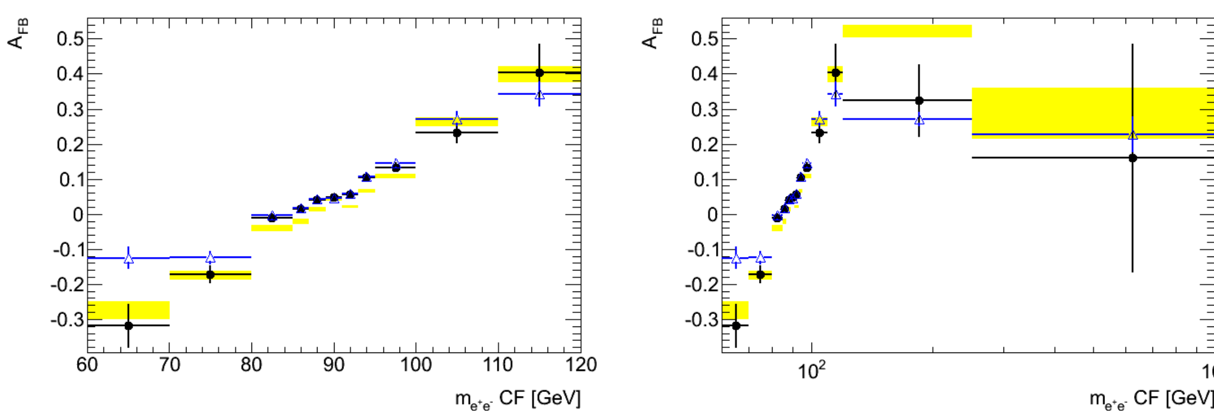

Figure 5.11. A_{FB} vs dielectron invariant mass for central-forward pairs. The yellow bars indicate the Standard Model expectation as taken from reconstructed events on simulated data. The blue triangles show the uncorrected distribution, while the black dots show the value as corrected for the presence of background. Errors are statistical. The left plot shows the Z peak region in more detail.

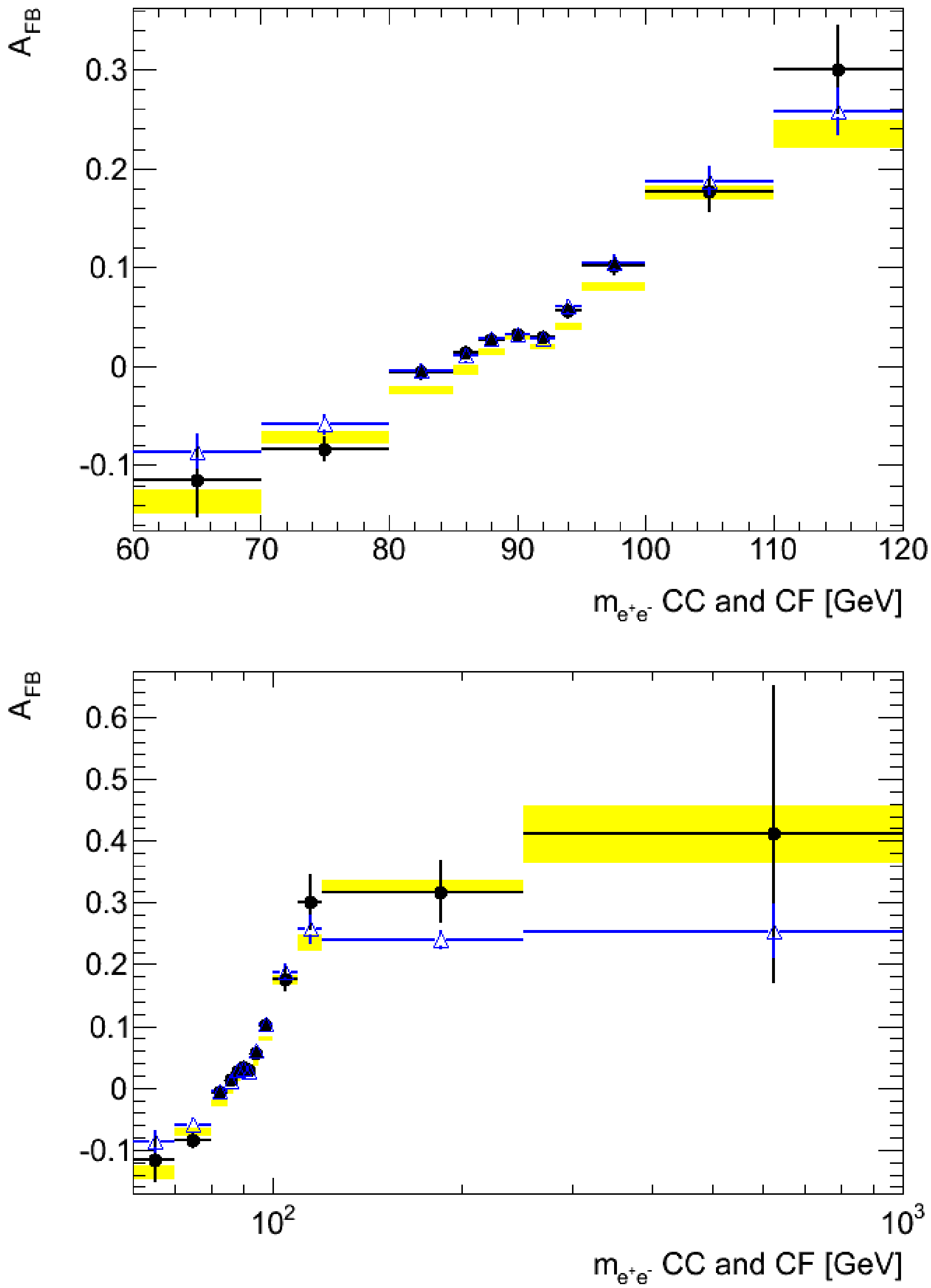

Figure 5.12. A_{FB} vs dielectron invariant mass for all electron pairs used in the analysis. The yellow bars indicate the Standard Model expectation as taken from reconstructed events on simulated data. The blue triangles show the uncorrected distribution, while the black dots show the value as corrected for the presence of background. Errors are statistical. The top plot shows the Z peak region in more detail.

5.5. Measurement of electron charge misidentification

Charge misidentification can affect the measurement of A_{FB} in one of two ways: in the first, one object from the true e^+e^- pair has misidentified charge, and so when the event is reconstructed it does not pass the opposite charge requirement of the analysis. This effect of the charge misidentification manifests itself as a loss of efficiency. This has been taken into account by correcting the Monte Carlo expected A_{FB} distribution with a data vs. Monte Carlo efficiency scale factor. The second way charge misidentification becomes important for this measurement occurs when both electron and positron have misidentified charge. In this case, the event still passes analysis selections, but an incorrect direction for the electron has been taken to calculate the value of $\cos\theta^*$. This case is discussed in this section.

To correct for the effect of charge misidentification of both electrons, a measurement of the charge identification efficiency for positive and negative charges is needed. I made this measurement using the tag and probe method. The tag and probe method uses probabilities of final states to calculate efficiencies. It relies on selecting two objects, the tag, which is chosen first and must conform to very stringent requirements, and the probe, chosen secondly, which is allowed to conform to looser requirements.

The tag and probe method relies on obtaining a sample of objects in the data that can reasonably be identified as 'real' electrons. This is accomplished by selecting Z→ee events, with one electron chosen as the tag and the other as the probe.

The specific cuts that the tag and the probe must pass vary with the measurement being made; the cuts used for this measurement are listed below.

The following selection criteria are applied at the event level:

- Good Runs List
- e20_medium trigger is used
- At least one primary vertex with >=3 associated tracks
- Noise burst removal

A tag electron is selected according to:

- Electron is reconstructed using the standard $e\gamma$ algorithm.
- The position in η is within $|\eta| < 0.8$. (Previous charge efficiency studies have indicated this to be the region with the lowest rate of charge misidentification [19].)
- Electron p_T is greater than 25 GeV.
- Electron passes object quality requirements.
- Electron passes tight identification requirement.
- The highest p_T electron in the event satisfying the above requirements is chosen as the tag.

Two probe electrons are selected per event and are required to meet the same requirements as the tag, with the following exceptions:

- The position in η is within $|\eta| < 2.5$ with the region $1.37 < |\eta| < 1.52$ excluded.
- Electron passes medium identification requirement.
- Electron charge is required to be opposite that of the tag electron in the case of the oppositely charged probe, and the same as that of the tag electron in the case of the same sign probe.

- The highest p_T same sign and opposite sign probes in the event satisfying the above requirements are chosen.

5.5.1. Derivation of formulas to calculate efficiencies with tag and probe method

Consider the four final dielectron states possible with the tags and probes as found by the selection criteria listed above:

1. ++: Positively charged tag, same-sign probe (also positive).
2. +-: Positively charged tag, opposite-sign probe (negative).
3. -+: Negatively charged tag, opposite-sign probe (positive).
4. $--$: Negatively charged tag, same-sign probe (also negative).

Given that a positron (electron) is reconstructed, there exists an efficiency that it is correctly identified as positive (negative), ϵ_p (ϵ_m), and a probability that it is misidentified as negative (positive), ρ_p (ρ_m).

Then, the probability of the ++ state is given by:

$$\begin{aligned} P(T_pP_p) &= P(T_p)P(P_p|T_p) \\ &= (\epsilon_p + \rho_p)\rho_p. \end{aligned} \tag{5.5}$$

Similarly, the probabilities of the other final states are as follows:

$$\begin{aligned} P(T_pP_m) &= (\epsilon_p + \rho_p)\epsilon_m, \\ P(T_mP_p) &= (\epsilon_m + \rho_m)\epsilon_p, \\ P(T_mP_m) &= (\epsilon_m + \rho_m)\rho_m. \end{aligned} \tag{5.6}$$

Note that for any reconstructed electron, there are only two possible alternatives: the electron can be correctly identified as negative, or misidentified as positive.

Therefore, the sum of these probabilities must be 100%:

$$\epsilon_m + \rho_p = 1, \epsilon_p + \rho_m = 1. \tag{5.7}$$

Ratios of the probabilities given in (5.5) and (5.6) are then used to obtain the charge identification efficiencies, ϵ_p and ϵ_m, or the charge misidentification rates, ρ_p and ρ_m:

$$\frac{P(T_pP_m)}{P(T_pP_m)+P(T_pP_p)} = \frac{\epsilon_m(\epsilon_p+\rho_p)}{(\epsilon_m+\rho_p)(\epsilon_p+\rho_p)} = \epsilon_m, \tag{5.8}$$

$$\frac{P(T_mP_p)}{P(T_mP_p)+P(T_mP_m)} = \frac{\epsilon_p(\epsilon_m+\rho_m)}{(\epsilon_p+\rho_m)(\epsilon_m+\rho_m)} = \epsilon_p, \tag{5.9}$$

$$\frac{P(T_mP_m)}{P(T_mP_m)+P(T_mP_p)} = \frac{\rho_m(\epsilon_m+\rho_m)}{(\epsilon_p+\rho_m)(\epsilon_m+\rho_m)} = \rho_m, \tag{5.10}$$

$$\frac{P(T_pP_p)}{P(T_pP_p)+P(T_pP_m)} = \frac{\rho_p(\epsilon_p+\rho_p)}{(\epsilon_m+\rho_p)(\epsilon_p+\rho_p)} = \rho_p. \tag{5.11}$$

While these probabilities are not directly obtained from the data, they are reflected in the number of ++, +-, -+ and $--$ pairs observed:

$$N(ee)_{obs} = P(ee)N(ee)_{true} \tag{5.12}$$

where $N(ee)_{obs}$ is the number of observed dielectron events, $P(ee)$ is the probability of this final state and $N(ee)_{true}$ is the number of true dielectron events. When replacing probabilities with number of observed events in (5.8) through (5.11), $N(ee)_{true}$ cancels out and the equations remain the same.

5.5.2. η dependence measured on collision data with tag and probe method

The measurement is performed in eight η bins, with two bins in each side of the barrel and two in each of the endcaps. Using the selection criteria previously described, I made the following measurements of charge identification efficiencies:

Table 5.3. Charge identification efficiencies measured on collision data with Z$\rightarrow$ee tag and probe. The results are binned in electron η.

$\eta =$	[-2.47, -2.0]	[-2.0, -1.52)	(1.37, -0.8]	[-0.8, 0.0]
$\epsilon_p =$	$(96.67 \pm 1.05)\%$	$(97.89 \pm 2.02\%)$	$(99.59 \pm 1.00\%)$	$(99.66 \pm 0.98)\%$
$\epsilon_m =$	$(96.40 \pm 1.32)\%$	$(97.71 \pm 1.90)\%$	$(99.57 \pm 0.92)\%$	$(99.75 \pm 1.36)\%$
$\eta =$	[0.0, 0.8]	[0.8, 1.37)	(1.52, 2.0]	[2.0, 2.47]
$\epsilon_p =$	$(99.61 \pm 1.07)\%$	$(99.48 \pm 1.42)\%$	$(98.55 \pm 1.66)\%$	$(97.12 \pm 1.02)\%$
$\epsilon_m =$	$(99.53 \pm 1.29)\%$	$(99.44 \pm 0.98)\%$	$(97.68 \pm 2.03)\%$	$(95.34 \pm 1.28)\%$

The results are extracted from data using a combined signal + background fit. The signal is modeled by a Breit Wigner convoluted with a Crystal Ball function, and the background by an exponential. The data is fit with the combined signal + background probability distribution function and the fraction signal is returned from the fit. This is used to obtain the number of events in each dielectron final state. The data distributions along with the fits are shown in Figures 5.13 through 5.16.

5.5.3. p_T dependence from simulated data

Charge misidentification occurs due to two causes:

- Matching of an incorrect track to an electron's cluster. This is expected to improve with stricter requirements on track-cluster matching, but at electron p_T values higher than 20 GeV is largely p_T independent.
- Very high p_T electrons, those with $p_T > 500$ GeV, have practically straight tracks for which it is difficult to measure the curvature. To measure the charge

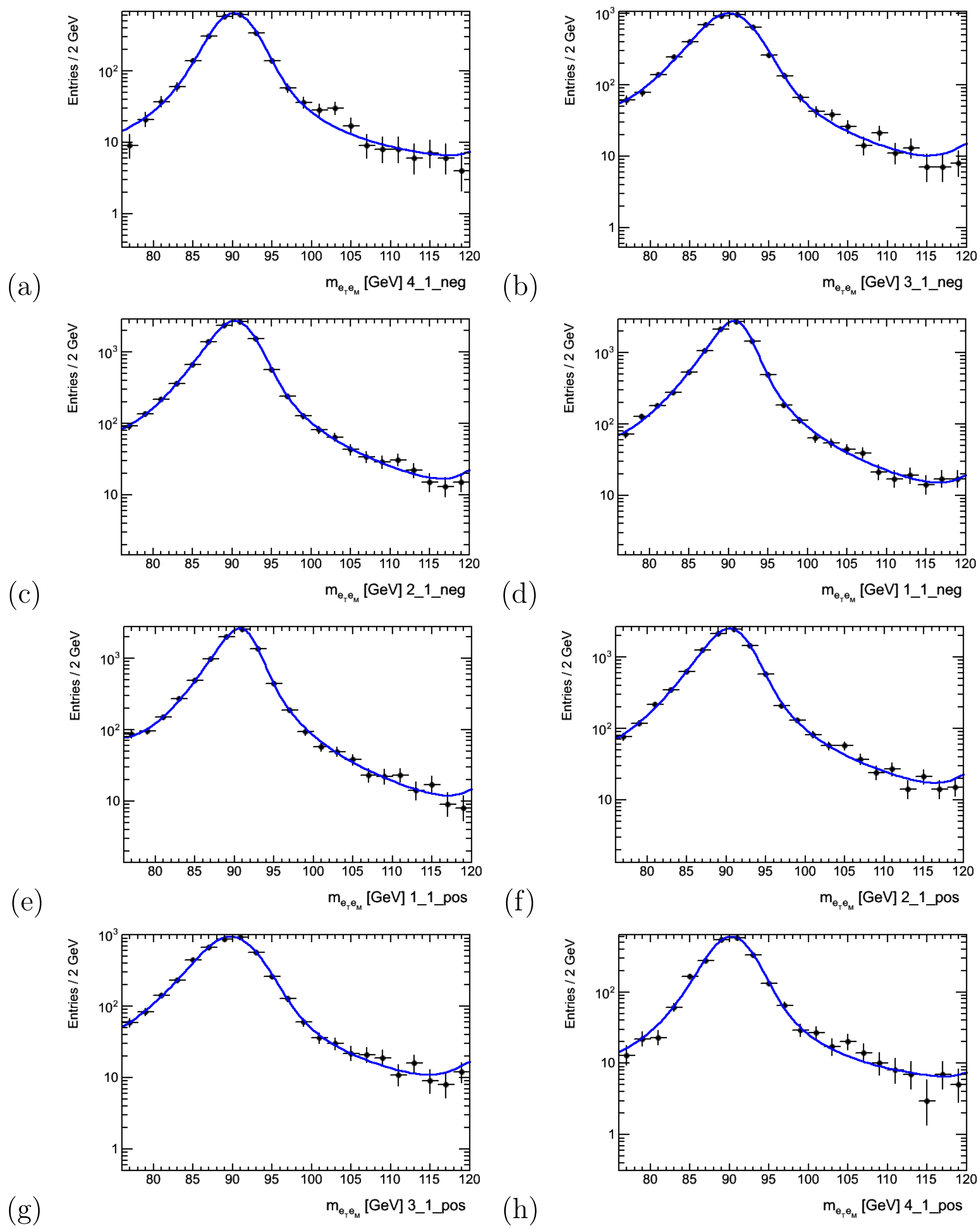

Figure 5.13. $+-$ masses in the eight η bins used: (a) [-2.47, -2.0], (b) [-2.0, -1.52), (c) (-1.37,-0.8], (d) [-0.8, 0.0], (e) [0.0, 0.8], (f) [0.8, 1.37), (g) (1.52, 2.0] and (h) [2.0, 2.47].

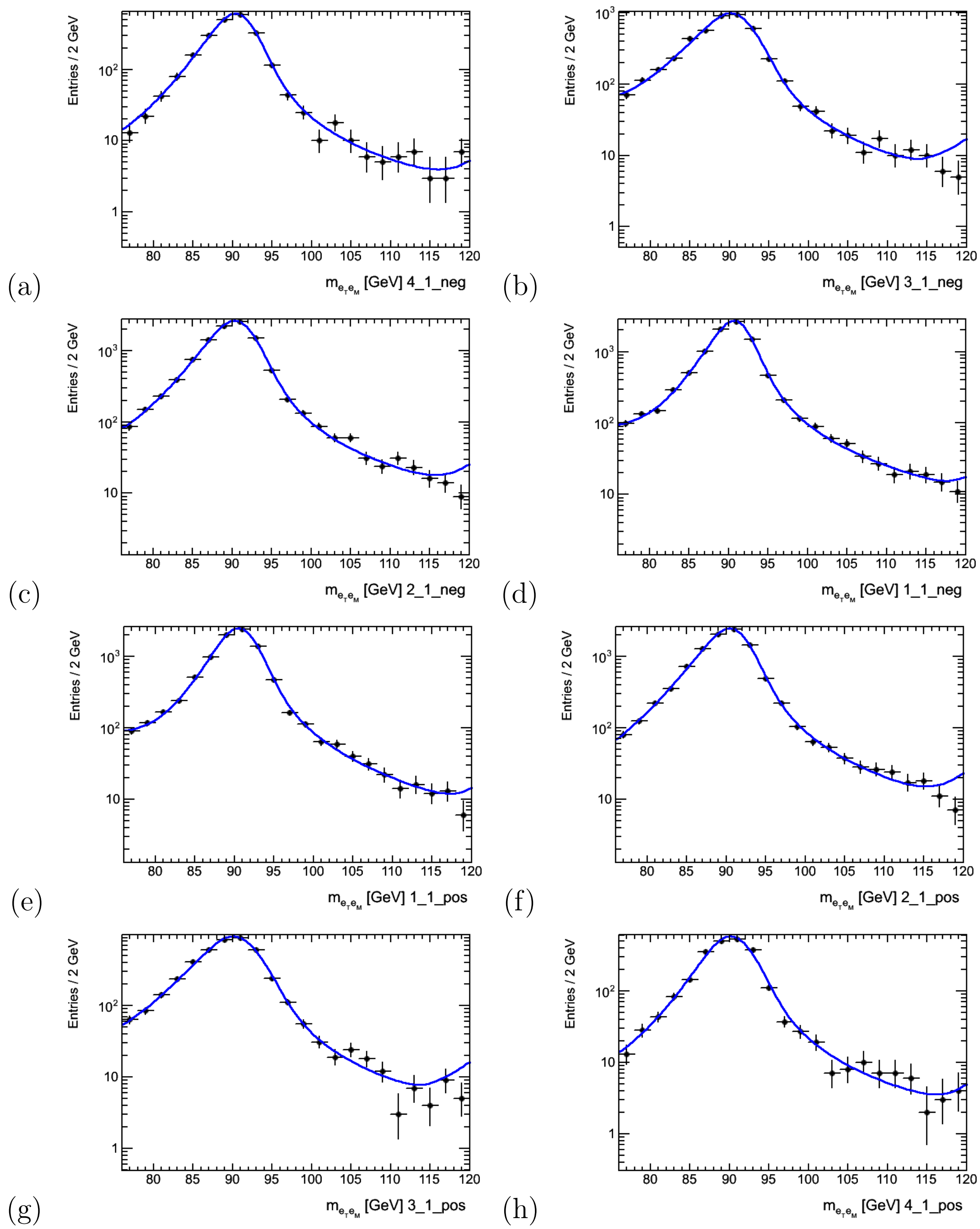

Figure 5.14. −+ masses in the eight η bins used: (a) [-2.47, -2.0], (b) [-2.0, -1.52), (c) (-1.37,-0.8], (d) [-0.8, 0.0], (e) [0.0, 0.8], (f) [0.8, 1.37), (g) (1.52, 2.0] and (h) [2.0, 2.47].

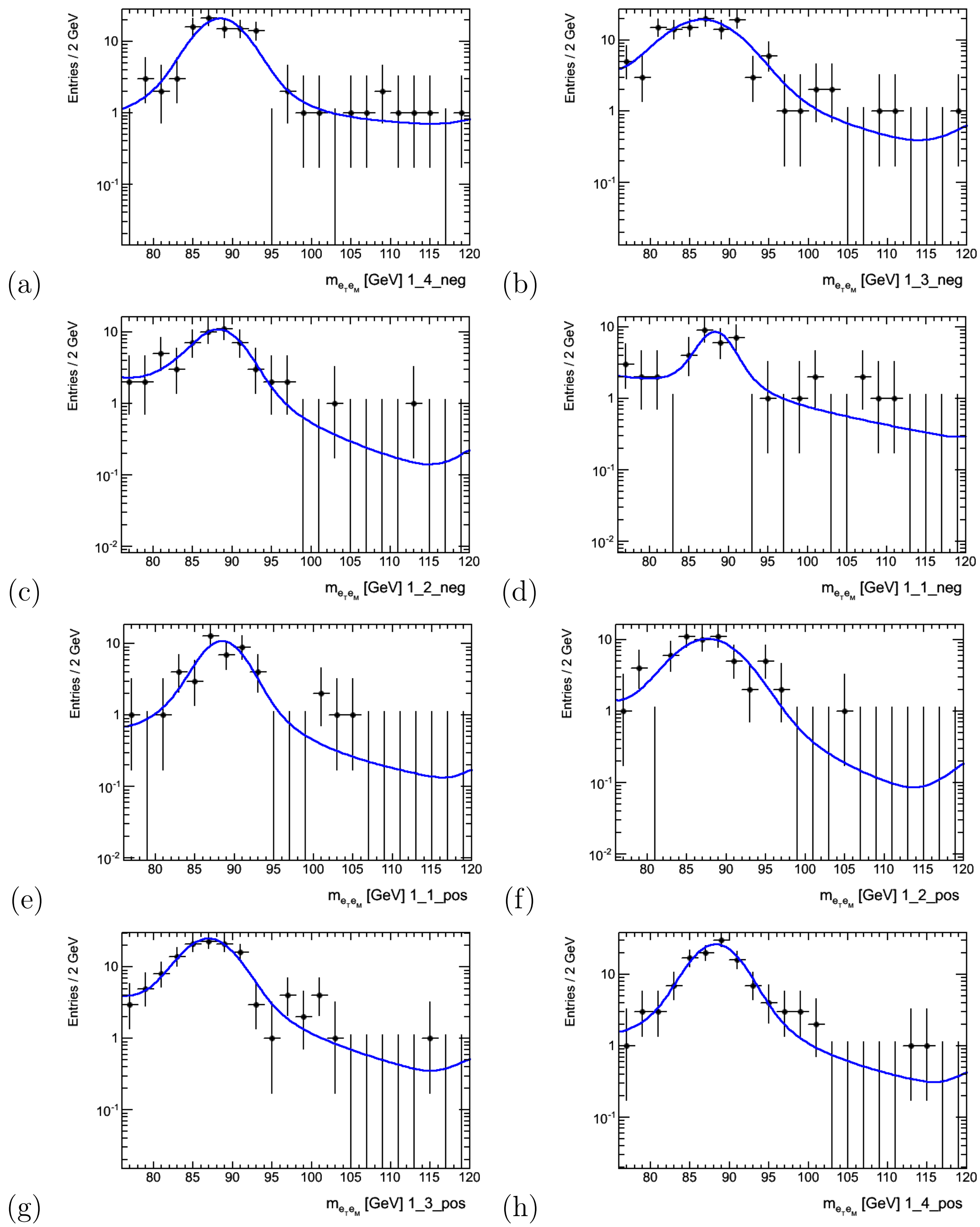

Figure 5.15. ++ masses in the eight η bins used: (a) [-2.47, -2.0], (b) [-2.0, -1.52), (c) (-1.37,-0.8], (d) [-0.8, 0.0], (e) [0.0, 0.8], (f) [0.8, 1.37), (g) (1.52, 2.0] and (h) [2.0, 2.47].

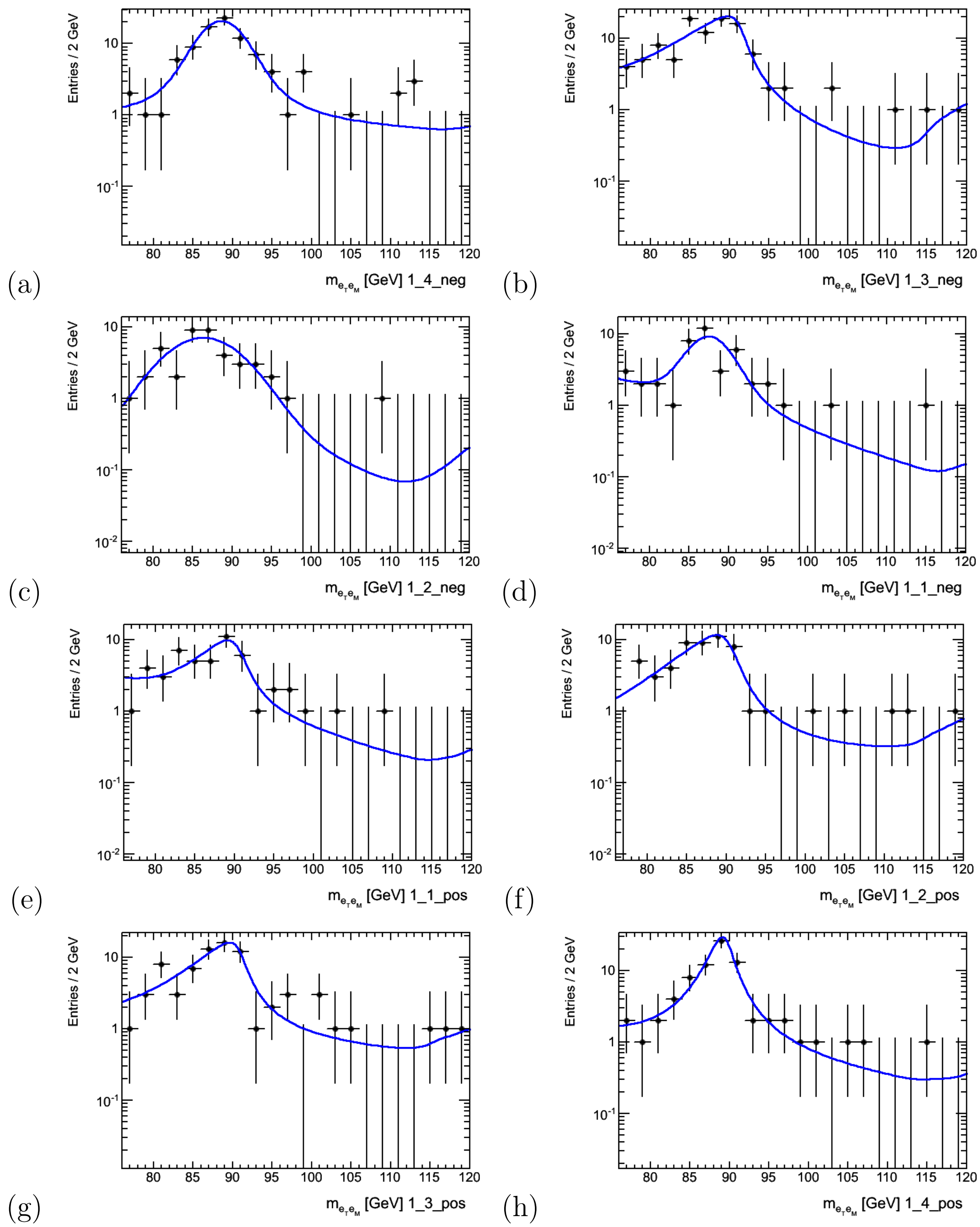

Figure 5.16. – – masses in the eight η bins used: (a) [-2.47, -2.0], (b) [-2.0, -1.52), (c) (-1.37,-0.8], (d) [-0.8, 0.0], (e) [0.0, 0.8], (f) [0.8, 1.37), (g) (1.52, 2.0] and (h) [2.0, 2.47].

identification efficiency in p_T bins for such high p_T electrons, a larger amount of data than has been collected is necessary. Because of this, the p_T binned measurements presented here have been taken from simulated samples of the Drell-Yan process.

Due to the fact that there are no constraints imposed by a trigger when using simulated samples, the p_T binned study is made over a larger p_T range than the data based, η binned measurement[2]. The statistical uncertainty on the values from these samples is negligible. The results of the p_T binned study are shown in Table 5.4.

[2]The data based study requires a p_T cut of 25 GeV, whereas the study on simulated samples goes down to p_T =15 GeV.

Table 5.4. Charge identification efficiencies measured on a simulated sample of the Drell-Yan process. The results are binned in electron p_T. The statistical uncertainty on the values from the samples is negligible.

p_T (GeV) =	[15, 20]	[20, 25]	[25, 30]	[30, 35]	[35, 40]	[40, 45]
ϵ_p =	99.26%	99.75%	99.52%	99.48%	99.39%	99.74%
ϵ_m =	99.92%	99.40%	99.72%	99.82%	99.52%	99.60%
p_T (GeV) =	[45, 50]	[50, 60]	[60, 70]	[70, 80]	[80, 90]	[90, 100]
ϵ_p =	99.79%	99.62%	99.26%	99.71%	99.80%	99.42%
ϵ_m =	99.65%	99.51%	99.43%	99.39%	98.76%	99.24%
p_T (GeV) =	[100, 125]	[125, 150]	[150, 175]	[175, 200]	[200, 250]	[250, 300]
ϵ_p =	99.36%	99.34%	99.43%	99.29%	99.46%	99.49%
ϵ_m =	99.78%	99.30%	98.96%	98.66%	98.96%	98.63%
p_T (GeV) =	[300, 350]	[350, 400]	[400, 500]	[500, 600]	[600, 700]	[700, 800]
ϵ_p =	99.49%	99.12%	99.12%	98.58%	98.26%	97.89%
ϵ_m =	98.90%	98.55%	98.63%	97.59%	97.02%	96.41%
p_T (GeV) =	[800, 1000]					
ϵ_p =	97.09%					
ϵ_m =	96.25%					

5.5.4. Corrected vs uncorrected cos θ^* distributions

The A_{FB} vs mass distribution observed on the data is corrected using the binned efficiency measurements of the previous section. In the central-central case, a correction factor for each electron is applied. In the central-forward case, a correction factor is applied only for the central electron, as the charge of the forward electron is inferred from the charge of the central one. The corrected cos θ^* distributions in each invariant mass bin used in the measurement versus the uncorrected distribution are shown in Figure 5.17. It can be seen that the corrected distribution is in all cases within statistical error of the uncorrected distribution. Ultimately, the charge misidentification effect is negligible, as can be seen in Figure 5.18, where a comparison of the corrected versus uncorrected A_{FB} spectra is made for all mass bins.

5.6. Conclusions

The A_{FB} vs dielectron mass distribution observed on the data is found to be in agreement with the expectation from the Drell-Yan process. This is shown in Figure 5.12. No evidence for an extra neutral gauge boson (Z') is seen. However, it should be noted that the search performed is not yet sensitive to Z' masses that have not already been excluded. Plots of the A_{FB} vs invariant mass spectra for simulated samples with Z' bosons of varying masses are shown in Figure 5.19. As of the writing of this thesis, the ATLAS [21] and CMS [36] experiments have excluded the existence of a SSM Z' with mass less than approximately 1.9 TeV, and for Z' particles in E6 models the limits range from 1.4 to 1.6 TeV. As is seen in Figure 5.19, for Z' bosons of mass 1.5, 1.75 and 2 TeV, the deviation in A_{FB} is not observable below 1 TeV.

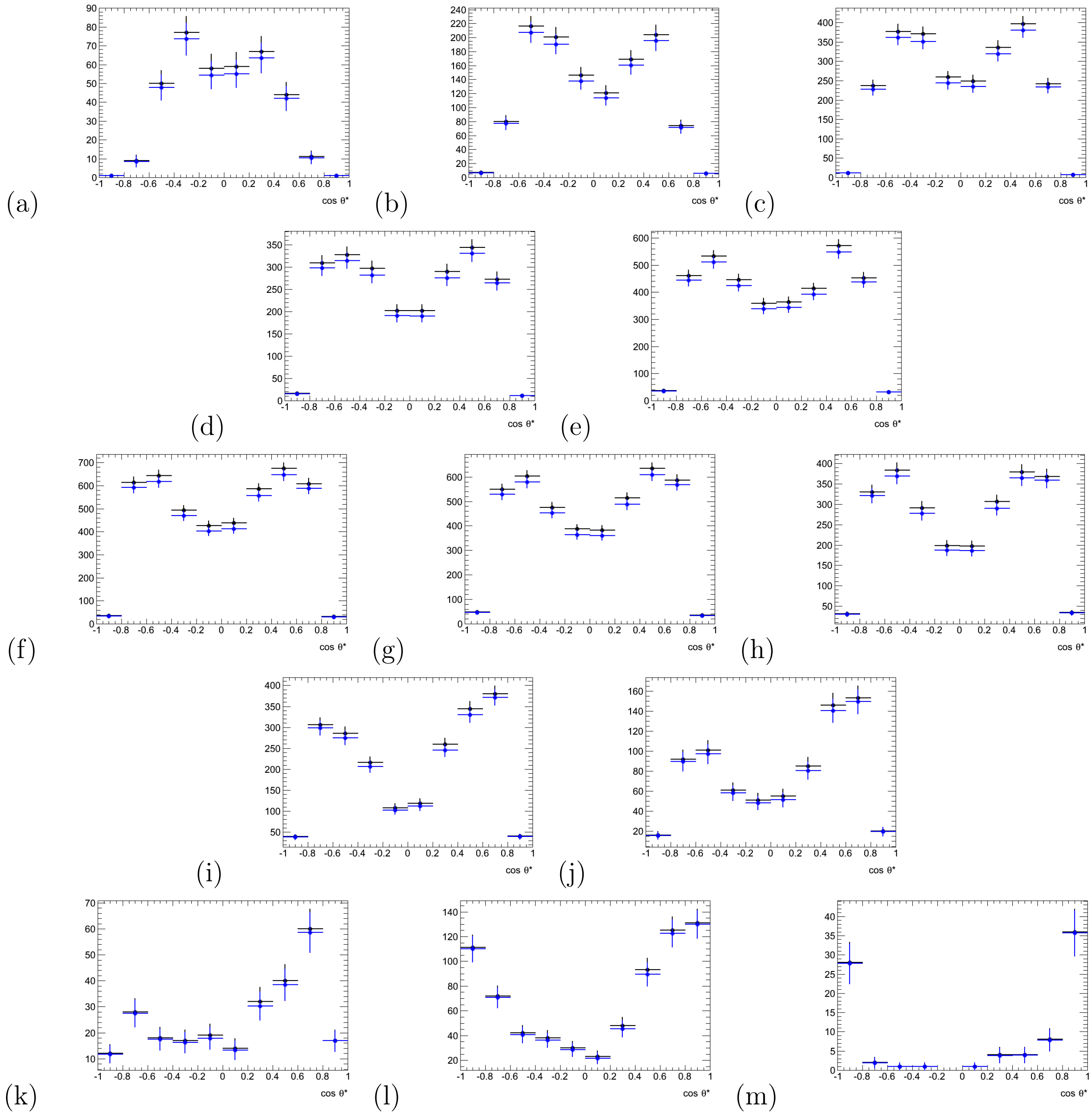

Figure 5.17. $\cos\theta^*$ distribution corrected using charge identification efficiencies (blue) and not corrected (black) in each invariant mass bin used for the measurement. The mass bins are, in GeV, (a) 60-70, (b) 70-80, (c) 80-85, (d) 85-87, (e) 87-89, (f) 89-91, (g) 91-93, (h) 93-95, (i) 95-100, (j) 100-110, (k) 110-120, (l) 120-250 and (m) 250-1000.

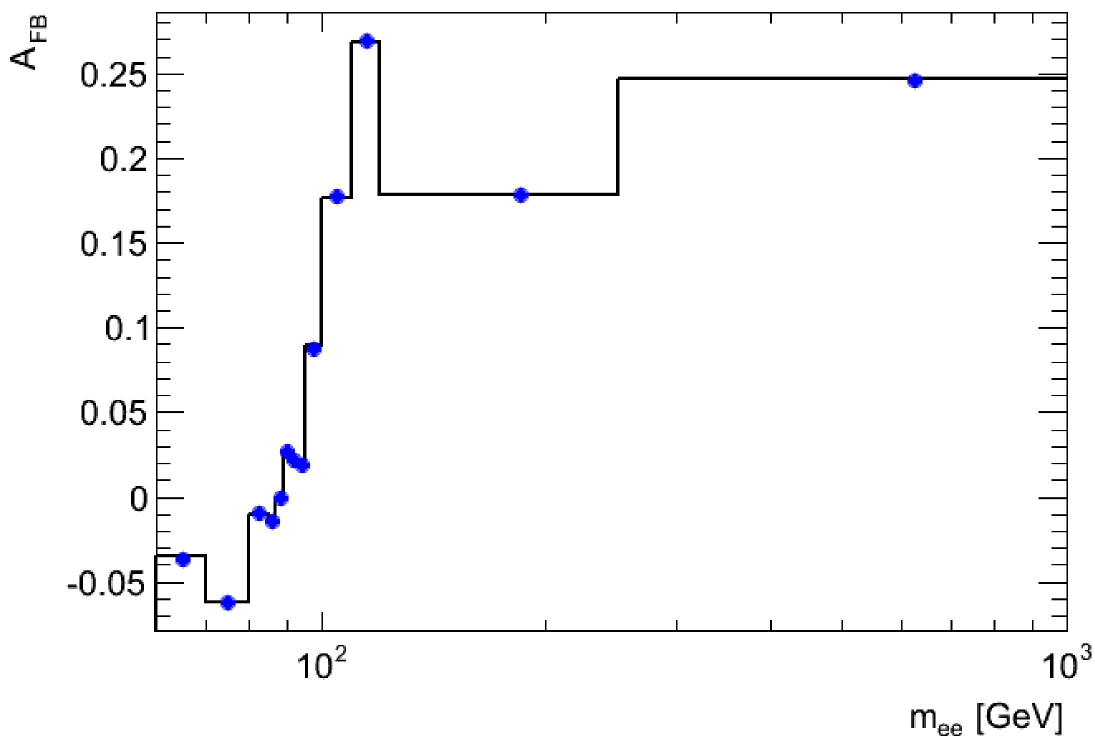

Figure 5.18. The difference is negligible between the A_{FB} distribution corrected for charge misidentification (blue points) and the uncorrected (black line) A_{FB}.

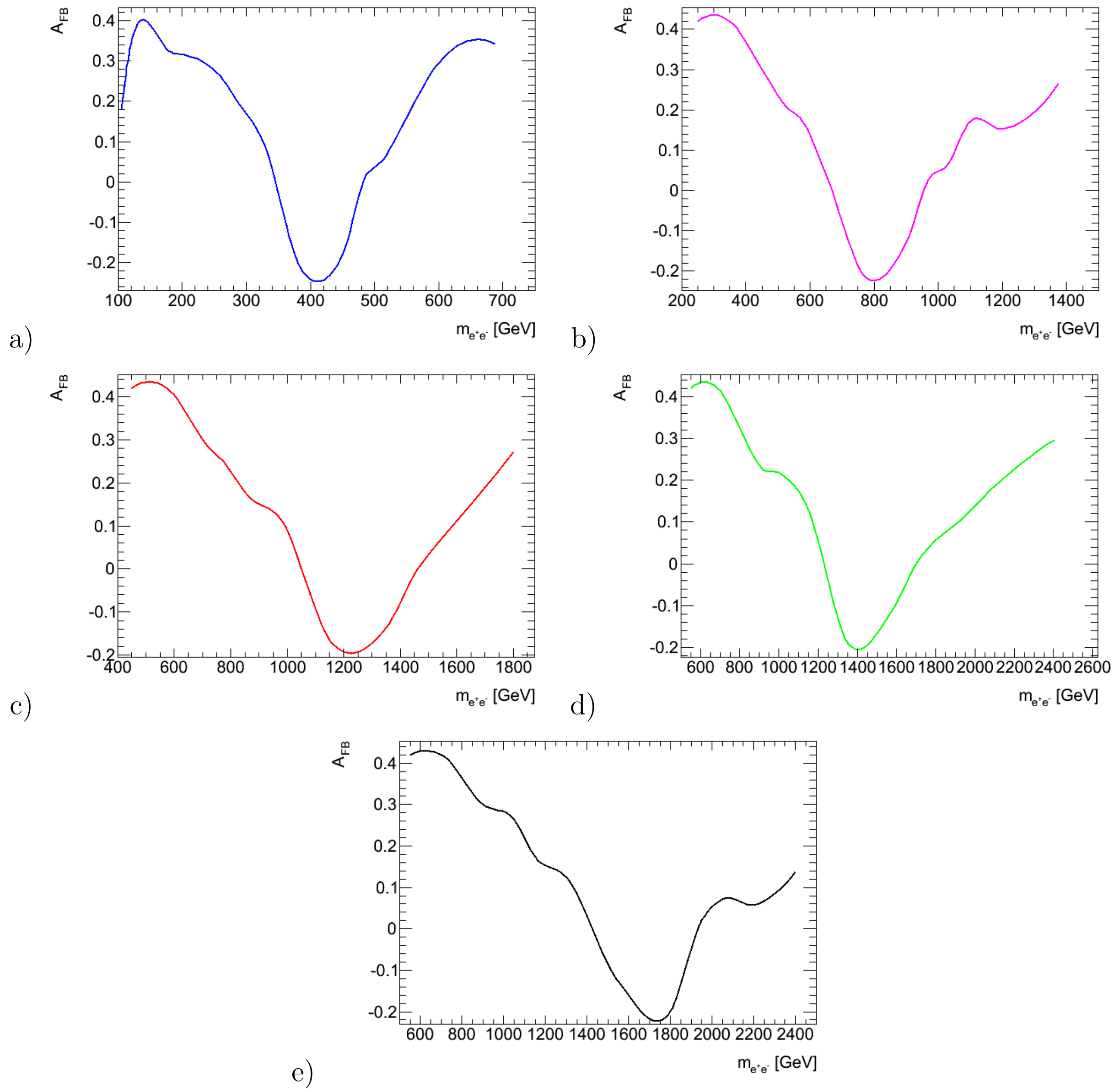

Figure 5.19. A_{FB} vs invariant mass for samples simulated with a SSM Z' having mass of a) 500 GeV, b) 1 TeV, c) 1.5 TeV, d) 1.75 TeV and e) 2 TeV. Before the Z' pole the value of A_{FB} is near the Standard Model expectation of Figure 5.12. This value is not equal to the theoretically expected 0.6 due to dilution of asymmetry occurrings when the wrong quark direction is selected. Consider the 2 TeV Z', which has not yet been excluded: the highest invariant mass events observed in this analysis are near 850 GeV. This corresponds to an A_{FB} value of approximately 0.35 in Figure 5.19e, which is well within the error bars of the Standard Model expectation. Therefore, the analysis in this thesis is not sensitive to the presence of a Z' having mass that has not already been excluded.

Appendix A

STUDY OF CONTAMINATION FROM W AND Z BOSONS IN THE PROMPT PHOTON FINAL STATE

If that turns out to be true, I'll quit physics.
On De Broglie's thesis on wave-particle duality

Max Von Laue (1879-1960)
German physicist, Nobel laureate

This chapter describes a data-driven method that was developed to determine the rate at which electrons from electroweak (EW) decays of W and Z bosons are misidentified as photons suitable for the measurement of the prompt photon cross section. The method relies on reconstruction of a Z boson in the ee and $e\gamma$ final states, where the γ arises from electron-photon misidentification. The result was used towards the calculation of photon purity [70] for use in the calculation of the prompt photon cross section using 880 nb^{-1} LHC collision data [20].

A.1. Electron and Photon Identification

Several Monte Carlo studies have demonstrated that electrons are occasionally reconstructed as photons. This is not entirely surprising, as the reconstruction of both electrons and photons begins with the identification of a cluster in the Liquid Argon (LAr) calorimeter. A cluster is a group of neighboring cells that is selected such that the cluster energy is maximized (known as the "sliding window" algorithm, see Chapter 3). For electrons and converted photons, which decay to an electron positron pair before entering the calorimeter, the cluster size is 5 $\times$ 5 cells. For unconverted photons the cluster size is 3×5 cells. The size of the cells which make up a cluster varies depending on the layer and the part of the calorimeter the cluster is located in. See Table A.1. For all particles, we attempt to locate a cluster in all layers of the calorimeter. However, less energetic particles may not deposit energy in all layers.

Table A.1. Cell size in the LAr calorimeter ($\Delta\eta \times \Delta\phi$).

$\|\eta\|$ range		Layer 1	Layer 2	Layer 3
0-1.475	Barrel	0.003×0.1	0.025×0.025	0.05×0.025
1.375-1.5	End-cap	0.025×0.1	|	|
1.5-1.8	End-cap	0.025×0.1	|	|
1.8-2.0	End-cap	0.003×0.1	|	|
2.0-2.5	End-cap	0.004×0.1	|	|
2.5-3.2	End-cap	0.006×0.1	|	|
1.375-2.5	End-cap	|	0.025×0.025	|
2.5-3.2	End-cap	|	0.1×0.1	|
1.5-2.5	End-cap	|	|	0.05×0.025

Once a cluster is located, it must be determined whether it belongs to an electron or a photon. This is accomplished via an understanding of whether or not there is a track associated with the cluster, and, if there is, an understanding of the track's properties.

To find associated tracks, the reconstruction software searches the $(\Delta\eta, \Delta\phi)$ region of $(0.05, 0.10)$ around the cluster's position in the second calorimeter layer. If a track is found in that area, the value of it's momentum, p, is checked to determine if $E/p < 10$ is satisfied, where E is the cluster's energy.

If no suitable track is located, the object is classified as an unconverted photon. Therefore, if an electron's track is of poor quality or is not found by the reconstruction software, the electron will be identified as a photon. Physical processes, such as Bremsstrahlung or photon conversions, can also make it more difficult to differentiate between electrons and photons.

The reconstruction software is designed to favor electrons in the case of electron-photon ambiguity. This has led to the creation of a photon recovery tool, which identifies such electrons and rebuilds photons from the eγ cluster level. This recovery tool is run in official reconstruction, for both real data and Monte Carlo production, since Athena version 15.5.0. Thus, there is some level of overlap between the electron and photon containers.

For some analyses, it may be desirable to remove this overlap by disregarding those electrons that correspond to recovered photons. This is easily done with data that are reconstructed after Athena version 15.6.6; in these later Athena versions, the barcodes of the recovered photon and the corresponding electron are the same. For Monte Carlo data sets reconstructed with earlier Athena releases, overlap removal can to some extent be accomplished using cluster matching, and track matching if track information is available. In this note, we will not use any overlap removal scheme.

A.2. Method to Measure e-γ Misidentification with LHC Collision Data

Due to the fact that there exists some level of ambiguity between electrons and photons, some number of Z$\rightarrow$ee events will be reconstructed as Z$\rightarrow$eγ. Because the frequency at which this occurs depends on the electron-photon fake rate, this rate can be extracted by examining the probability of reconstructing a Z $\rightarrow$ee event, which has a true ee final state, as ee or as $e\gamma$.

Before photon recovery is done, the probability of reconstructing the true ee event as ee is given by $\epsilon_1\epsilon_2$, where $\epsilon_{1(2)}$ is the efficiency associated with correctly identifying the first (second) electron used in ee invariant mass reconstruction.[1]

Therefore, the number of reconstructed ee events expected before recovery, $N(ee)_{before}$, is given by

$$N(ee)_{before} = \epsilon_1\epsilon_2 \; N(ee)_{true}, \tag{A.1}$$

where $N(ee)_{true}$ is the number of true Z→ee events with both electrons reconstructed within the acceptance region.

The probability of reconstructing the true ee event as $e\gamma$ is given by $2\epsilon_3\rho_E$, where ϵ_3 is the efficiency associated with reconstructing the electron used in $e\gamma$ invariant mass reconstruction and ρ_E is the probability of reconstructing an electron as a photon *before* photon recovery from the electron container is done. Thus, ρ_E represents the probability that an electron is identified *exclusively* as a photon. The factor of two arises from the fact that either electron can be misidentified.

Then, the number of reconstructed $e\gamma$ events we expect before photon recovery, $N(e\gamma)_{before}$, is given by

$$N(e\gamma)_{before} = 2\epsilon_3\rho_E \; N(ee)_{true}. \tag{A.2}$$

[1]In studies using the tag-and-probe method of electron efficiency measurement [12], it has been shown that ϵ is dependent on η, p_T and dielectron mass. Therefore, electron efficiencies are available as a matrix, in bins of these quantities, for various quality electrons. In this note, we use a value of ϵ that has been averaged over all bins.

During the photon recovery procedure, no additional ee events are obtained. The number of reconstructed ee events gained in the course of recovery, $N(ee)_{recov}$, is zero. This is because no electrons are actually removed from the electron container in this process. However, a non-zero number of additional $e\gamma$ pairs, $N(e\gamma)_{recov}$, is expected.

The probability that a reconstructed ee event will also be reconstructed as $e\gamma$ during photon recovery is: $P(ee \to e\gamma) = P(ee) \times 2P(e \xrightarrow[recovery]{} \gamma) = 2\epsilon_1\epsilon_2\rho_R$,[2] and so the number of additional $e\gamma$ events gained during photon recovery is

$$N(e\gamma)_{recov} = 2\epsilon_1\epsilon_2\rho_R N(ee)_{true}. \tag{A.3}$$

The total number of reconstructed $e\gamma$ pairs expected after recovery is then:

$$\begin{aligned} N(e\gamma)_{after} &= N(e\gamma)_{before} + N(e\gamma)_{recov} \\ &= 2\epsilon_3\rho_E N(ee)_{true} + 2\epsilon_1\epsilon_2\rho_R N(ee)_{true}. \end{aligned} \tag{A.4}$$

Now, let ρ be the overall e-γ fake rate, measured after recovery is done. Note that here ρ is the overall probability of the electron being reconstructed as a photon. Due to the electron-photon overlap described, ρ really consists of a combination of ρ_R, the probability that the electron is reconstructed as a photon during photon recovery (and is therefore also reconstructed as an electron), and ρ_E, the probability that the electron is exclusively reconstructed as a photon.

[2] Note that we do not account for the probability that one of the electrons is *not* recovered, $(1 - \rho_R)$, where ρ_R is the probability for an electron to simultaneously be (mis)reconstructed as a photon. This is due to the overlap mentioned earlier; the fact that an electron is reconstructed as a photon does not preclude it from being reconstructed as an electron, and regardless of whether a photon is recovered from it or not, an electron before recovery remains in the electron container after.

In this case, we also have

$$N(e\gamma)_{after} = 2\epsilon_3 \rho N(ee)_{true}, \tag{A.5}$$

which, together with (A.4), yields:

$$\rho = \rho_E + \frac{\epsilon_1 \epsilon_2}{\epsilon_3} \rho_R. \tag{A.6}$$

In addition to writing ρ in terms of ρ_E and ρ_R, we can write it in terms of the number of ee and $e\gamma$ reconstructed events obtained after photon recovery. This is done by combining (A.5) and (A.1), keeping in mind that $N(ee)_{before} = N(ee)_{after}$. Hence,

$$\rho = \frac{\epsilon_1 \epsilon_2}{2\epsilon_3} \frac{N(e\gamma)_{after}}{N(ee)_{after}}. \tag{A.7}$$

Using (A.7) the value of ρ can be measured in data.

Following the same logic, ρ_E can also be written in terms of the number of reconstructed $e\gamma$ and ee events. Using (A.2) and (A.1) we obtain

$$\rho_E = \frac{\epsilon_1 \epsilon_2}{2\epsilon_3} \frac{N(e\gamma)_{before}}{N(ee)_{before}}. \tag{A.8}$$

The value of ρ_E can be measured in data by not considering recovered photons in the mass reconstruction. As both ρ and ρ_E can be measured in data, the value of ρ_R can then be calculated.

A.3. Calculation of the fake rate ρ, on MC simulated data

To understand the likelihood of observing an $e\gamma$ invariant mass peak from misidentified Z→ee, we have conducted a feasibility study using fully simulated and reconstructed Monte Carlo data, generated with $\sqrt{s}$ =7 TeV.

Table A.2. Monte Carlo data samples used.

Process	Dataset ID	Generators	Generator Cuts	Number of events
$Z \to ee$	106046	Tauola, Photos, PYTHIA	$\|\eta_e\| < 2.8$ $M_{ee} > 60$ GeV	4.75 million
$\gamma\gamma$	105964	Photos, PYTHIA	$\|\eta_\gamma\| < 2.7$ $p_{T_\gamma} > 15$ GeV	100000
γ+jet	108087	PYTHIA	$\|\eta_\gamma\| < 2.7$ $p_{T_\gamma} > 17$ GeV $p_{T_{jet}} > 15$ GeV	5 million
jj	105802	PYTHIA	$\|\eta_{jet}\| < 2.7$ $p_{T_{jet}} > 17$ GeV	10 million

To reconstruct ee and eγ invariant masses, we run on officially produced D3PDs of the samples listed above.[3] All electron and photon container objects used in the invariant mass reconstruction were required to conform to the cuts listed in Table A.3. For each event, we attempt to reconstruct an ee and an $e\gamma$ invariant mass; in the case of events with multiple electron and photons, the ee mass made from the highest two p_T electrons and the $e\gamma$ mass made from the highest p_T electron and highest p_T photon are taken. After analysis cuts, ee and $e\gamma$ mass distributions from the dijet sample had too low statistics to be used. Therefore, we reconstruct the dijet, jj, invariant mass for this sample. The dijet background to $e\gamma$ final states was obtained

[3]For the Monte Carlo analysis, we have not required that objects pass any event selection trigger. When using this method in data, use of a photon trigger will be necessary, as opposed to the electron trigger used for the standard Z→ee analysis. We will likely use the 2g20_loose trigger.

by using the shape of the jj distribution and scaling it using e-jet rejection factor of .0146% [54] [59] and a γ-jet rejection factor of .0167% [85]. True Z$\rightarrow$ee events have been removed from the dijet sample.

Table A.3. Selection cuts imposed on electron, photon and jet candidates.

Final State	Particle ID Criteria	Kinematic Cuts
eγ	e passes ElectronTight[4]	$\lvert\eta\rvert < 2.4$
	γ passes PhotonTight[4]	$1.37 < \lvert\eta\rvert < 1.52$ excluded
		$p_T > 20$ GeV
jj	2 highest p_T jets selected	$\lvert\eta\rvert < 2.4$
		$1.37 < \lvert\eta\rvert < 1.52$ excluded
all		Mass > 5 GeV

The combined signal and background for the $e\gamma$ final state, normalized to 1 pb^{-1} integrated luminosity, is shown in Figure A.1.[4]

[4]In this note we show plots and a fake rate that has been measured using tight quality electrons. In general, any combination of electron qualities may be used with the appropriate value of ϵ in (A.7) (See Table A.4). In this note we take the values $\epsilon_{tight} = 0.7152$, $\epsilon_{medium} = 0.8997$ and $\epsilon_{loose} = 0.9430$ [41].

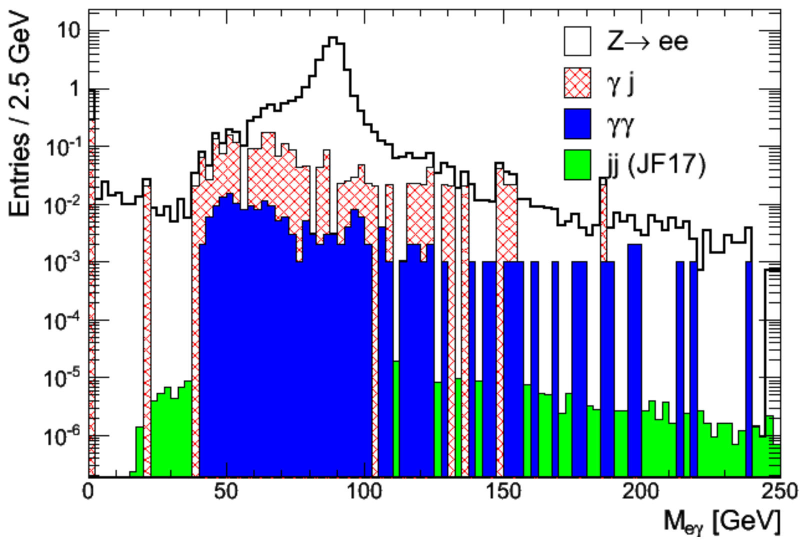

Figure A.1. Signal and background for eγ final state in the Monte Carlo study, normalized to 1 pb^{-1}. The eγ peak from $Z \rightarrow ee$ misidentification is clearly visible above γ+jet (hatched), $\gamma\gamma$ (blue) and jj backgrounds (green).

The combined background is minimal, especially in the signal region. At 1 pb^{-1}, approximately 30 $e\gamma$ events from ee misidentification are expected. The signal region is shown in Figure A.2 using linear scale, to demonstrate more precisely the expected shape of the $e\gamma$ distribution from electron misidentification.

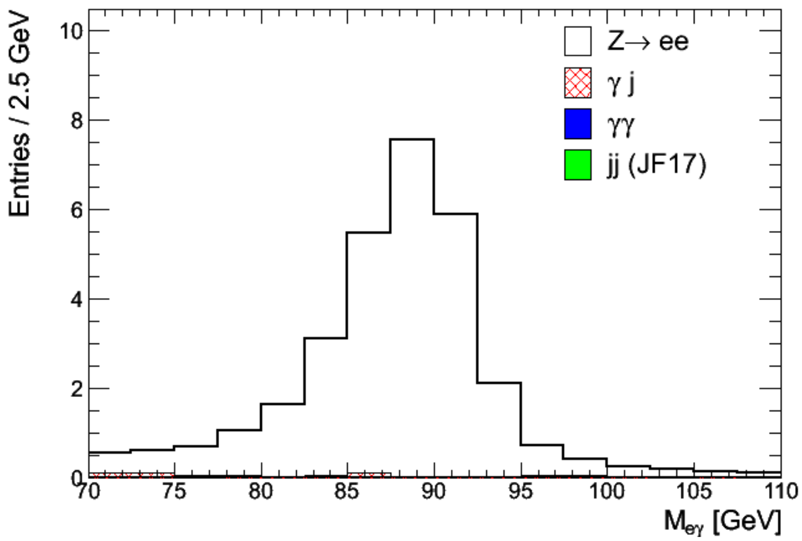

Figure A.2. Signal and background for eγ final state in the Monte Carlo study, with focus on the signal region between 70 and 110 GeV. Only a small amount of the γj background is visible in linear scale; other backgrounds are not visible at all. Approximately 30 $e\gamma$ events are expected with 1 pb^{-1} of data.

Based on the results of this feasibility study, it should be possible to identify a peak in the $e\gamma$ final state arising from misidentification of one electron in Z→ee events.

A.3.1. Extraction of number of $e\gamma$ events

To calculate the e-γ fake rate it is necessary to obtain the number of events in the signal peak shown in Figure A.1. We first perform a maximum likelihood fit to the signal (Figure A.3) and background (Figure A.4) separately.

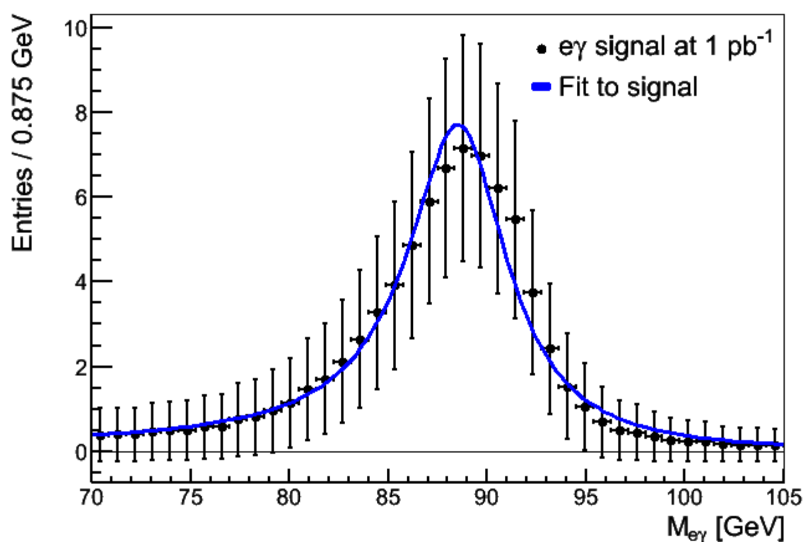

Figure A.3. Maximum likelihood fit to the signal, eγ from $Z \to ee$ misidentification, normalized to 1 pb^{-1} integrated luminosity.

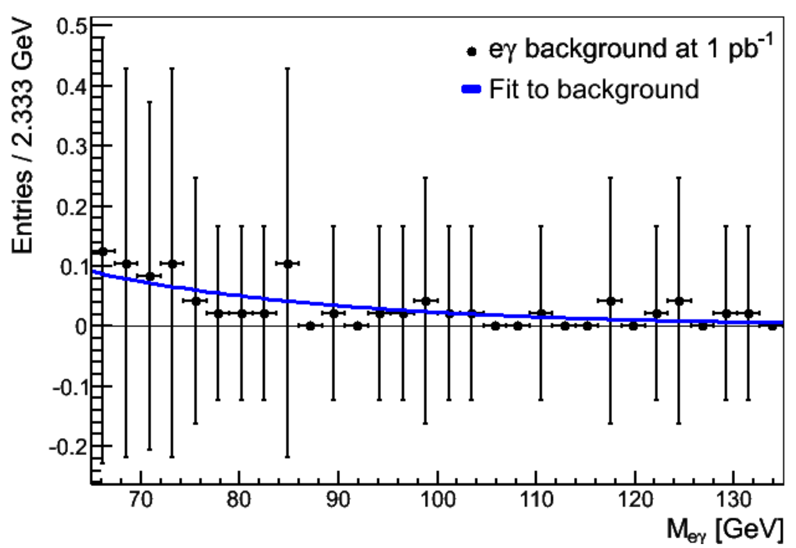

Figure A.4. Maximum likelihood fit to the background in the eγ final state, normalized to 1 pb^{-1} integrated luminosity.

Parameter values for the signal and background probability distribution functions are extracted from these fits. Using these parameters, a final maximum likelihood fit is done to the combined signal and background distribution (Figure A.5). The number of eγ events in the signal peak is returned as a parameter of this fit.

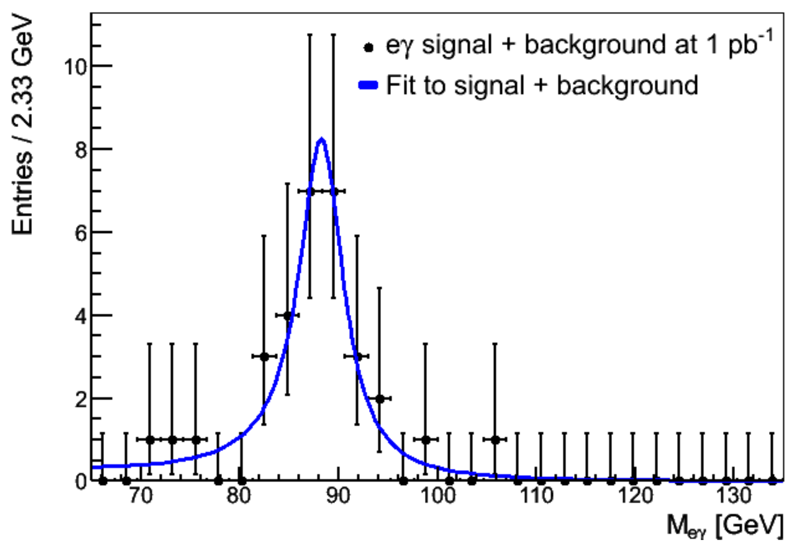

Figure A.5. Maximum likelihood fit to combined signal and background in the eγ final state, normalized to 1 pb^{-1} integrated luminosity.

The final item needed to evaluate (A.7) is the number of signal events in the ee final state. This number can be found in the same way as the number of $e\gamma$ events was found.

A.3.2. Values of ρ using different combinations of electron quality

We have obtained results for the electron-tight quality photon fake rate present in the most recent production of Monte Carlo data by counting the number of ee and $e\gamma$ invariant masses reconstructed and normalized to 1 pb^{-1}. This has been done using (A.7), and results have been obtained for different combinations of electron quality as shown in Table A.4. For the case where all tight quality electrons are used, this yields a fake rate of $(6.2 \pm 1.4)\%$.

Table A.4. e-γ fake rate, ρ, measured using different electron quality combinations for the ee and $e\gamma$ reconstructed masses. All errors shown are statistical and correspond to an integrated luminosity of 1 pb^{-1}. The first column shows the set of cuts applied to the leading (e_{lead}) and subleading (e_{sub}) electrons used for the dielectron mass. The second of column shows misidentification rates calculated using tight cuts ('T') on both the electron and photon in the eγ mass, the third column uses medium ('M') cuts on the electron and tight for the photon and the fourth column uses loose ('L') cuts on the electron and tight for the photon.

		el	γ	el	γ	el	γ
e_{lead}	e_{sub}	T	T	M	T	L	T
T	T	6.2±1.4%		5.2±1.2%		6.1±1.0%	
T	M	6.1±1.3%		5.1±1.1%		5.9±1.0%	
M	T	6.3±1.4%		5.3±1.2%		6.2±1.0%	
M	M	5.6±1.2%		4.7±1.1%		5.5±0.9%	
M	L	6.2±1.4%		5.2±1.1%		6.0±1.0%	
L	M	6.2±1.4%		5.3±1.2%		6.1±1.0%	
L	L	6.2±1.4%		5.2±1.2%		6.1±1.0%	

A.3.3. Systematic uncertainties on ρ

The systematic uncertainties on the measurements of $N(ee)$, $N(e\gamma)$ and the electron reconstruction efficiencies, ϵ_1, ϵ_2 and ϵ_3 all contribute to the uncertainty on the measurement of the fake rate, ρ. Specifically, if the efficiencies used in the calculation of ρ are those measured in data via the tag-and-probe method [80], the systematic error on the electron efficiency is correlated with the error on the measurement of ρ. Some expected sources of systematic error on ρ include: effect of electron energy scale, uncertainty of electron identification, the effect of distorted material and the use of object-quality maps to remove objects in the region of dead OTX modules. These are well documented in [15] and [17]. A systematic effect due to the presence of dead pixel modules is discussed in Section A.3.6, although the uncertainty has not been quantified. Additionally, systematics associated with the maximum likelihood fitting procedure will be present, such as the effect of an uncertainty on electron/photon energy resolution on the resolution of the ee and $e\gamma$ peaks observed. Systematics associated with aspects of the fit are described in [73] and in Section 5.5 of [68].

A.3.4. Fake rate in bins of η and p_T

The values of ρ, as measured from Z→ee using the method of this note, are shown in Figure A.6 in bins of η and p_T. The results shown are for masses reconstructed using tight electrons only. In the following plots, the entire Monte Carlo dataset of 4.75 million unfiltered Z→ee events is used, which corresponds to an integrated luminosity of 5.56 fb^{-1}.

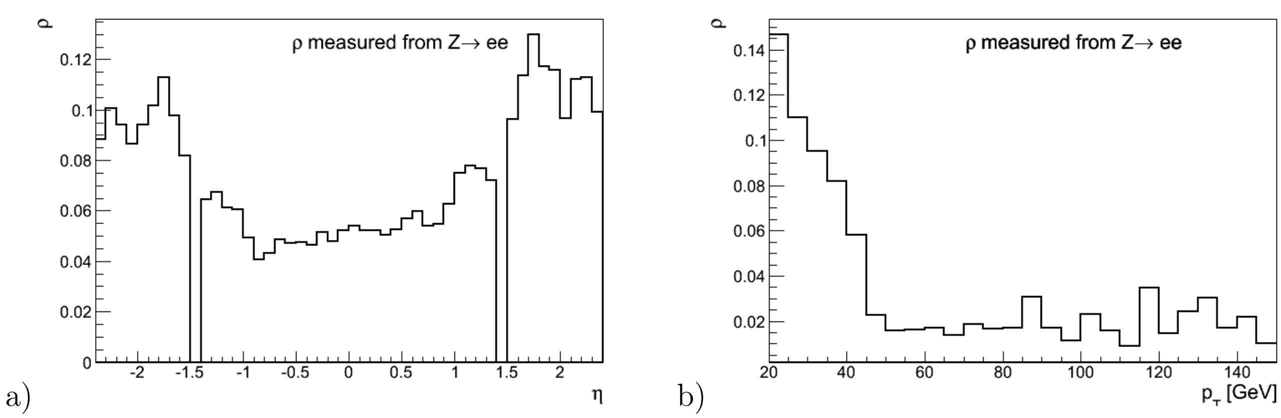

Figure A.6. The electron-photon fake rate, ρ, in bins of a) η, and b) p_T. The entire Monte Carlo dataset of 4.75 million unfiltered Z→ee events is used, corresponding to an integrated luminosity of 5.56 fb^{-1}.

The high fake rate observed in bins of low p_T can be somewhat ameliorated by the use of a higher invariant mass cut, as shown in Figure A.7. The effect is significant for lower p_T objects, but for higher p_T objects the use of an invariant mass cut has little impact on the fake rate ρ.

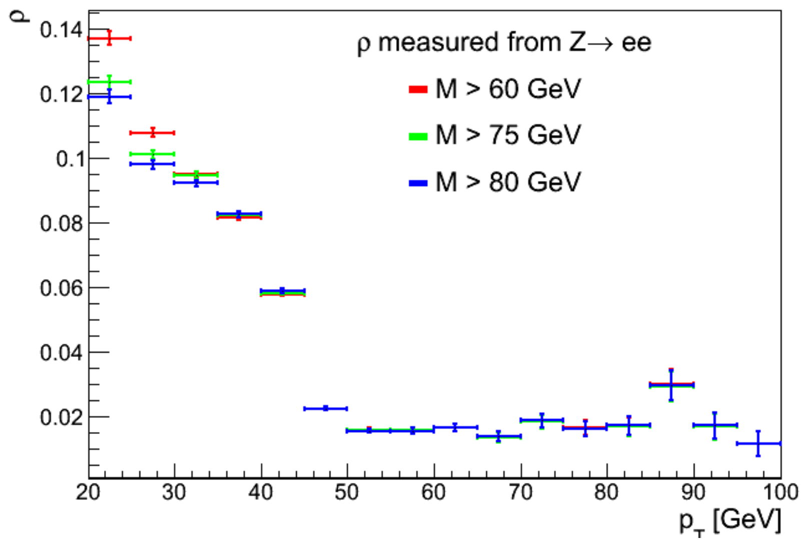

Figure A.7. The electron-photon fake rate, ρ, in bins of p_T. The entire Monte Carlo dataset of 4.75 million unfiltered Z→ee events is used, corresponding to an integrated luminosity of 5.56 fb^{-1}. In red, an invariant mass minimum of 60 GeV is implemented; in green, 75 GeV; in blue, 80 GeV. The use of a high invariant mass cut leads to a significant lowering of the value of ρ in lower p_T bins, but the effect is minimal for higher p_T objects.

A.3.4.1. Comparison to fake rate from truth (information at the generator level)

A comparison to the true value of ρ has been made, with the true value computed using (A.9) below:

$$\rho_{true} = \frac{\gamma_{tight}}{e_{true}^{MotherZ}}, \tag{A.9}$$

where γ_{tight} is the number of reconstructed tight photons matching to true electrons from Z→ee decay and $e_{true}^{MotherZ}$ is the number of true electrons known to have originated from a Z boson. Both the reconstructed photons and the true electrons are required to be within the η and p_T acceptance specified in Table A.3. Using (A.9) we find that ρ_{true} =6.5%.

Figure A.8 shows this value in bins of η and p_T, and Figure A.9 shows the values of ρ_{true} with $\rho_{measured}$ superimposed.

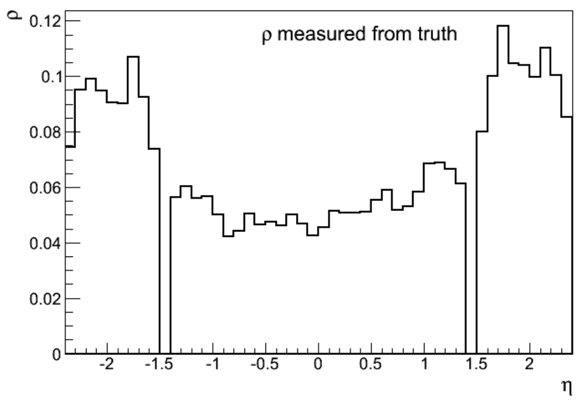

a)

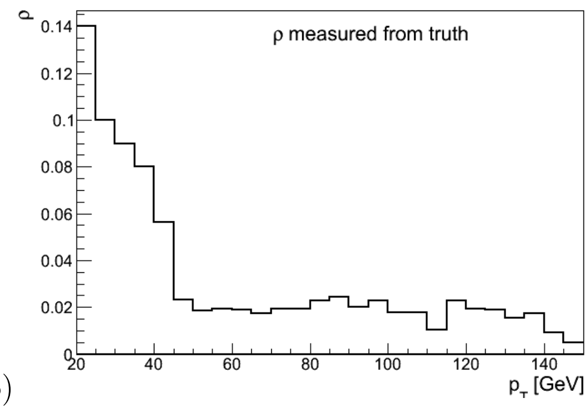

b)

Figure A.8. The electron-photon fake rate, ρ, as measured in truth, in bins of a) η and b) p_T. The entire Monte Carlo dataset of 4.75 million unfiltered Z→ee events is used, corresponding to an integrated luminosity of 5.56 fb^{-1}.

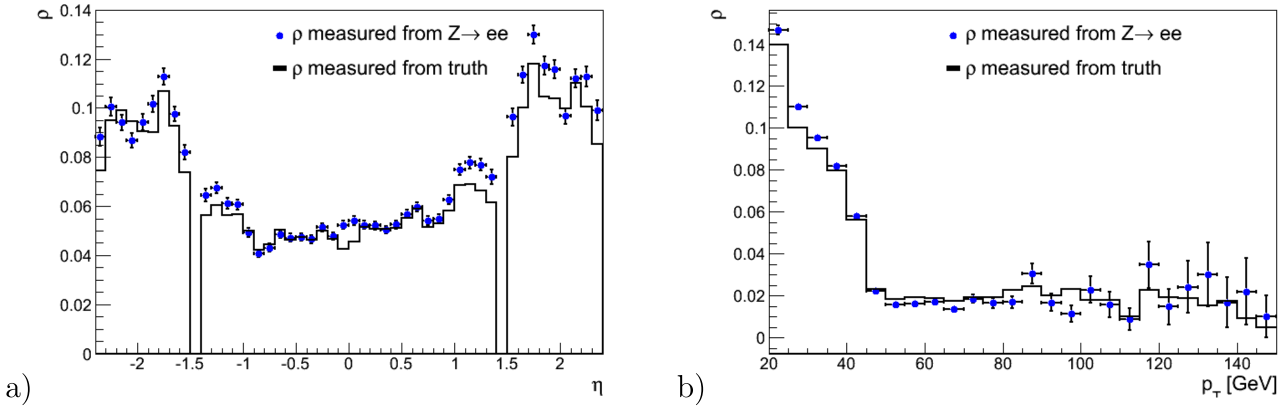

Figure A.9. The electron-photon fake rate, ρ, in bins of a) η and b) p_T. Measurements using the data-driven method described in this note are shown in blue, while truth measurements are shown in black. The entire Monte Carlo dataset of 4.75 million unfiltered Z→ee events is used, corresponding to an integrated luminosity of 5.56 fb^{-1}.

There is good agreement between $\rho_{measured}$ and ρ_{true} for both η and p_T distributions. The asymmetry in η, present in both the truth and measured distributions of ρ, will be discussed in Section A.3.6. The high measured fake rate in lower p_T bins is due to the presence of a low-mass tail arising primarily from low p_T photons from bremsstrahlung (see Figure A.10).

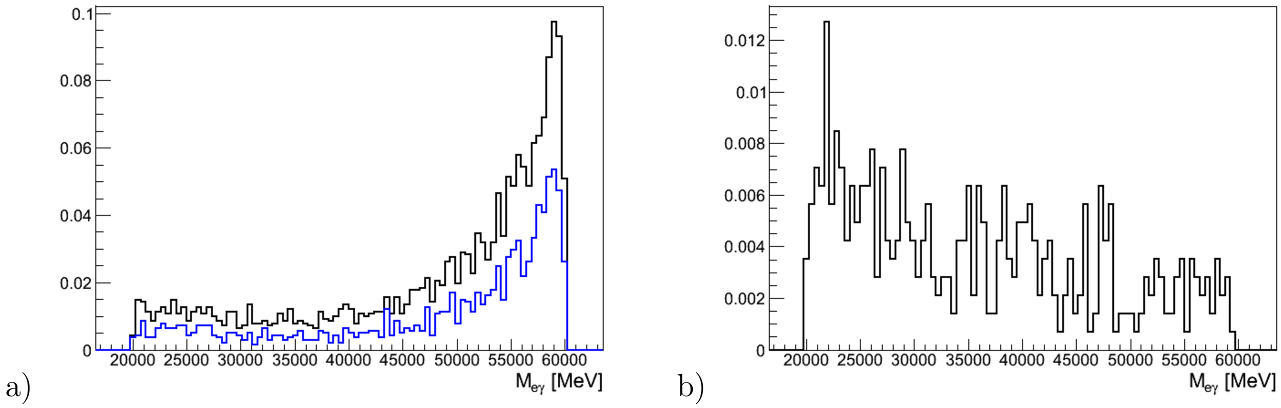

Figure A.10. The low-mass tail ($M_{e\gamma} < 60$ GeV) in the $e\gamma$ final state, normalized to 1 pb^{-1} integrated luminosity. a) In black, contributions to the $e\gamma$ tail with the photon having $p_T < 40$ GeV. In blue, the portion of this contribution that arises from photons from bremsstrahlung. b) In black, contributions to the $e\gamma$ tail with the photon having $p_T > 40$ GeV. Contribution from bremsstrahlung is negligible and not shown.

A.3.5. Measurement of ρ_E and calculation of ρ_R

As was mentioned in Section A.2, it is possible to measure the rate at which electrons are *exclusively* reconstructed as photons, ρ_E, by disregarding those photons from photon recovery. In all other respects, the same procedure as outlined in the previous sections of this note is followed. In Table A.5 we present measurements of ρ_E using different qualities of electrons (tight photons are always used). Figure A.11 depicts the values of ρ_E in bins of η and p_T; in this case, tight electrons are used. Figure A.12 shows the true values of ρ_E binned in η and p_T, and Figure A.13 shows a comparison between the true and measured values.

Table A.5. e-γ fake rate, ρ_E, measured using different electron quality combinations for the ee and $e\gamma$ reconstructed masses. Recovered photons are not used. All errors are statistical and correspond to an integrated luminosity of 1 pb^{-1}. This table reflects the measurement of exclusive misidentification, as opposed to Table A.4, which shows total misidentification.

		el	γ	el	γ	el	γ
e_{lead}	e_{sub}	T	T	M	T	L	T
T	T	1.3±0.7%		1.6±0.5%		1.1±0.5%	
T	M	1.3±0.6%		1.5±0.5%		1.1±0.4%	
M	T	1.3±0.7%		1.6±0.5%		1.1±0.5%	
M	M	1.2±0.6%		1.4±0.5%		1.0±0.4%	
M	L	1.3±0.7%		1.6±0.5%		1.1±0.5%	
L	M	1.3±0.7%		1.6±0.5%		1.1±0.5%	
L	L	1.3±0.7%		1.6±0.5%		1.1±0.5%	

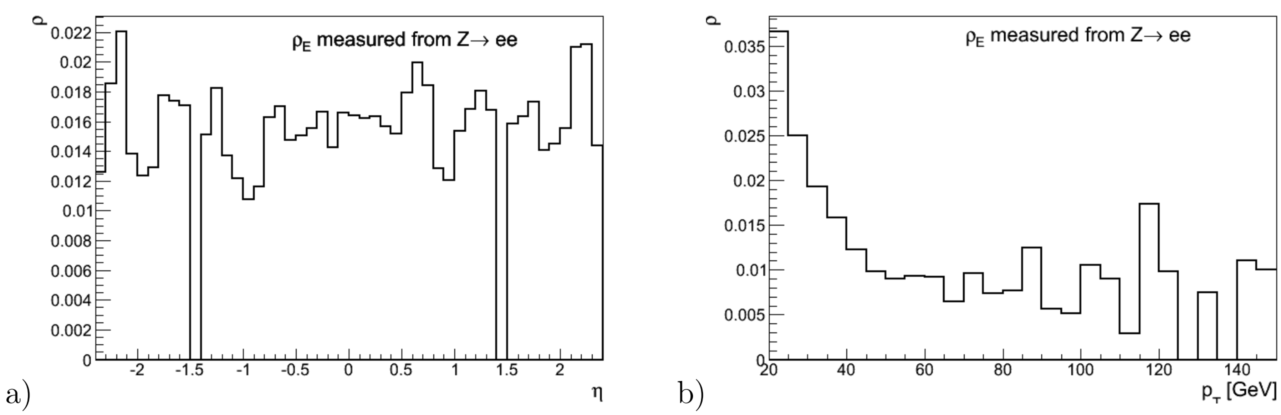

Figure A.11. The rate at which electrons are identified exclusively as photons, ρ_E, as measured using the data-driven method described in this note, in bins of a) η and b) p_T. The entire Monte Carlo dataset of 4.75 million unfiltered Z→ee events is used, corresponding to an integrated luminosity of 5.56 fb^{-1}.

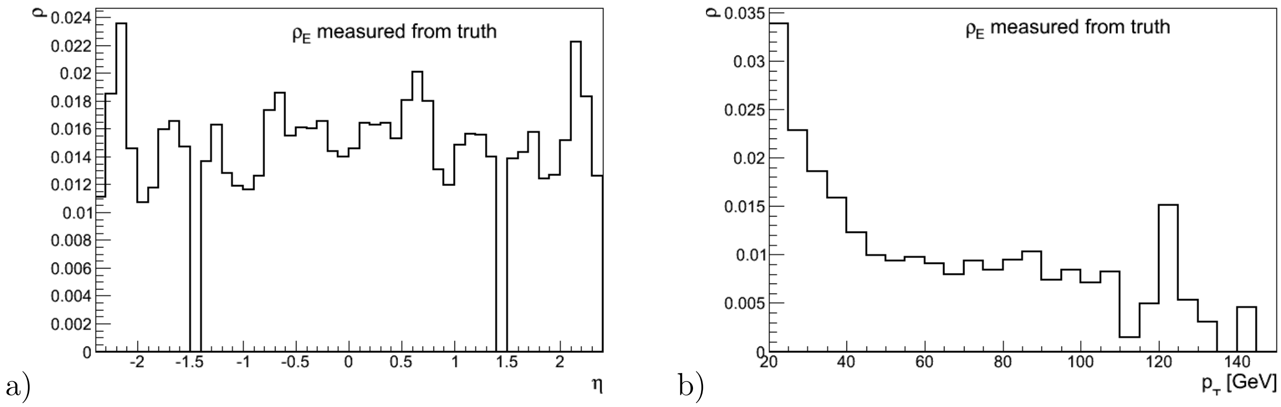

Figure A.12. The rate at which electrons are identified exclusively as photons, ρ_E, as measured using Monte Carlo truth information, in bins of a) η and b) p_T. The entire Monte Carlo dataset of 4.75 million unfiltered Z→ee events is used, corresponding to an integrated luminosity of 5.56 fb^{-1}.

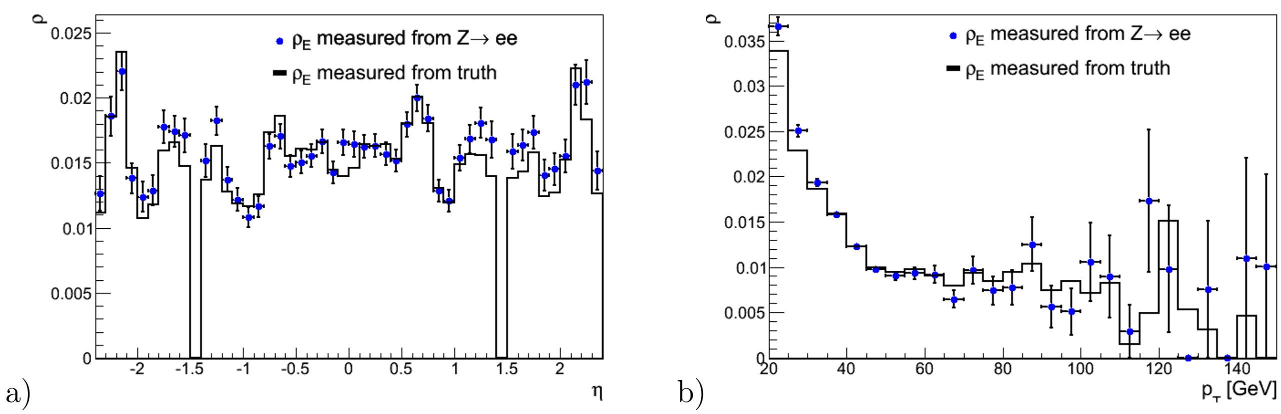

Figure A.13. A comparison between the value of ρ_E obtained via the data-driven method, shown in blue, and the truth value, shown in black. The entire Monte Carlo dataset of 4.75 million unfiltered Z→ee events is used, corresponding to an integrated luminosity of 5.56 fb^{-1}.

We have also calculated the fake rate arising from photon recovery, ρ_R, using (A.6) using these measurements for ρ and ρ_E. Using values of ρ and ρ_E averaged in η and

p_T which have been obtained using only tight electrons, we calculate ρ_R =6.8±1.6%.

A.3.6. Dependence of ρ and ρ_E on the presence of dead pixel modules

As was seen in the previous section, the fake rate ρ is not symmetric in η. This is directly due to the fact that the majority of the fakes are converted photons. For the case when a tight electron is used, the percentage of photons in the $e\gamma$ mass arising from conversions is 72%. The fraction of these that are double-track conversions is 54%, while the fraction of these that are single-track conversions is 46%.

The identification of converted photons is highly dependent on the presence of dead modules in the b-layer of the inner detector tracking system. Single-track photons are defined as those electromagnetic objects associated with one track having no b-layer hits. The track's first inner detector hit is taken to be the conversion vertex. [29] In the case that there is at least one b-layer hit on the track, the object will be reconstructed as an electron. Double-track objects associated with a conversion vertex are taken to be converted photons if each track has a b-layer hit, or if neither track does. If only one of the two tracks has a b-layer hit, the object is classified as an electron. [37]

Thus, if an electron's track is reconstructed in the (η, ϕ) region of a dead b-layer (pixel) module, it may be mistakenly classified as a converted photon. Therefore, a higher e-γ fake rate is expected in the location of dead b-layer modules. Since many of the converted photons arise from photon recovery, we also expect greater geometric dependence in the measurement of ρ than in ρ_E.

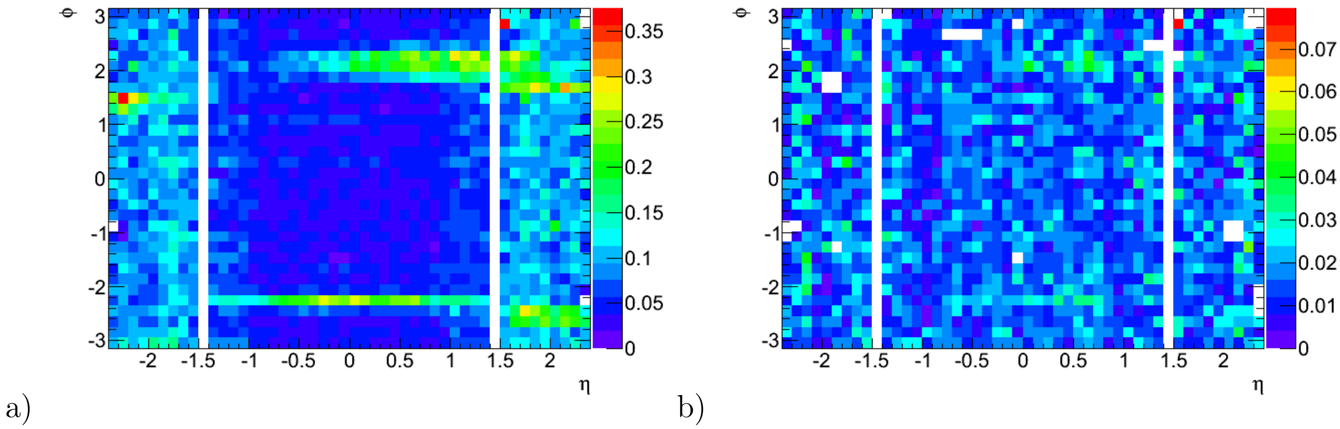

Figure A.14. a) The dependence of ρ as a function of η vs. ϕ. The regions with high values of ρ overlap with regions of the tracking system that have dead b-layer modules, b-layer modules with many dead pixels or are neighbors to such modules. b) The dependence of ρ_E as a function of η vs. ϕ. The dead or partially dead regions of the tracking system are not as apparent, although some effect can be seen. The full Z→ee Monte Carlo dataset, corresponding to 5.56 fb^{-1}, was used.

As is seen in Figure A.14, which shows the dependence of ρ as a function of η vs. ϕ, there is in fact a higher fake rate in the regions where dead b-layer modules are present; the effect is also seen in some regions near such modules. However, for ρ_E, as is expected, a very low degree of asymmetry in η and ϕ is observed. The geometric dependence of ρ depicted in Figure A.14 of course reflects the hardware conditions used to simulate the specific Monte Carlo sample. For a future measurement using data, the distribution may be different, although a dependence on the location of dead pixel modules is still expected.

A.3.7. Conclusion of MC study

We have developed a data-driven method for measuring the rate at which high p_T electrons are misidentified as high p_T, tight quality photons with the current ATLAS reconstruction software. We have measured this value to be $\rho = (6.2 \pm 1.4\%)$ in the current Monte Carlo production. An understanding of this specific misidentification is important, as good quality, high p_T photons are those commonly selected for many physics analyses, such as the $H \to \gamma\gamma$ analysis.

We have also isolated and measured the portion of the fake rate that occurs due to exclusive misidentification of electrons as photons, ρ_E, and have subsequently calculated ρ_R, the portion of the fake rate arising from photon recovery from the electron container. For a measurement made with 1 pb^{-1} integrated luminosity, and using only tight electrons, the values found in Monte Carlo are $\rho_E = 1.3{\pm}0.7\%$ and $\rho_R = 6.8{\pm}1.6\%$.

A.4. Measurement with LHC collision data and use in calculating photon impurity

The electron contribution to photon impurity can be calculated by (A.10):

$$I = \frac{L \cdot \sigma_e \cdot \rho}{N_\gamma} \tag{A.10}$$

where L is the integrated luminosity, σ_e is the prompt electron cross section, N_γ is the number of objects reconstructed as photons passing analysis cuts, and ρ is the electron-to-photon fake rate.

All parameters required to evaluate (A.10) can be taken from data, with the exception of σ_e. For this, the effective cross section ($\sigma_e \times \epsilon_F$) of the Pythia JF17 [5] sample is used. To estimate the cross section of electrons from hadronic processes, the Pythia cross section is scaled by the fraction of events having a true electron from hadronic decay with $p_{\mathrm{T,true}} > 20$ GeV and $|\eta_{\mathrm{true}}| <2.37$ (excluding $1.37< |\eta_{\mathrm{true}}| <1.52$). To estimate the cross section of electrons from electroweak sources, the same procedure is employed, but requiring that the electron originate from the decay of a W, Z or

τ. The final values of the electron contributions for both hadronic and electroweak processes are given in Table A.6.

Table A.6. MC based estimate of prompt electron cross section and input parameters. The cross section and filter efficiency are the average values listed at [5]. Errors on these values are estimated by subtracting the smallest value listed from the largest and dividing by two. Error on the fraction of events in the sample with high p_T electrons is statistical.

JF17 cross section	$(1147 \pm 9) \times 10^6$ pb
JF17 filter efficiency	(0.085 ± 0.004)
Fraction of JF17 events with >=1 truth electron: electron is from hadronic decay, $p_{T_{true}} > 20$ GeV, $\|\eta_{true}\| <2.37$ (less $1.37< \|\eta_{true}\| <1.52$)	$(305 \pm 6) \times 10^{-6}$
Fraction of JF17 events with >=1 truth electron: electron is from EW decay, $p_{T_{true}} > 20$ GeV, $\|\eta_{true}\| <2.37$ (less $1.37< \|\eta_{true}\| <1.52$)	$(37 \pm 2) \times 10^{-6}$
$\sigma_{e_{had}}$	$(30 \pm 1) \times 10^3$ pb
$\sigma_{e_{EW}}$	$(3.6 \pm 0.3) \times 10^3$ pb

The method to calculate ρ is outlined in the previous section. It consists of counting the number of ee and $e\gamma$ pairs reconstructed with an invariant mass in the Z mass region, where the γ in the $e\gamma$ pair is assumed to arise from misidentification of one electron in $Z \to ee$ decay. The fake rate is given by (A.11):

$$\rho = \frac{\epsilon_1 \epsilon_2}{2\epsilon_3} \frac{N(e\gamma)}{N(ee)} \tag{A.11}$$

where ϵ_1 and ϵ_2 are the efficiencies associated with reconstructing the electrons used to build the ee pair, ϵ_3 is the efficiency of reconstructing the electron used in the $e\gamma$

pair, and $N(ee)$ and $N(e\gamma)$ are the numbers of reconstructed ee and $e\gamma$ pairs. In principle, the efficiencies used in (A.11) can be binned in p_T and η. However, here the average values cited in [40] is used.

The analysis is carried out on the same data set used for the prompt photon cross section paper, applying the same Good Run List (GRL), trigger and vertex requirements. For 880 nb^{-1}, in the mass range 66-116 GeV, 156 ee pairs and 38 $e\gamma$ pairs are found. A complete list of the cuts applied to the electron and the photon are listed in Table A.7. Invariant mass plots for the ee and $e\gamma$ final states are shown in Figure A.15. Comparison is made with the unfiltered $Z \to ee$ sample, which has a luminosity of 5.2 fb^{-1}.

Table A.7. Object level cuts for the electron-photon fake rate analysis are listed here. One eγ invariant mass pair per event is made, using the highest p_T electron and photon that pass the cuts.

e/γ is within $\|\eta\|$ <2.37, excluding 1.37< $\|\eta\|$ <1.52
e/γ has $p_{T_{clus}}$ >20 GeV
e/γ passes object quality cuts
e passes robuster electron tight isEM quality cut
γ passes robust photon tight isEM quality cut
Photon passes isolation cut

These numbers, applied to equation (A.11), yield a fake rate $\rho = (8.4 \pm_{stat} 1.6 \pm_{syst} 1.1)\%$. The value of ρ, as measured on the $Z \to ee$ Monte Carlo sample, is $(7.1 \pm_{stat} 1.6 \pm_{syst} 0.2)\%$. The systematic errors arise from a 3.4% relative error on the electron efficiency, as measured on 7.7 pb^{-1} in [40] (used for both data and MC). For the data measurement, an additional systematic error of 13.1% is considered, as the 5 background events predicted by Monte Carlo amount to the 13.1% of

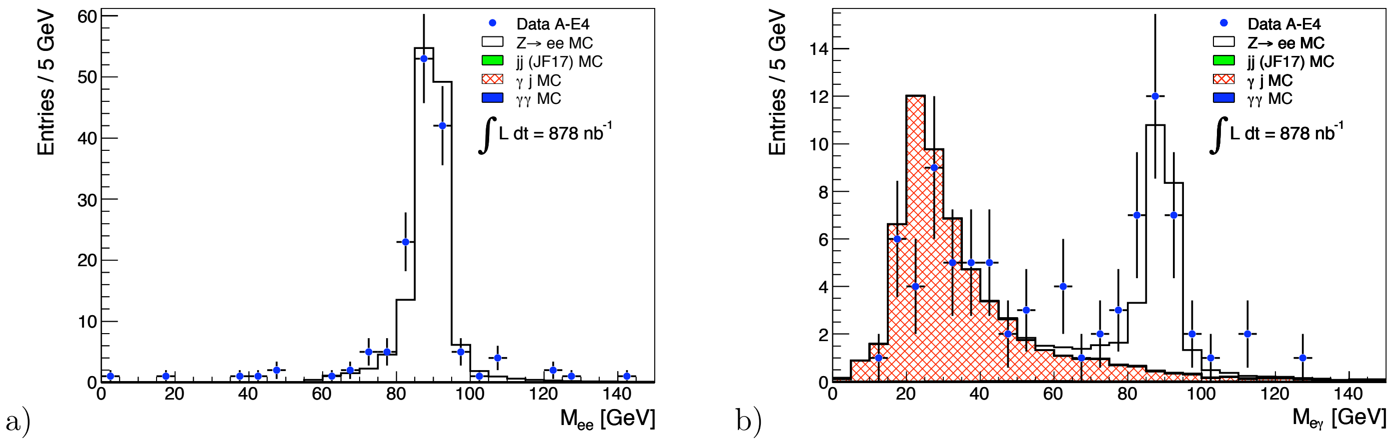

Figure A.15. Invariant mass plots for the ee (a) and eγ (b) final states, shown using MC and 880 nb^{-1} collision data. The entire mass range is shown. In the mass range used in the electron-photon fake rate calculation, 66-116 GeV, 38 $e\gamma$ and 156 ee pairs are found. The background estimate from MC, 5 events, is taken to yield 33 $e\gamma$ signal pairs in the mass range used. This is the number used in the calculation of ρ.

the reconstructed $e\gamma$ events.

Using the measurement of ρ on data, the values $L = 880\ nb^{-1} \pm_{syst} 11\%$, the number of observed photon candidates $N_\gamma = 56974$ (as from the sum of entries in 2nd column of Table A.8, for $E_T > 20$ GeV) and $\sigma_{e_{EW}} = (3.6 \pm 0.3) \times 10^3\ pb$, the impurity contribution from electrons from EW decays is estimated to be $(0.5 \pm 0.1)\%$.

The E_T dependence of the contributions is shown in Table A.8, based on the value of $\frac{d\sigma_{EW}}{dp_T}$, which has been extrapolated using the JF17 sample in the same manner as for σ_{EW}. (see Figure A.18). The fake rate ρ as a function of E_T is taken from the $L = 880\ nb^{-1} \pm_{syst} 11\%$ collision data set, and is shown in Figure A.16. The available statistics is not enough to evaluate the electron impurity in each (η, E_T) bin. However, an idea of the trend versus η can be obtained from Table A.9, where the impurity is evaluated in the four η regions, integrated in E_T in the range $20 \div 100$ GeV.

E_T interval [GeV]	N_γ	ρ_{Data}	from EW particles $(d\sigma_e/dE_T)$ $\times(\Delta E_T)$ [nb]	$I(\%)$
15÷20	83463	|	|	|
20÷25	29051	$.351 \pm_{st} .1 \pm_{sy} .05$	$.691 \pm .09$	0.7 ± 0.3
25÷30	12547	$.105 \pm_{st} .05 \pm_{sy} .01$	$.561 \pm .08$	0.4 ± 0.2
30÷35	6259	$.100 \pm_{st} .05 \pm_{sy} .01$	$.594 \pm .08$	0.8 ± 0.4
35÷40	3457	$.055 \pm_{st} .03 \pm_{sy} .007$	$.756 \pm .09$	1.1 ± 0.6
40÷50	3181	$.113 \pm_{st} .03 \pm_{sy} .01$	$.788 \pm .09$	2.5 ± 0.8
50÷60	1280	$.163 \pm_{st} .08 \pm_{sy} .02$	$.140 \pm .04$	1.6 ± 0.9
60÷100	1199	$.046 \pm_{st} .05 \pm_{sy} .006$	$.076 \pm .03$	0.3 ± 0.3

Table A.8. Evaluation of the impurity due to electrons from decays of EW particles (columns 4–5) , for each E_T interval. Here N_γ is the number of photon candidates passing tight and isolation cuts, $d\sigma_e/dE_T$ the differential cross-section in the E_T bin of width ΔE_T (statistical error shown), and I the impurity, or electron fraction in the photon sample, as calculated in each E_T bin.

A.4.1. Characteristics of fake γ, 880 nb^{-1}

Important characteristics of the photon fakes from electrons are given in Table A.10 and Figure A.19.

Using the $Z \to ee$ MC sample and examining photons in the $e\gamma$ mass within the range 66 GeV< $M_{e\gamma}$ <116 GeV, 62% of the fake photons matching to true electrons pass the isolation cut when reconstructed and 12% fail. The isolation distribution of the photon in the $e\gamma$ mass is given in Figure A.21.

η interval	N_γ	ρ_{Data}	from EW particles	
			$(d\sigma_e/d\eta)$ $\times(\Delta E_T)$ [nb]	$I(\%)$
0.00÷0.60	15147	$.059 \pm_{st} .02 \pm_{sy} .008$	$1.231 \pm .13$	$.4 \pm .2$
0.60÷1.37	20304	$.058 \pm_{st} .02 \pm_{sy} .008$	$1.220 \pm .13$	$.3 \pm .1$
1.52÷1.81	8931	$.097 \pm_{st} .05 \pm_{sy} .01$	$.464 \pm .07$	$.4 \pm .2$
1.81÷2.37	12592	$.051 \pm_{st} .03 \pm_{sy} .007$	$.713 \pm .09$	$.3 \pm .2$

Table A.9. Evaluation of the impurity due to electrons from decays of EW particles (columns 4–5), for each η interval. Here N_γ is the number of photon candidates with $E_T > 20$ GeV, passing tight and isolation cuts, $d\sigma_e/d\eta$ the differential cross-section in the η bin of width $\Delta\eta$ (statistical error shown), and I the impurity, or electron fraction in the photon sample, as calculated in each η bin.

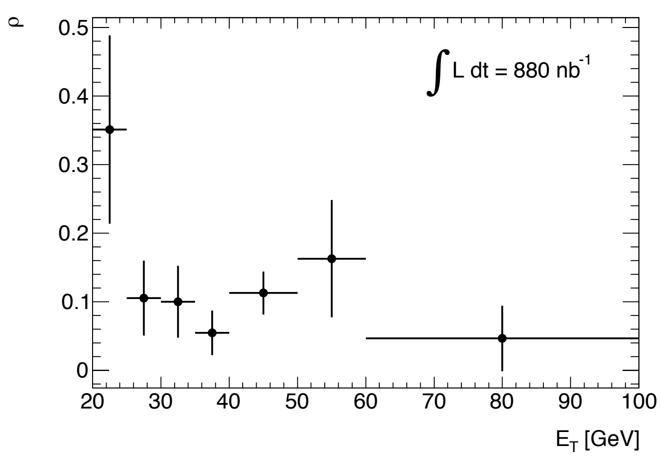

Figure A.16. Electron-photon misidentification rate, ρ, as measured on $L = 880\ nb^{-1} \pm_{syst} 11\%$. The measurement is shown in bins of E_T.

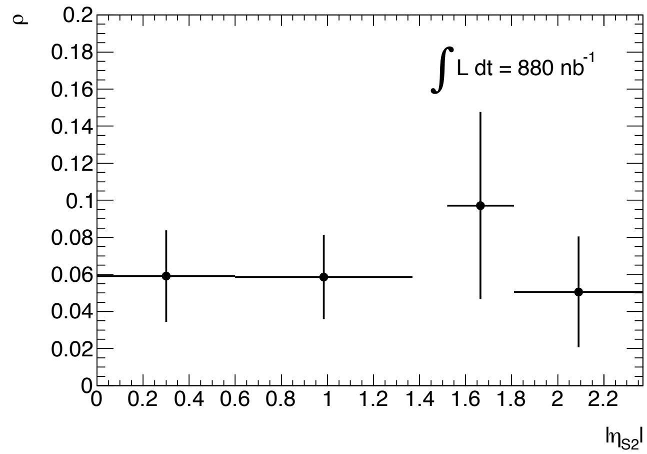

Figure A.17. Electron-photon misidentification rate, ρ, as measured on $L = 880\ nb^{-1} \pm_{syst} 11\%$. The measurement is shown in bins of η.

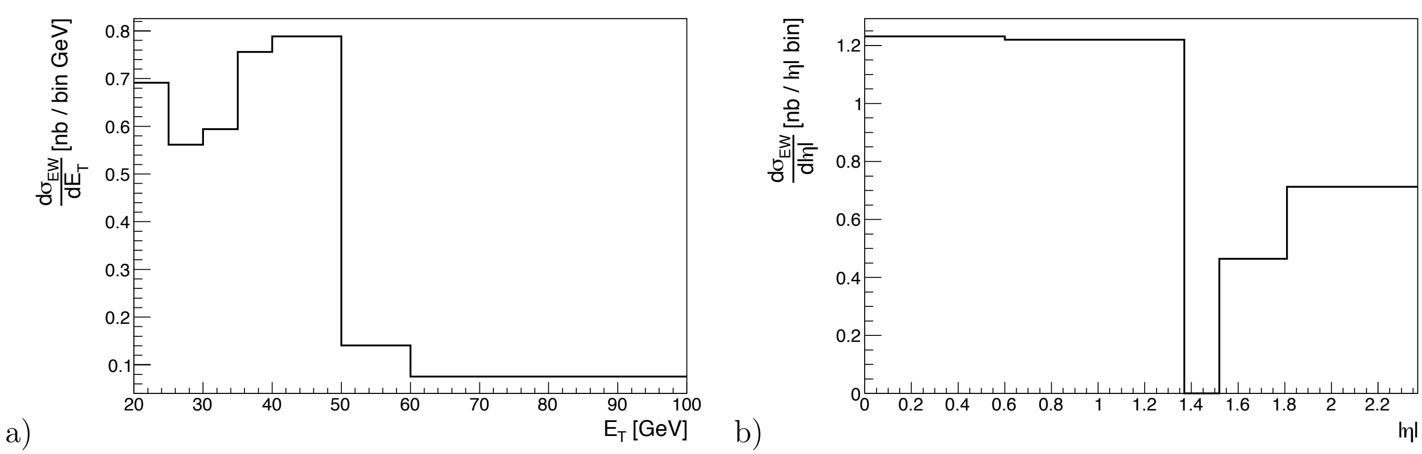

Figure A.18. For electrons from EW sources, differential cross section $(\frac{d\sigma_e}{dE_T})$and (b) $(\frac{d\sigma_e}{d\eta})$. The JF17 sample is used.

Table A.10. Characteristics of fake photons from electrons. Comparison is made to results from the unfiltered Z→ee Monte Carlo sample.

880 nb^{-1} data		
% recovered	$(66 \pm 20)\%$	
% converted	$(68 \pm 20)\%$	
	% single track:	% double track:
	$(38 \pm 10)\%$	$(62 \pm 20)\%$

MC Z→ee		
% recovered	$(85.1 \pm 0.3)\%$	
% converted	$(79.8 \pm 0.3)\%$	
	% single track:	% double track:
	$(60.9 \pm 0.3)\%$	$(39.1 \pm 0.2)\%$

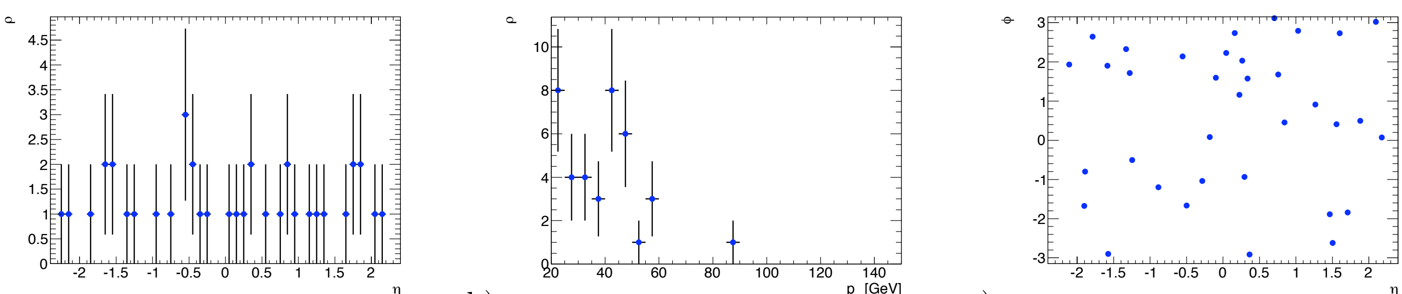

a) b) c)

Figure A.19. η (a), p_T (b) and η, ϕ (c) distributions using 880 nb^{-1} collision data, for photons in the eγ invariant mass depicted in Figure A.15

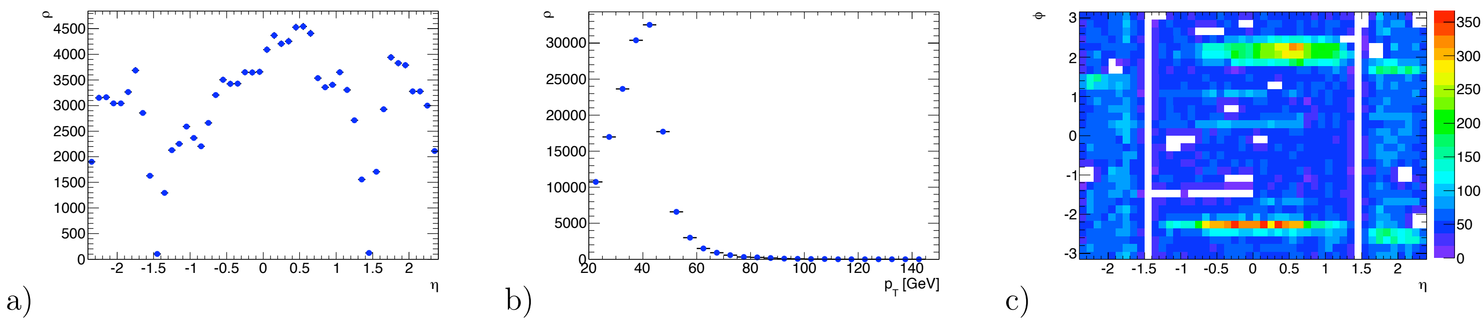

Figure A.20. η (a), p_T (b) and η,ϕ (c) distributions using Z→ee MC (5.2 fb^{-1}) normalized to 880 nb^{-1} for photons in the eγ invariant mass depicted in Figure A.15 (b).

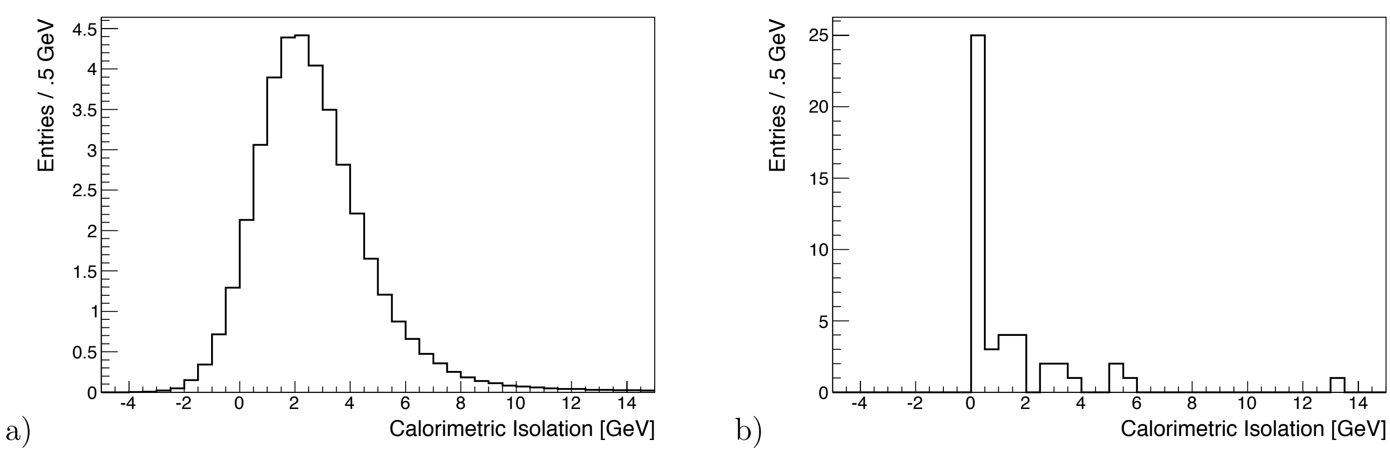

Figure A.21. Calorimetric isolation for the photon in the $e\gamma$ mass within the range 66 GeV< $M_{e\gamma}$ <116 GeV, for (a) Z→ee MC and (b) data. The reconstructed photons are required to pass all analysis cuts with the exception of isolation.

Appendix B

Relationship between A_{FB}, and m_H, the Higgs mass

Physics isn't a religion. If it were, we'd have a much easier time raising money.
On the difficulty of acquiring funds for pure science

Leon Lederman (1922-present)
American physicist, Nobel laureate

Due to the presence of both charged and neutral currents, there are two coupling constants for the weak interactions, g' and g. These coupling constants are related by the weak (sometimes referred to as electroweak, or Weinberg) mixing angle:

$$tan\theta_W = \frac{g'}{g}. \tag{B.1}$$

The value of θ_W is related to the forward-backward asymmetry, A_{FB}, measured near the Z pole by:

$$A_{FB} = b\left(a - sin^2\theta_W\left(M_Z\right)\right), \tag{B.2}$$

where a and b are factors from the specific parton density functions (PDFs) used; the PDFs describe the quark content of protons.

In the minimal Standard Model, which refers to the choice of Higgs field with the lowest number of free parameters, the weak angle also relates the masses of the W and Z bosons:

$$\frac{M_W}{M_Z} = cos\theta_W. \tag{B.3}$$

This can be rewritten as

$$\rho_0 \equiv \left(\frac{M_W}{M_Z}\right)^2 \frac{1}{cos^2\theta_W} = 1, \tag{B.4}$$

which is frequently used as an experimental test of the minimal Standard Model.

If first order radiative corrections to the minimal Standard Model–meaning the Standard Model where a single doublet of scalar fields is chosen for the Higgs field–are considered, the mass of the top quark, M_t, and the mass of the Higgs boson, M_H, are correlated with the electroweak parameters θ_W and M_Z:

$$\frac{G}{\sqrt{2}} = \frac{e^2}{8sin\theta_W^2 cos^2\theta_W M_Z^2}\left(1 + 1.064\alpha - \frac{cos^2\theta_W}{sin^2\theta_W}\Delta\rho + \Delta r\right), \tag{B.5}$$

where G is measured from the muon lifetime, α is the fine structure constant, e is the electron charge, and $\Delta\rho$ and Δr are given by (B.6) and (B.7).

$$\Delta\rho \approx \frac{3e^2}{64\pi^2 sin^2\theta_W cos^2\theta_W M_Z^2} M_t^2 \tag{B.6}$$

$$\begin{aligned} \Delta r_{Higgs} &= \frac{e^2}{64\pi^2 sin^2\theta_W}\frac{11}{3}\left[ln\left(\frac{M_H^2}{cos^2\theta_W M_Z^2}\right) - \frac{5}{6}\right], \\ \Delta r_{top} &= \frac{e^2}{64\pi^2 sin^2\theta_W} 2\left(\frac{cos^2\theta_W}{sin^2\theta_W} - \frac{1}{3}\right) ln\left(\frac{M_t^2}{cos^2\theta_W M_Z^2}\right) \end{aligned} \tag{B.7}$$

A precision measurement of θ_W can be obtained via measurement of M_Z and measurement of A_{FB} near the Z pole (as described by (B.2)). Such a measurement of θ_W can provide a constraint on M_H, in addition to those imposed by direct searches.

REFERENCES

[1] A. Bingul. ATLAS TRT and its performance at the LHC. *ATL-COM-PHYS-2011-662* (2011), 31.

[2] A. Caldwell and D. Kollar and K. Kroninger. BAT - The Bayesian Analysis Toolkit. *Computer Physics Communications 180* (2009), 2197–2209.

[3] A. Martin, W. Stirling, R. Thorne and G. Watt. Parton Distributions for the LHC. *European Journal of Physics C 63* (2009), 189.

[4] A. Sherstnev and R. S. Thorne. Parton Distributions for LO Generators. *European Journal of Physics C55* (2008), 553.

[5] AMI Production database. https://ami.in2p3.fr/.

[6] ATLAS collaboration. Forward electron reconstruction and identification inputs, egammaForwardGetter.py. Internal documentation available to ATLAS users on svn: https://svnweb.cern.ch/trac/atlasoff.

[7] ATLAS collaboration. Forward electron reconstruction and identification tool, egammaForwardBuilder.cxx. Internal documentation available to ATLAS users on svn: https://svnweb.cern.ch/trac/atlasoff.

[8] ATLAS collaboration. Standard electron cut tool, egammaElectron-CutIDTool.cxx. Internal documentation available to ATLAS users on svn: https://svnweb.cern.ch/trac/atlasoff.

[9] ATLAS collaboration. Standard electron cut tool inputs, egammaElectron-CutIDToolBase.py. Internal documentation available to ATLAS users on svn: https://svnweb.cern.ch/trac/atlasoff.

[10] ATLAS collaboration. ATLAS detector and physics performance: technical design report. *CERN/LHCC 99-14* (1999), 13.

[11] ATLAS collaboration. Calibration and Performance of the Electromagnetic Calorimeter. *CERN-OPEN-2008-020* (2008), 44–71.

[12] ATLAS COLLABORATION. Reconstruction and Identification of Electrons. *CERN-OPEN-2008-020* (2008), 88–90.

[13] ATLAS COLLABORATION. The expected performance of the Inner Detector. *CERN-OPEN-2008-020* (2008), 16–41.

[14] ATLAS COLLABORATION. The Trigger for Early Running. *CERN-OPEN-2008-020* (2008), 550–564.

[15] ATLAS COLLABORATION. Supporting note for the measurement of the production cross-section of Wenu and Zee at sqrt(s) = 7 TeV with the ATLAS detector. *ATL-COM-PHYS-2010-539* (2010), 31.

[16] ATLAS COLLABORATION. The ATLAS Simulation Infrastructure. *European Journal of Physics C70* (2010), 823–874.

[17] ATLAS COLLABORATION. W→enu and Z→ee cross-section measurments in proton-proton collisions at sqrt(s) = 7 TeV with the ATLAS detector. *ATL-PHYS-INT-2010-125* (2010), 55.

[18] ATLAS COLLABORATION. Efficiencies of electron/photon triggers using early 2011 data: Approval for PLHC2011. *ATL-COM-DAQ-2011-032* (2011), 3.

[19] ATLAS COLLABORATION. Electron performance measurements with the ATLAS detector using the 2010 LHC proton-proton collision data. *ATL-COM-PHYS-2011-546, submitted to European Journal of Physics C* (2011), 45.

[20] ATLAS COLLABORATION. Measurement of the inclusive isolated prompt photon cross section in pp collisions at $\sqrt{s}$ =7 TeV with the ATLAS detector. *Phys. Rev. D83* (2011), 052005.

[21] ATLAS COLLABORATION. Search for dilepton resonances in pp collisions at $\sqrt{s}$ = 7 TeV with the ATLAS detector. arXiv:1108.1582 (submitted to PRL), 2011.

[22] ATLAS COLLABORATION. Search for high-mass dilepton resonances in pp collisions at $\sqrt{s}$ = 7 TeV (2011 update for the EPS conference). *ATL-COM-PHYS-2011-770* (2011).

[23] ATLAS COLLABORATION. Search for high mass dilepton resonances in pp collisions at $\sqrt{s}$ =7 TeV with the ATLAS experiment. *ATLAS-COM-CONF-2011-098* (2011), 20.

[24] ATLAS COLLABORATION. Search for high mass dilepton resonances in pp collisions at $\sqrt{s}$ = 7 TeV with the ATLAS experiment. *Phys.Lett. B700* (2011), 163–180.

[25] ATLAS electron-photon combined performance group. Electron Identification. ATLAS internal documentation, availble to ATLAS users on twiki: https://twiki.cern.ch/twiki/bin/view/AtlasProtected/ElectronIdentification.

[26] ATLAS electron-photon combined performance group. Electron Reconstruction. ATLAS internal documentation, availble to ATLAS users on twiki: https://twiki.cern.ch/twiki/bin/view/AtlasProtected/ElectronReconstruction.

[27] ATLAS electron-photon combined performance group. Event display photon / pi0. Publicly available plots: https://atlas.web.cern.ch/Atlas/GROUPS/PHYSICS/EGAMMA/PublicPlots.

[28] ATLAS electron-photon combined performance group. LAr cleaning and Object Quality. Internal documentation available to ATLAS users on twiki: https://twiki.cern.ch/twiki/bin/view/AtlasProtected/LArCleaningAndObjectQuality.

[29] ATLAS electron-photon combined performance group. Photon Reconstruction. Available to ATLAS users on twiki: https://twiki.cern.ch/twiki/bin/view/AtlasProtected/PhotonReconstruction.

[30] ATLAS LAr collaboration. Description of different sources of noise in LAr. Internal documentation available to ATLAS users on twiki: https://twiki.cern.ch/twiki/bin/viewauth/Atlas/LArNoiseSummary.

[31] C. M. Carloni Calame, G. Montagna, O. Nicrosini and A. Vicini. Precision electroweak calculation of the charged current Drell-Yan process. *JHEP 0612* (2006), 016.

[32] C. M. Carloni Calame, G. Montagna, O. Nicrosini and A. Vicini. Precision electroweak calculation of the production of a high transverse-momentum lepton pair at hadron colliders. *JHEP 0710* (2007), 109.

[33] CEA Saclay Institute. Superconducting quadrupole magnets for the LHC. Source used for image only, available at http://irfu.cea.fr/en/Phocea/Vie_des_labos/Ast/ast_visu.php?id_ast=2411.

[34] CERN: European Organization for Nuclear Research. The coupling constants and unification of forces. Particle Physics Education CD-ROM (image source only), 1999.

[35] CERN publications. LHC: collisions on course for 2007. Source used for image only.

[36] CMS collaboration. Search for Resonances in the Dilepton Mass Distribution in pp Collisions at $\sqrt{s} = 7$ TeV. CMS public note, 2011.

[37] D. Damiani, J. Mitrevski. Phi asymmetry in fake single-track photon conversions, 2010. Available to ATLAS users on indico: http://indico.cern.ch.

[38] D. London and J.L. Rosner. Extra Gauge Bosons in E(6). *Phys. Rev. D34* (1986), 1530.

[39] D0 collaboration. Measurement of $\sin^2\theta^l_{eff}$ and Z-light quark couplings using the forward-backward charge asymmetry in $p\overline{p} \rightarrow Z/\gamma^* \rightarrow e^+e^-$ events with L = 5.0 fb^{-1} at $\sqrt{s}$=1.96 TeV. *Phys.Rev. D84* (2011), 012007.

[40] E. Berglund. Tag and Probe using Z→ee analysis on D3PDs, 2010. Available to ATLAS users on indico: http://indico.cern.ch.

[41] F. Dudziak. Electron reconstruction and identification in ATLAS. Implication for the Higgs into four electron final state. *ATL-PHYS-PROC-2010-039* (2010), 5. This is a H→4lepton note, but the efficiencies documented within are official eγ efficiencies for any electrons with p_T >20 GeV.

[42] F. James and M. Roos. MINUIT-Function minimisation and error analysis, 1988.

[43] G. Aad et al. The ATLAS Experiment at the CERN Large Hadron Collider. *JINST 3* (2008), S08003.

[44] G. Corcella *et al*. HERWIG 6.5 release note. *arXiv:hep-ph/0210213*.

[45] G. Corcella *et al*. HERWIG 6: an event generator for hadron emission reactions with interfacing gluons (including supersymmetric processes). *JHEP 01* (2001), 010.

[46] G. W. Anderson. Tools for E_6 model building. In proceedings from "Third Latin American Symposium on High Energy Physics".

[47] GEANT4 Collaboration, S. Agostinelli *et al*. Geant4: a simulation toolkit. *Nucl. Instrum. Meth. A506* (2003), 250.

[48] Gillies, J. and Jacobsson and R., Lenz, O. Particle Physics Educational CD-ROM, 2001. Available at http://keyhole.web.cern.ch/keyhole//projects/number_of_families.html (source used only for image).

[49] J. Leveque and B. Trocme. LAr data quality: What CP groups need to know about the data. Available to ATLAS users on indico: http:://indico.cern.ch.

[50] J. M. Butterworth, J. R. Forshaw and M. H. Seymour. Multiparton interactions in photoproduction at HERA. *Z. Phys. C72* (1996), 637–646.

[51] J. Pumplin *et al*. New generation of parton distributions with uncertainties from global QCD analysis. *JHEP 07* (2002), 012.

[52] J.C. Collins and D. E. Soper. Angular distribution of dileptons in high energy hadron collisions. *Physical Review D 16* (1977), 2219.

[53] J.L. Hewett and T. G. Rizzo. Low-energy phenomenology of superstring-inspired E_6 models. *Phys. Rept. 183* (1989), 193.

[54] M. Aharrouche *et al*. Electron performance in the ATLAS experiment. *ATL-COM-PHYS-2010-208* (2010), 44.

[55] M. Aharrouche *et al*. Total and differential W→lν and Z→ll cross-sections measurements in proton-proton collisions at $\sqrt{s}$ =7 TeV with the ATLAS detector. *ATL-COM-PHYS-2011-751* (2011), 230.

[56] M. Aliev *et al*. HATHOR-HAdronic Top and Heavy quarks crOss section calculatoR. *Comput. PHys. Commun. 182* (2011), 1034–1046.

[57] M. L. Mangano, M. Moretti, F. Piccinini, R. Pittau and A. D. Polosa. ALPGEN, a generator for hard multiparton processes in hadronic collisions. *JHEP 07* (2003), 001.

[58] N. Fatemi-Ghomi. Measurement of the Double Beta Decay Half-life of ^{150}Nd and Search for Neutrinoless Decay Modes with the NEMO-3 Detector. Thesis submitted in fulfillment of requirements for doctoral degree, 2009.

[59] N. Kerschen. Electron Reconstruction and Identification with the ATLAS Detector. *ATL-PHYS-PROC-2009-111* (2009), 2009 Europhysics Conference on High Energy Physics, Krakow, Poland, 16 Jul – 22 Jul 2009.

[60] O. Klein. Quantum Theory and Five-Dimensional Theory of Relativity. (In German and English). *Z.Phys 37* (1926), 895–906.

[61] P. Golonka and Z. Was. PHOTOS Monte Carlo: a precision tool for QED corrections in Z and W decays. *European Journal of Physics C 45* (2006), 97–107.

[62] P. Langacker. The Physics of Heavy Z' Gauge Bosons. *Rev. Mod. Phys 81* (2009), 1199.

[63] P. Renton. Has the Higgs boson been discovered? *Nature 428* (2011), 141–144. Source used for image only.

[64] P.T. Hurst. A measurement of $\sin^2\theta(W)$ from the forward-backward asymmetry in p anti-p $\rightarrow Z0 \rightarrow e + e-$ interactions at $\sqrt{s} = 1.8$ TeV. Ph.D. Thesis (Advisor: L. E. Holloway), 1990.

[65] R. Adolphi et al. The CMS experiment at the CERN LHC. *JINST 3* (2008), S08004.

[66] R. Barlow and C. Beeston. Fitting using finite Monte Carlo samples. *Comp. Phys. Comm. 77* (1993), 219–228.

[67] R. Brun and F. Rademakers. ROOT–An Object Oriented Data Analysis Framework. *Nucl. Inst. and Meth. in Phys. Rev. A 389* (1997), 81–86. Proceedings of AIHENP'96 Workshop, Lausanne, Sep 1996.

[68] R. Daya *et al.* Exclusion Prospects for the Standard Model Higgs Boson Decaying into Two Photons. *ATL-PHYS-INT-2010-061* (2010), 63.

[69] R. Daya *et al.* Limit setting and signal extraction procedures in the search for narrow resonances decaying into leptons at ATLAS. *ATL-COM-PHYS-2011-085* (2011), 15.

[70] R. Daya *et al.* Purity Estimates for the Inclusive Isolated Photons. *ATL-PHYS-INT-2011-015* (2011), 38–43.

[71] R. Daya *et al.* Search for high-mass dilepton resonances in 2011 data with $\sqrt{s} =$ 7 TeV. *ATL-COM-PHYS-2011-465* (2011).

[72] R. Hamberg, W. L. van Neerven, and T. Matsuura. A Complete calculation of the order α_s^2 correction to the Drell-Yan K factor. *Nucl. Phys. B359* (1991), 343–405.

[73] R. Ishmukhametov, D. Joffe, R. Daya, R. Stroynowski. Estimated systematic uncertainty due to detector non-uniformity and its implications for the exclusion limit calculation in H channel using simulated data at 10 TeV. *ATL-PHYS-INT-2010-055* (2010), 11.

[74] R. Ishmukhametov, F. Polci, Q. Buat, L. Serin. Personal correspondance with ATLAS object quality experts. At 2010 ATLAS eγ workshop".

[75] ROOT analysis framework,. TFractionFitter. http://root.cern.ch/root/html/TFractionFitter.html.

[76] Rosner, J. Forward-backward asymmetries in hadronically produced lepton pairs. *Physical Review D 54*, 1 (1996), 1078–1082.

[77] S. A. Thomas, F. B. Abdalla, and O. Lahav. Upper Bound of 0.28eV on the Neutrino Masses from the Largest Photometric Redshift Survey. *Phys.Rev.Lett. 105* (2010), 031301.

[78] S. Cheuklaev. Report from Run Coordinators. Presentation shown at LAr Weekly meeting May 2, 2011.

[79] S. Frixione and B. Webber. Matching NLO QCD computations and parton shower simulations. *JHEP 0206* (2002), 029.

[80] S. Hassani, C. Petridou, D. Illiadis, K. Bachas. The Tag and Probe method with $J/\psi \rightarrow \mu^+\mu^-$ and $\Upsilon \rightarrow \mu^+\mu^-$ candidates in ATLAS. *ATL-PHYS-INT-2010-050* (2010), 20.

[81] S. Menke. Status of local hadron calibration. Presentation shown at ATLAS Week, December 2, 2008, Jet E_T session.

[82] S. Moch and P. Uwer. Theoretical status and prospects for top-quark pair production at hadron colliders. *Physical Review D 78* (2008), 034003.

[83] S.D. Drell, T.M. Yan. Massive Lepton Pair Production in Hadron-Hadron Collisions at High-Energies. *Phys.Rev.Lett. 25* (1970), 316–320.

[84] T. Sjostrand, S. Mrenna and P.Z. Skands. PYTHIA 6.4 Physics and Manual. *JHEP 05* (2006), 026.

[85] T. Yamamura, J. Tanaka, S. Asai. 7 TeV sample checks. available to ATLAS users on indico: http://indico.cern.ch.

[86] Tankersley, Jr., R. and Orvis, K. Modeling the Geography of Migratory Pathways and Stopover Habitats for Neotropical Migratory Birds. *Ecology and Society 7*, 1 (2003), 7.

[87] Th. Kaluza. On the Problem of Unity in Physics. *Sitzungsber.Preuss.Akad.Wiss.Berlin (Math.Phys.) 1921* (1921), 966–972.

[88] The European Organization for Nuclear Research (CERN). The accelerator complex, 2008. Public information about CERN and the LHC system, available at http://public.web.cern.ch/public/en/research/AccelComplex-en.html.

[89] Trottier-McDonald, M. and O'Neil, D. C. Identifying hadronic tau decays using calorimeter topological clusters at ATLAS. *ATL-PHYS-INT-2011-034* (2011), 36.

[90] U. Baur, O. Brein, W. Hollik, C. Schappacher and D. Wackeroth. Electroweak Radiative Corrections to Neutral-Current Drell-Yan Processes at Hadron Colliders. *Phys.Rev. D65* (2002), 033007.

[91] U. Langenfeld, S. Moch and P. Uwer. New results for $t\bar{t}$ production at hadron colliders. *arXiv:0907.2527 [hep-ph]*.

[92] V. Rubin, W.K. Ford, Jr. Rotation of the Andromeda Nebula from a Spectroscopic Survey of Emission Regions. *Astrophysical Journal 159* (1970), 379.

[93] V.D. Barger, W. Keung and E. Ma. Sequential W and Z bosons. *Phys.Lett. B94* (1980), 377.

[94] W. Lampl *et al*. Calorimeter Clustering Algorithms: Description and Performance. *ATL-LARG-PUB-2008-002* (2008), 18.

[95] Wikipedia. Various articles. Available at http://en.wikipedia.org/ (Source used only for image).